NASS
NAN YANG ACADEMY OF SCIENCES

Earth and Planetary Science

Volume 1 · Issue 1 · April 2022 ISSN 2810-9732(Online)

Editor-in-Chief

Ziyuan Ouyang
Chinese Academy of Sciences, China

Editorial Board Members

Venkata Ravibabu Mandla, India

Biswajit Nath, Bangladesh

Mukaila Abdullahi, Nigeria

Sathish Sathasivam, India

Vinod Kumar, India

Weibiao Xie, China

Armel Ekoa, Cameroon

Waseem H Naseeri, Pakistan

Pandurang Prakash Choudhari, India

Pemmani VS Raju, India

Adem Akpınar, Turkey

Volume 1 Issue 1 • April 2022 ISSN 2810-9732 (Online)

Earth and Planetary Science

Editor-in-Chief

Ziyuan Ouyang

NASS
NAN YANG ACADEMY OF SCIENCES

NASS
NAN YANG ACADEMY OF SCIENCES

Volume 1 | Issue 1 | April 2022 | Page1-49
Earth and Planetary Science

Contents

Research Articles

1 **Integrated Geophysical and Geospatial Approaches for Delineating Groundwater Potential Zones in Karachi, Pakistan**
Muhammad Jahangir Khan Syeda Rida Fatima Bokhari Umair Bin Nisar Farhad Ali

35 **Assessment of Pollution and Identification of Sources of Heavy Metals, and Radionuclides Contamination in Sand along the Southern Part of the Cameroonian Coast (South-West, Africa)**
Francis Temgo Sopie Victorine Ambassa Bela Armel Zacharie Ekoa Bessa Archange Duviol Tsanga Patrice Roland Liyouck Théophile Njanko Gabriel Ngueutchoua

Review Article

22 **Contribution to the Paleontology, Stratigraphy and Paleogeography of Ninety-seven Southern Tethyan Agglutinated Foraminiferal Species**
Haidar Salim Anan

Case Report

10 **Evaluation of Wellbore Stability by Analytical and Numerical Methods: A Case Study in a Carbonate Oil Field**
Faramarz Abazari Hossein Jalilifar Mohammad Ali Riahi

Earth and Planetary Science
https://ojs.nassg.org/index.php/eps/index

RESEARCH ARTICLE

Integrated Geophysical and Geospatial Approaches for Delineating Groundwater Potential Zones in Karachi, Pakistan

Muhammad Jahangir Khan[1*] Syeda Rida Fatima Bokhari[2] Umair Bin Nisar[3] Farhad Ali[1]

1. Department of Earth & Environmental Sciences, Bahria University Karachi Campus, Pakistan
2. The State Key Laboratory of Information Engineering in Surveying, Wuhan University, China
3. Centre for Climate Research and Development, COMSATS University, Islamabad Campus, Islamabad, Pakistan

ARTICLE INFO

Article history
Received: 22 April 2022
Revised: 17 May 2022
Accepted: 23 May 2022
Published Online: 2 June 2022

Keywords:
Aquifer
Vertical electrical sounding
Weighted overlay analysis
GIS

ABSTRACT

Availability of subsurface fresh water in coastal cities of the world is a growing problem due to sea level intrusion and less seepage. The authors have utilized an integrated data dataset in which conventional geophysical methods were used to collect primary data for the groundwater resources in Karachi and geospatial approaches were used to generate the hydrogeological model. It aimed to investigate geological/hydrogeological conditions of any aquifer system in the study area. The geophysical survey was planned to acquire electrical resistivity data in the outskirts of Karachi. The geophysical survey was carried out at twenty-one stations by adopting vertical electrical sounding technique with schlumberger configuration. The field data were processed in an iterative process to improve the signal to noise ratio and obtain smooth field data curves for delineation of the aquifer. The authors have interpreted field data to model the geological information and determine the hydrogeophysical parameters of respective layers. These parameters including the number of layers, aquifer resistivity, aquifer lithology, aquifer thickness and depth to the aquifer, are determined at each field station. The acquired dataset of hydrogeophysical parameters was used to build a geospatial database. The multi-criteria analysis and decision-making process were utilized in GIS-based program to model spatial distribution of these parameters. The results identified an aquifer system in the depth ranging from 53.3 meters to 143.9 meters. The aquifer in the area is mostly sandstone having sufficient thickness which varies from northeast to south and southwest due to undulating topography of the area. The maximum potential of the groundwater is identified in the south which is suitable for water exploration because of low resistivity zone, high aquifer thickness, and flow of drainage network.

*Corresponding Author:
Muhammad Jahangir Khan,
Department of Earth & Environmental Sciences, Bahria University Karachi Campus, Pakistan;
Email: mjahangir.bukc@bahria.edu.pk

DOI: http://dx.doi.org/10.36956/eps.v1i1.520

Copyright © 2022 by the author(s). Published by Nan Yang Academy of Sciences Pte. Ltd. This is an open access article under the Creative Commons Attribution-NonCommercial 4.0 International (CC BY-NC 4.0) License. (https://creativecommons.org/licenses/by-nc/4.0/).

1. Introduction

The massive body of sea is at door-step of the coastal towns around the globe. Therefore, the groundwater resources are under threat of advancing saltwater intrusion. Where to drill a borehole for pumping groundwater in a coastal city? It is a challenging and complicated question for town developers, planners, and common public living in coastal regions around the world [1,2]. Centuries ago, people used "dowsing method" [3]. Geophysical and geospatial studies attempt to help in demarcation of the groundwater potential zones to fulfill growing needs of water supply. The geophysical techniques such as electrical resistivity, induced polarization, and electromagnetic induction methods are employed for shallow geological mapping and hydrogeological studies around the globe. These shallow geophysical methods are found helpful within anisotropic medium and to solve water related problems such as exploration for promising aquifer, water pollution monitoring, water management and environmental preservation [4-6]. Hydrogeophysical delineations facilitate obtaining information about aquifer, although sometimes uncertainty in interpretation precludes the recommendation for drilling [7]. The primary difficulties in groundwater modelling can be abridged by interpretation and careful inversion techniques applied to process the resistivity datasets [8,9]. The development of digital data modeling and computer solutions has improved the reliability of geophysical data interpretation [10,11]. Literature review suggests that ground resistivity is a function of various factors which are lithology type of geological layer, mineralogical content and fluid saturation, depth to the geological layer, porosity, and permeability of clastic rocks [12]. The geological environment and recharge potential in an area also affect the resistivity values therefore time series/seasonal analysis of aquifer potential could help to improve the hydrogeological investigations.

Geographical information system (GIS) facilitates in mapping and modelling of spatial databases. For example, the hydrogeophysical database consists of parameters obtained from the geophysical data interpretation [13-15]. GIS-based mapping techniques are effectively used for spatial analysis and decision making. Review of the studies [12,16] suggests that the scope of groundwater studies is broadened by undertaking spatial modelling techniques. GIS-based suitability model for well-location can be created by considering multiple data variables such as layer thickness, depth to aquifer, and ground resistivity of aquifer [17-20].

The coastal cities of Pakistan including Karachi, Thatta, Ormara, Pasni, Gwadar, and other small towns are facing a serious problem in searching of groundwater aquifers. Geoscientists are making their efforts to explore and protect groundwater resources in coastal towns [21-23]. Karachi is one of the largest cities of Pakistan which is further expending in northeastern outskirts. The fast-growing urbanization projects demand mapping of sweet-water aquifers in and around Karachi. Seasonal rainfall is the main source of groundwater recharge in Karachi and its immediate surroundings. Overall, arid climate in the region prevails which limit the recharge potential and channel flow down the streams to southwest. It is speculated that the precipitation rate in Karachi has decreased from 200 mm/yr to 20 mm/yr, majorly causing shifting of monsoon seasonal trends of rain fall system in Karachi region [24,25]. Thereby imbalance between the pumping rate and recharging rate of aquifers imposes adverse impact on quality of groundwater [11]. The present study is designed to investigate hydro-geological conditions of aquifers in hilly outskirts of Karachi city. The objectives are to find the hydrogeological conditions of the subsurface and possible aquifer systems using electrical resistivity method and to classify the region based on spatial analysis of the aquifer and to demarcate the best potential zone to get optimum groundwater.

There are several under-developed towns in northeastern edge of Karachi city. Understudy area is located inside DHA City Karachi (DCK) which is under-development town located to the northeast of Karachi along the motorway section of M-9 (Figure 1a). Khadeji anticline exposed clastic rocks composed of sandstone, shale and limestone in the study area. Hydrological model indicates that the DCK is located in the upper Malir basin, therein two small ephemeral streams known as Abdar and Sukkun and two larger intermittent streams known as Khadeji and Mol are located to the south and north of DCK respectively. These streams drain in Malir river which eventually leads to drain in the Arabian sea (Figure 1b).

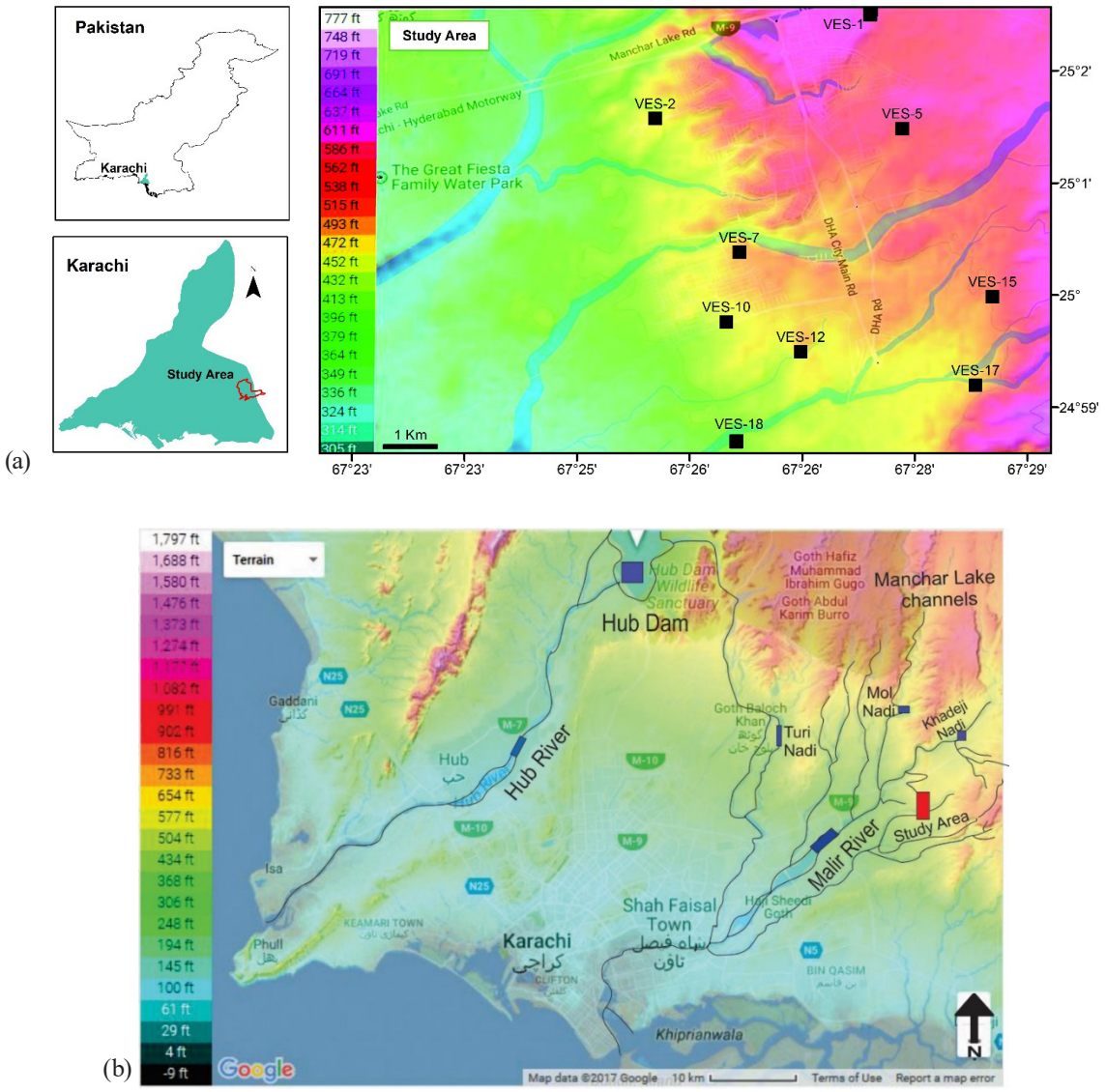

Figure 1. (a). Location of study area and locations of VES points. (b). Hydrological and topographic features in outskirts of Karachi.

2. Data and Methodology

This study is based on acquisition of geophysical dataset using electrical resistivity method, interpretation of field datasets to obtain the hydrogeophysical parameters, and preparation of spatial database for GIS-based modelling.

2.1 Geophysical Data

Geoelectrical resistivity experiments are based on-field measurement of ground resistivity by vertical electrical sounding (VES) [26,27]. The electrodes are configured in co-linear assemblies such as symmetrical Schlumberger and Wenner arrays or asymmetric Dipole-Dipole array. Direct Current supply is compelled to flow in the subsurface, the geological layers resist smooth flow of current, thus offering ground resistance for each observation. The apparent resistivity is obtained by multiplying ground resistance and geometrical factor (function of distance between the electrodes) at corresponding observation station.

The geophysical field data as VES was acquired at twenty-one stations located in the study area using Schlumberger configuration. The VES stations are spatially distributed over uneven topography of terrain (elevation varies between 430-690 ft above mean sea level). Four electrodes are connected with Terrameter. The potential difference (delta V) was determined between the potential electrodes in response to the direct current supply (I) injected into the ground through current electrodes. These two parameters are used to derive the ground resistance

using Ohm's law. The apparent resistivity (rho-a, also known as ground resistivity) is determined by multiplying the measured resistance and geometric constant at each observation point, as given in Equation (1).

$$\rho_a=\pi\left[\frac{\left(\frac{AB}{2}\right)^2-\left(\frac{MN}{2}\right)^2}{MN}\right]\frac{\Delta V}{I} \quad (1)$$

where, the current electrode and potential electrode separations are denoted by (AB/2) and (MN/2), respectively.

The apparent resistivity curves (field data curve) are drawn through IPIWIN software. The curves show the apparent resistivity versus current electrode separation along VES profile. The shape of the field curve as H-type, A-type, K-type and Q-type may represent different subterranean conditions [26]. The field data curves are matched with master curves in semi-automation process. The exercise of curve matching attempts to choose a geological model at best-fit match. The best model (with the least error) of the field and master curves helped to infer the characteristics of different geological layers at each VES station. The interpretation based on apparent resistivity provided thickness of each layer, lithology type, (sandstone, shale, Limestone), the thickness of the aquifer etc. The interpretation of VES curves helped us to model the subsurface geology based on resistivity ranges. The hydrogeological conditions such as salinity of groundwater increase when resistivity decreases. A community water well lies near the study area providing a ground control while interpretation of the lithologies down to 450 feet depth. The lithological units encountered in the community borehole are undertaken as benchmark to infer the lithological interpretation of VES curves modelling. The community borehole is producing sweet water from the sandstone as aquifer. The field visit and site observations suggest that the groundwater is being pumped from a confined aquifer "possible sandstone" with initial smell which indicate the water is not being charged by surface stream or tributary channel. The aquifer lithology is interpreted as sandstone at all VES stations based on contrasting resistivity measurements. The interpretation of VES curves is summarized in geoelectrical sections (graphically represent stratified geological layers). This graphical illustration of geo-electric profile is outlined by layered strata identified through electrical (resistivity) verses depth which are analogous to virtual drilling logs. Thus, the geo-electrical investigations are non-destructive drilling where each layer is discriminated by corresponding apparent resistivity.

The location of VES points (center of Schlumberger array), outer electrode spread (max.), and inferred data for each VES station are summarized in Table 1. The values of apparent resistivity for aquifer (at each VES) are ranging between 101 ohm-m and 269.5 ohm-m (Table 1).

2.2 Geospatial Data

The interpreted hydrogeophysical parameters for each VES station are processed and mapped by the using ArcMap, The interpreted hydrogeophysical variables (location of VES measurements, depth to the aquifer, aquifer resistivity, the yield of the aquifer, and thickness of aquifer) are interpolated by Kriging method. The Kriging method is helpful to generate thematic raster layers of each variable. Each cell of the raster thematic layer is reclassified and multiplied by an assigned weight. The weight of each hydrogeophysical parameters is determined as knowing its proportional influence on the suitability function. The reclassified thematic layers are integrated to

Table 1. The dataset used for mapping of aquifer extent and building the GIS-based suitability criteria.

VES ID	Latitude	Longitude	Max. VES spread (m)	Aquifer resistivity (ohm-m)	Thickness (m)	Yield (gpm)	Aquifer depth (m)	Interpreted lithologies & proposed aquifer (underlilned)
VES-1	25.042398	67.460177	300	115	49.5	155	106	Sh, LSt, Sh, Sh, **S.St,** S.St.
VES-2	25.026230	67.428244	300	101	22.7	70	54.3	Sh, Sh, Sh, **S.St,** Sh, Sh
VES-5	25.024761	67.464804	300	148	50.3	190	79.4	Sh,S.St, Sh, Sh, Sh, **S.St,** Sh
VES-7	25.006357	67.440705	300	138	50.1	210	82.3	S.St, Sh, Sh, **S.St,** Sh, Sh
VES-10	24.996018	67.438758	300	181	36.5	170	53.3	Sh, Sh, Sh, Sh, **S.St**
VES-12	24.991582	67.449782	300	122	60.5	225	94.6	LSt, LSt, Sh, **S.St,** Sh
VES-15	24.999768	67.478147	300	153	36.7	160	73.6	S.St, Sh, **S.St,** Sh, Sh
VES-17	24.986628	67.475659	300	153	65.1	190	76.2	LSt, LSt, Sh, **S.St,** Sh
VES-18	24.967666	67.455622	300	269.5	84.25	250	143.9	Sh, Sh, Sh, **S.St**, LSt

identify the most suitable area (Equation (2)):

$$S_i = \Sigma W_i . X_i \quad (2)$$

W_i= weight of factor map and X_i = criteria class score of factor map "i" and S_i = Suitability index for each pixel in the cell.

The weighted suitability analysis is done by using parametric overlay techniques [2]. For the site suitability analysis, the final map is derived by the following Equation (3):

$$S = (AE_w\, AE_R + AR_W\, AR_R + AZ_W\, AZ_R + AG_W\, AG_R) \quad (3)$$

where, S is dimensionless, representing site for new well location, AE is the aquifer depth, AR is the aquifer resistivity, AG is aquifer yield, AZ is the aquifer thickness. The subscript letter w represents the weight of each factor and R is the range of each class.

3. Results and Discussion

A correlation between interpreted results at corresponding VES stations such as VES 7, VES 8, VES 9 shows that the presence of aquifer does not extend to the east (Figure 2a). A correlation between interpreted geological layers at VES 10, 12, 17, 16 (from east to west) shows the presence of aquifer (sandstone) (Figure 2b). The sandstone (aquifer) is present at the bottom of lithology log down to 36.5-meter thick package overlain by shale bed at VES-10. In VES-12 the sandstone (aquifer) is present at the bottom of lithology log down to 60-meter thick. The same geological model extends at VES-17, sandstone aquifer is present at the bottom of the lithology log. The correlation shows thick aquifer bottom of the logs (Figure 2b). However, the interpreted aquifer at VES-16 is confined, capped by shale and limited by the underlain limestone.

The correlation of derived lithology log between VES 10, 12, 15 from east to west (Figure 2c). In VES-10 sandstone (aquifer) is present at the bottom up to 36.5-meter thick and shale is present on the top of the geoelectrical section. In VES-12 sandstone (aquifer) is also present at the bottom of lithology log it is very thick package up to 60-meter thick above aquifer shale and limestone is present. In VES-15 we identified two sandstone aquifers bifurcated by the shale bed. The aquifer present at VES-15 is confined aquifer and on the top of lithology log an unconfined aquifer is present. Figure 2d shows a co-relation between VES (1, 5, 8, 18) from North to South, which shows how aquifer is increasing towards South. In VES-1 Sandstone (aquifer) is present at the bottom of lithology log up to 105-meter, and there is a thin package present at the top of the geoelectrical section in VES-1 shale present in between limestone and sandstone (aquifer). Towards south at VES-5 two packages of aquifer are present, one is present at the top and the other one is present at the bottom of the top sandstone (aquifer) which is about 6-meter thick and at the bottom it is 50.3-meter-thick and shale is present in between these layers. Aquifer thickness is increasing towards south, where there is another very thick aquifer present at the bottom of VES-18 which is about 84 meters thick. This aquifer layer is one of the thickest aquifer of the study area, identified in between VES 5 and VES 18. An unconfined aquifer is present at the top of VES-5.

ArcMap tools are explored to facilitate in optimum site selection for locating potential water zones. which is interpolated to determine lateral extension of aquifer (Figure 3a). The interpolated maps of apparent resistivity are reclassified into five classes. The class one is indicating least suitable area (lowest resistivity), and class at rank five is assigned to the most suitable area (relatively highest resistivity of sandstone aquifer). The most suitable area surrounds VES-18 (which contain the aquifer with the highest resistivity) whereas the least suitable sites are VES-2 and VES-1 (Figure 3b). The field visits to the study area give evidence that the ground water extracted from the study area is being pumped from a confined aquifer characterized with an initial smell.

The depth to the aquifer map showcases the top of aquifer ranging from 53 meters to 143 meters (Figure 3c). The least depth is interpreted at VES-2, 15 & 10, and the deepest aquifer is present at VES-18 (Table 1). Figure 3d represents the reclassified map of aquifer depth into five classes. The value of class one is assigned to the least suitable area (deepest depth aquifer) and the most suitable site is ranked at five (shallowest aquifer) in the southern side of the study area at VES-18. The aquifer thickness map is presenting the interpolated thickness ranging from 29 meters to 77 meters (Figure 3e). The aquifer with the highest thickness is present at VES-18 and least thick is present at VES-2, though these points also contain less depth resistivity and yield values. Figure 3f shows that the class one of the least suitable area (least depth) and five indicates the most suitable (highest depth).

The aquifer yield (gallons per minute) is monitored from the pumping wells installed in the study area. The approximate location of pumping wells is correlated with the VES stations. The interpolated map of values ranging from 93 gpm to 237 gpm, which helps to know the spatial distribution of potential volume and flow dynamics of groundwater in the study area (Figure 3g). The highest yield is present at VES-12 & 18 whereas the least yield is encountered at VES-2. The reclassified map of yield classifies the area into five classes (Figure 3h). The most suitable area is classified as five and least suitable is classified as class one.

Primarily, the hydrogeological information (aquifer yield) and geophysical data (thickness, resistivity, depth)

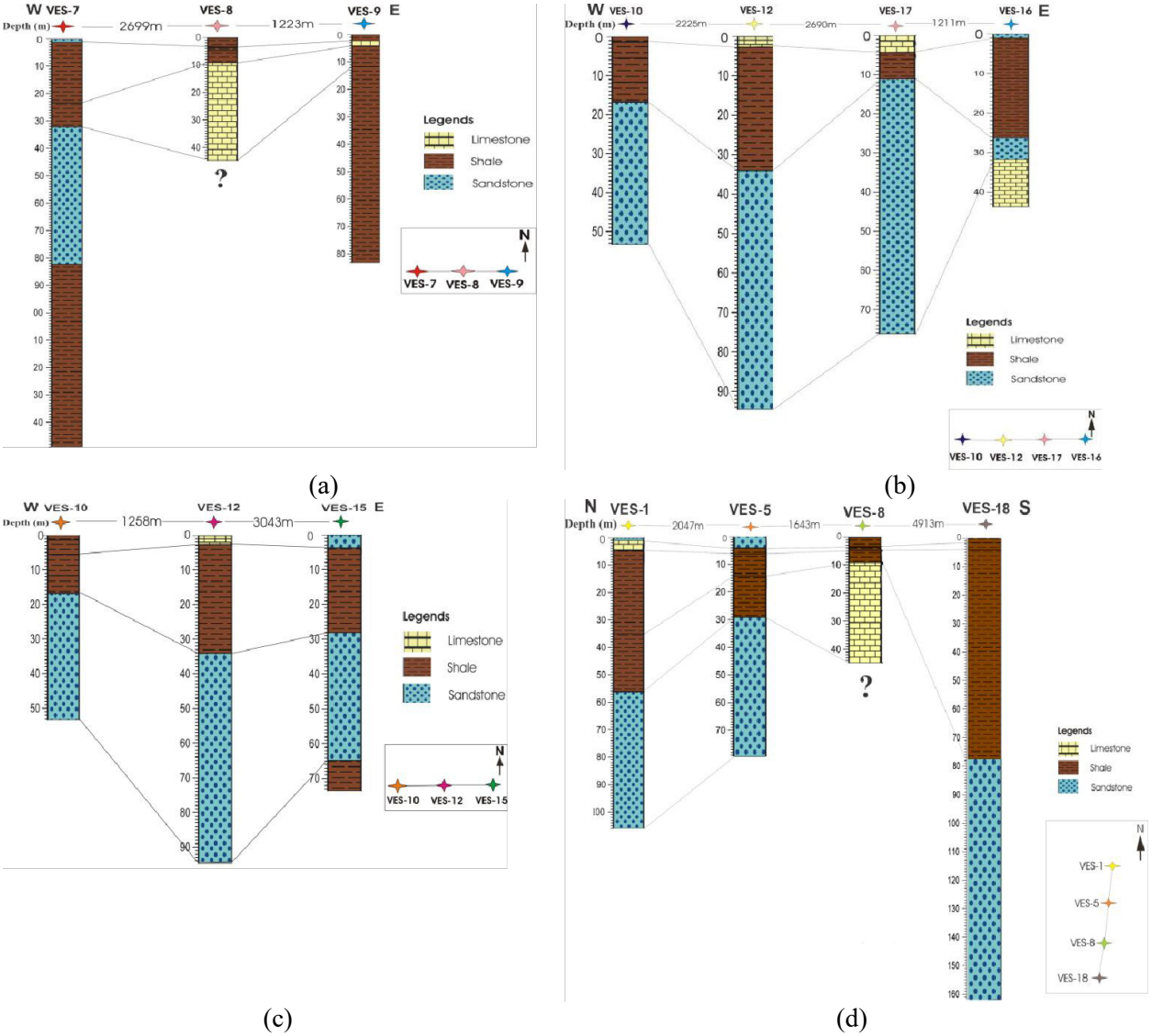

Figure 2. Geoelectrical sections presenting the interpreted lithologies and their geological correlations.

of the aquifer are used to identify the groundwater potential sites using the geospatial technique. The resultant map is prepared by defining the weight of variables. The aquifer yield is given the highest weight (40%) as an indicative of the aquifer pumping potential, the aquifer nature is represented by the resistivity, though assigned a weight of 30% as an indicator of quality of water either (fresh or saline), resistivity decreases with increases salinity of water, the thickness of the aquifer assigned a weight of 20%, however, relatively least weight i.e. 10% is assigned to the depth of aquifer because it is vital to determine cost of drilling any well. The suitable sites are mapped by weighted overlay method by assigning weight to respective variables such as aquifer yield (40%), aquifer resistivity (30%), aquifer thickness (20%), and aquifer depth (10%). The suitability analysis is done through overlay analysis of the spatially distributed variables (Figure 3).

Site suitability analysis depends on inputs variables of hydrogeophysical database, which were interpolated, reclassified, and integrated for weighted overlay analysis. The integration of the data is shown in the suitability map. The map classifies the study area into three classes (Figure 4). The suitability map showcases potential groundwater zones in the study area and provides a guide to select a site for installation of a water-well. Each pixel of the integrated raster indicates its suitability value. For instance, the pixel with a value of 3 is the most suitable area (shown in green). The similar pixel values are grouped to showcase the lateral extent of most suitable zone. The observation sites are overlaid to recognize the location of the VES point and intended drilling. The most suitable area contains multiple wells in the buffer of VES-18, 12, 17, 10, 7

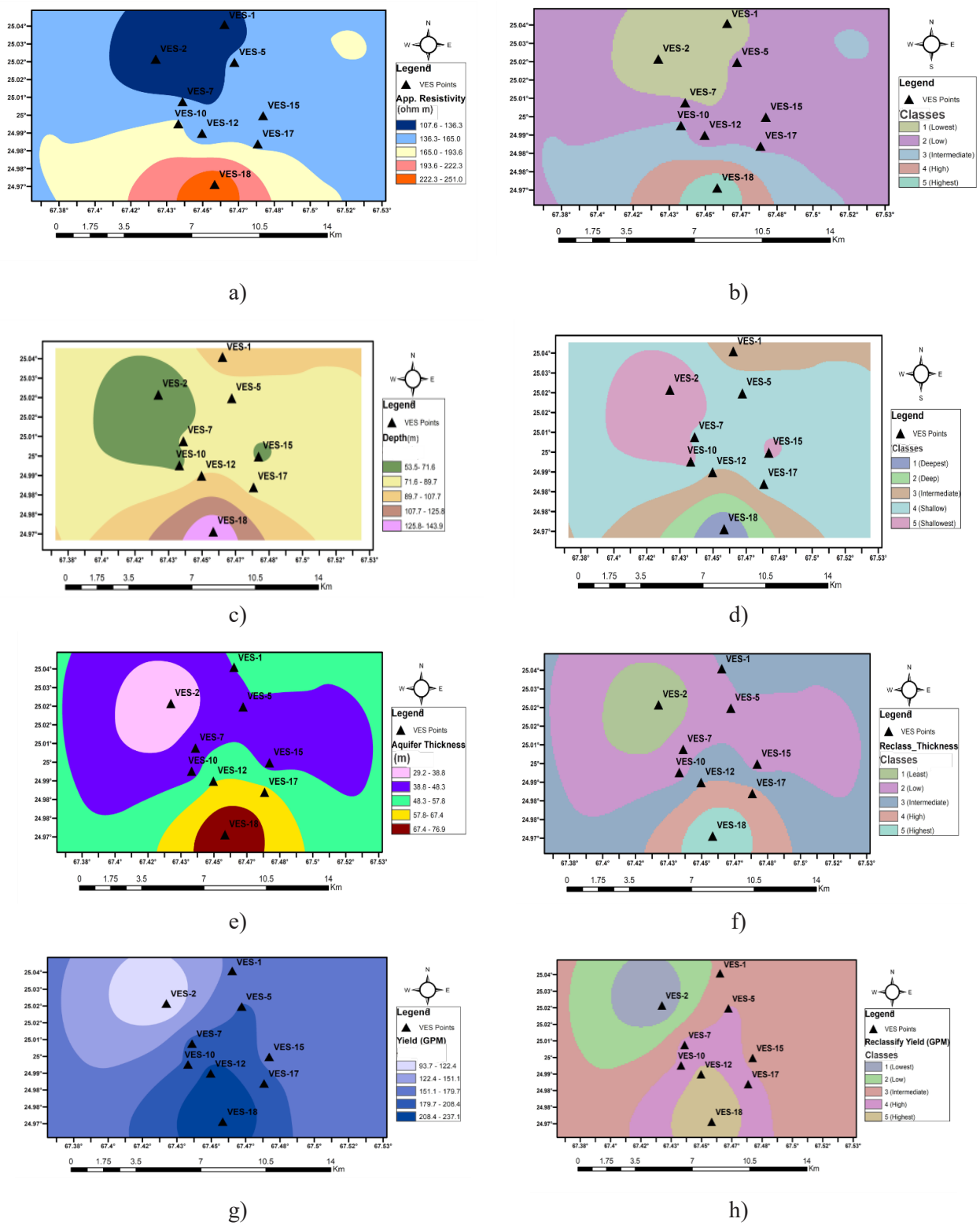

Figure 3. GIS-based maps of input variables of suitability criteria. a) Aquifer Apparent Resistivity map, b) Reclassified Apparent Resistivity map, c) Aquifer Depth map, d) Reclassified Aquifer Depth map, e) Aquifer thickness map, f) Reclassified Aquifer thickness map, g) Aquifer yield (GPM) map, h) Reclassified Aquifer yield (GPM) map.

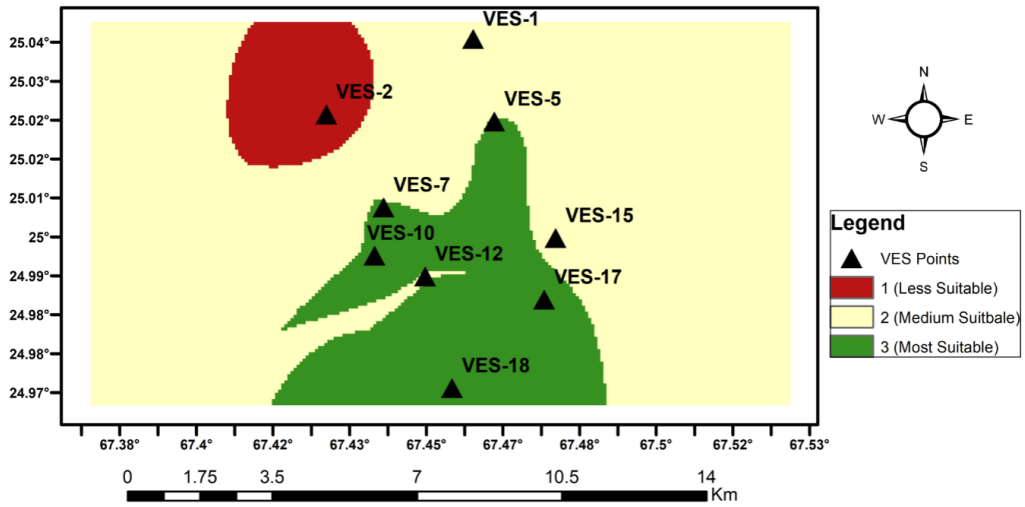

Figure 4. Groundwater potential zonation. Site suitability map is classifying the study area for locating a new well.

and 5. The least suitable area is in the vicinity of VES-2, which may be not good for drilling a water well.

4. Conclusions

The geophysical delineations of VES helped to explore the hydrogeological conditions of the aquifer in study area. It is found that the electrical resistivity methods are significant to find the aquifer characteristics. The sandstone layer was interpreted as an aquifer however, its thickness varies in its lateral extent within in hilly topography of study area. The integrated approaches of geophysical and GIS helped to integrate the multiple parameters and classify the region into potential zones. The suitable sites of potential groundwater are located in vicinity of VES 18, 12, 17, 10, 7, 5 (central-south) of the study area. The most suitable potential zone is recommended for drilling water well in the future. This study may help in cutting down the cost of water exploration projects and reduces the labor efforts in hunting possible sites for drilling a well. The integrated methodological approach of this study is recommended to utilize for locating groundwater potential zones even in rough and hilly regions.

Author Contributions

Muhammad Jahangir Khan has initiated this research work's proposal and designed the methodological workflow. Syeda Rida Fatima Bokhari and Farhad Ali assisted in the literature review, data analysis and interpretation. Umair Bin Nisar helped in the improvement of the language while proofreading of article. All authors have read and agreed to the published version of the manuscript.

Data Availability Statement

The data presented in this study are available on request from the corresponding author. Data is contained within the article.

Funding

This research received no external funding.

Acknowledgement

The authors acknowledge the worthy reviewers for their technical guidance and suggestions. We are thankful to Bahria University (Karachi Campus) for providing PPL lab facilities to conduct this study.

Conflict of Interest

The authors declare no conflict of interest.

References

[1] Li, P., Zhang, C., Li, W., et al., 2021. Groundwater vulnerability assessment of Pingtan Island in Fuzhou City, China, based on DRASLI-QUE. Journal of Hydrologic Engineering. 26(3), 05020050.

[2] Motevalli, A., Pourghasemi, H.R., Hashemi, H., et al., 2019. Assessing the vulnerability of groundwater to salinization using GIS-Based data-mining techniques in a coastal aquifer. Spatial modeling in GIS and R for earth and environmental sciences. Elsevier: Amsterdam. pp. 547-571.

[3] Pérez-Carrascal, K., García-Guarín, J., 2021. Detection of water leaks with Dowsing technique and

Reynold's transport theorem. Journal of Physics: Conference Series. IOP Publishing. (1), 012004.

[4] Mondal, N.C., Singh, V.P., Singh, V.S., et al., 2010. Determining the interaction between groundwater and saline water through groundwater major ions chemistry. Journal of Hydrology. 388(1-2), 100-111.

[5] Prasad, K.A., Gnanappazham, L., Selvam, V., et al., 2015. Developing a spectral library of mangrove species of Indian east coast using field spectroscopy. Geocarto International. 30(5), 580-599.

[6] Greer, B.M., Burbey, T.J., Zipper, C.E., et al., 2017. Electrical resistivity imaging of hydrologic flow through surface coal mine valley fills with comparison to other landforms. Hydrological Processes. 31(12), 2244-2260.

[7] Thabit, J.M., AL-Hameedawie, M.M., 2014. Delineation of groundwater aquifers using VES and 2D imaging techniques in north Badra area, Eastern Iraq. Iraqi Journal of Science. 55(1), 174-183.

[8] Kearey, P., Brooks, M., 1991. An introduction to geophysical prospecting. Blackwell: Boston.

[9] Teixidó, T., 2012. The surface geophysical methods: A useful tool for the engineer. Procedia Engineering. 46, 89-96.

[10] Stewart, M.T., 1982. Evaluation of electromagnetic methods for rapid mapping of salt-water interfaces in coastal aquifers. Groundwater. 20(5), 538-545.

[11] Khan, M.J., Shah, B., Nasir, B., 2020. GIS-based groundwater quality assessment for drinking purpose: A case study of Sindh industrial trading estate (SITE), Karachi, Pakistan. Modelling Earth Systems and Environment. 6, 263-272.

[12] Al-Ruzouq, R., Shanableh, A., Merabtene, T., et al., 2019. Potential groundwater zone mapping based on geo-hydrological considerations and multi-criteria spatial analysis: North UAE. Catena. 173, 511-524.

[13] Yin, L., Zhang, E., Wang, X., et al., 2013. A GIS-based DRASTIC model for assessing groundwater vulnerability in the Ordos Plateau, China. Environmental Earth Sciences. 69(1), 171-185.

[14] Dashtpagerdi, M.M.,Vagharfard, H., Honarbakhsh, A., et al., 2013. GIS-based fuzzy logic approach for identification of groundwater artificial recharge site. Open Journal of Geology. 3(06), 379.

[15] Ghorbanzadeh, O., Feizizadeh, B., Blaschke, T., 2018. Multi-criteria risk evaluation by integrating an analytical network process approach into GIS-based sensitivity and uncertainty analyses. Geomatics, Natural Hazards and Risk. 9(1), 127-151.

[16] Biswas, S., Mukhopadhyay, B.P., Bera, A., 2020. Delineating groundwater potential zones of agriculture dominated landscapes using GIS based AHP techniques: A case study from Uttar Dinajpur district, West Bengal. Environmental Earth Sciences. 79(12), 1-25.

[17] Metwaly, M., El-Qady, G., Massoud, U., et al., 2010. Integrated geoelectrical survey for groundwater and shallow subsurface evaluation: A case study at Siliyin spring, El-Fayoum, Egypt. International Journal of Earth Sciences. 99(6), 1427-1436.

[18] Khan, S., Nisar, U., Ehsan, S., et al., 2021. Aquifer vulnerability and groundwater quality around Brahma Bahtar Lesser Himalayas Pakistan. Environmental Earth Sciences. 80(13), 1-13.

[19] Nisar, U., Khan, M.J., Imran, M., et al., 2021. Groundwater investigations in the hattar industrial estate and its vicinity, Haripur District, Pakistan: An integrated approach. Kuwait Journal of Science. 48(1), 51-61.

[20] Aziz, N.A., Hasan, R.H., Abdulrazzaq, Z.T., 2018. Optimum site selection for groundwater wells using integration between GIS and hydrogeophysical data. Engineering and Technology Journal. 36(6 Part (A) Engineering), 596-602.

[21] Abdalla, O.A., Ali, M., Al-Higgi, K., et al., 2010. Rate of seawater intrusion estimated by geophysical methods in an arid area: Al Khabourah, Oman. Hydrogeology Journal. 18(6), 1437-1445.

[22] Olusola, F.O., Marvellous, O.O., 2020. Groundwater vulnerability mapping and quality assessment around coastal environment of Ilaje local government area, southwestern Nigeria. International Journal of Earth Sciences Knowledge and Applications. 2(2), 74-91.

[23] Khan, M.J., Zeeshan, M., Ali, S.S., 2020. GIS-based change detection of coastal features along Karachi Coast, Pakistan. Pakistan Journal of Science. 72(2), 124-133.

[24] Zafar, S., Zaidi, A., 2019. Impact of urbanization on basin hydrology: A case study of the Malir Basin, Karachi, Pakistan. Regional Environmental Change. 19(6), 1815-1827.

[25] Salma, S., Shah, M.A., Rehman, S., 2012. Rainfall trends in different climate zones of Pakistan. Pakistan Journal of Meteorology. 9(17).

[26] Xie, J., Cui, Y.A., Fanidi, M., et al., 2021. Numerical modeling of marine self-potential from a seafloor hydrothermal ore deposit. Pure and Applied Geophysics. 178(5), 1731-1744.

[27] Sato, M., Mooney, H.M., 1960. Electrochemical mechanism of sulphide self-potentials. Geophysics. 25, 226-249.

Earth and Planetary Science
https://ojs.nassg.org/index.php/eps/index

CASE REPORT

Evaluation of Wellbore Stability by Analytical and Numerical Methods: A Case Study in a Carbonate Oil Field

Faramarz Abazari[1] Hossein Jalilifar[1] Mohammad Ali Riahi[2*]

1. Department of Mining and Petroleum, Shahid Bahonar University of Kerman, Iran
2. Institute of Geophysics, University of Tehran, Tehran, Iran

ARTICLE INFO

Article history
Received: 22 April 2022
Revised: 21 May 2022
Accepted: 25 May 2022
Published Online: 2 June 2022

Keywords:
Drilling mud window
Failure criteria
Minimum and maximum mud pressure
Wellbore stability

ABSTRACT

The instability of the wellbore has significant effects on drilling, causing delays in operations, increasing costs, and ultimately may result in the abandonment of wells. Nowadays, it is possible to stabilize a wellbore by changing the drilling mud composition. With the help of rock mechanics and knowledge of the mechanical properties of the formation, the optimal path for the drilling of the well and the window of the mud is determined. Several features of the formation are influential in wellbore design; knowing these features is necessary for designing optimal mud weight to ensure wellbore stability. In practice, analytical methods for the calculation of the optimal mud weight are more convenient than numerical ones because the latter needs information on many samples that are usually unknown at the commencement of the project. This research investigates the wellbore stability in the Kupal carbonate oil field using an analytical method with three rock strength criteria of Mogi-Coulomb, Mohr-Coulomb, and Hoek-Brown failure. The authors conclude that the Mogi-Coulomb criterion predicts a minimum drilling mud pressure and is more conservative. This is due to the use of its intermediate stress.

1. Introduction

Underground formations always suffer from vertical compression stresses (upper layer weights) and horizontal stresses (lateral strain range) loads. The drilling operation perturbs the natural stress balance in the rocks and generates a high risk in terms of pollution, fueling climate change, disrupting wildlife, and damaging public lands [1]. When a well is drilled, the equilibrium of the area in which it is drilled is disturbed. The wellbore around it tries to restore the balance of the stress field. As a result, stress concentrations are created around the wellbore and penetrated the formation. In the absence of stability, there will be a failure in the wellbore and formation [2]. We need a deterrent as a pressure compensator to prevent the breakdowns, which is mainly the fluid (drilling mud) hydrostatic pressure. Zhang et al., (2009) [3] examined five failure criteria on various rock specimens to determine the best

*Corresponding Author:
Mohammad Ali Riahi,
Institute of Geophysics, University of Tehran, Tehran, Iran;
Email: mariahi@ut.ac.ir

DOI: http://dx.doi.org/10.36956/eps.v1i1.524

Copyright © 2022 by the author(s). Published by Nan Yang Academy of Sciences Pte. Ltd. This is an open access article under the Creative Commons Attribution-NonCommercial 4.0 International (CC BY-NC 4.0) License. (https://creativecommons.org/licenses/by-nc/4.0/).

criterion for the wellbore stability analysis. Accordingly, they concluded that the 3D Hoek-Brown and the Mogi-Coulomb criteria are appropriate for wellbore stability analysis [3-5]. Al-Ajmi and Zimmerman (2006) [4] proposed using the Mogi-Coulomb criterion to predict the brittle shear failure of rocks. This criterion was shown to accurately model laboratory failure data on a range of different rock types McLean and Addis (1990) [6]. Using this Mogi-Coulomb criterion, they developed improved stability models for vertical, horizontal, and deviated boreholes [7]. Chatterjee and Mukhopadhyay (2003) [8] used ANSYS finite element software and investigated stress around a wellbore to study the effects of fluid pressure during drilling. Hoang et al. (2004) [9] investigated wellbore stability in multilateral junctions using the finite element method. They showed that the orientation of junction and in situ stresses both have a significant impact on well completion and stability. Salehi and Hareland (2010) [10] investigate wellbore stability in underbalanced drilling concerning equivalent circulating density with both Finite Explicit and finite-Element codes to cross-check the results [11,12].

In this paper, we have first used the Hoek-Brown, Mohr-Coulomb, Mogi-Coulomb, criteria to determine the optimum drilling direction and mud pressure for a wellbore located in the Kupal carbonate oil field. Then the finite difference method was used to show the validation and accuracy of predicted mud pressure and investigate the wellbore stability in different vertical, horizontal, and deviated states. The Kupal oil anticline is one of the most important structures in the Dezful embayment that is located northeast of the Ahvaz city and north of the Marun oil field. Recent deposits and Lahbari members of the Aghajari formation have formed the surface outcrops, and the Asmari formation with seven reservoir layers is the main reservoir rock in this oil field.

2. General and Geomechanical Information on the Kupal Carbonate Oil Field

The Kupal field is one of the Iranian oil fields. which is located in Khuzestan province and Haftkel city capital of Haftgel County. The length of this square is 39 km and its width is 4 km. The average crude oil production capacity of the Kupal field is equal to 91,000 BPD of crude oil, which is made through thirty-two active wells in the Asmari and Bangestan reservoirs of this field. The Kupal oil anticline is a fault-related (detachment fold) and asymmetric fold, in which the middle parts have been distinguished as potential zones of dense fracture development due to longitudinal curvature. The southwest limb in many parts and the northeast limb in the middle parts indicate zones with high fracture density, and the axial bending of the Kupal anticline is a result of the movement of deep faults. In situ stresses, geomechanical, and fluid flow information related to the Kupal carbonate reservoir in the wellbore at the depth of 3791 m are listed in Tables 1 and 2 [12].

Table 1. In situ stress and geotechnical parameters for wellbore stability analysis in the Kupal oil field [12].

Wellbore parameters	Value
Overburden Stress (MPa)	96.7
Maximum Horizontal Stress (MPa)	59.4
Minimum Horizontal Stress (MPa)	44.5
Cohesion (MPa)	27
Friction Angle (deg.)	40
Poisson's ratio	0.3
Density (gr/cm^3)	2.7
Young's modulus (GPa)	44
m_i	31
mb	11
S	0.036
D	0
GSI	70

Table 2. Parameters of formation fluid flow [12].

Pore pressure (MPa)	31.1
Permeability (md)	3
Porosity (%)	8
Oil density (gr/cm^3)	0.692
Fluid modulus (GPa)	0.63

3. Rock Strength Criteria

Mogi-Coulomb criterion

The Mogi-Coulomb model is an extension of the Mohr-coulomb criterion for predicting a failure condition in a 3D stress plane in the true triaxial test space. Mogi in 1971 carried out a polyaxial experiment and deduced that for several rock types the intermediate principal stress influences the rock strength. Therefore, while a fracture is generated, it will be in the direction of intermediate principal stress along a plane [4].

Mohr-Coulomb criterion

Mohr-Coulomb criterion model is based on the 2D Mohr's stress circle, which has been in for analyzing rock failure. Coulomb concluded that failure will occur along a plane due to shear stress acting on the plane. According to Coulomb's failure theory, the required compressive stress for failure will be increased linearly by increasing the confining stress [13,14].

Hoek-Brown failure criterion

The Hoek-Brown Failure criterion was developed to predict the ultimate strength of intact rocks and rock masses. Over the years, it has been adapted to specific rock masses and modified to fit non-linear models. It gives a more practical estimation of rock strength compared to the Mohr-Coulomb criterion. It can be used to calculate the mud pressures corresponding to the lower and upper stable mud weight windows [15,5].

4. Wellbore Stability Analysis by Analytical Method

For this analysis, parameters such as Young's modulus, Poisson's coefficient, pore pressure, main stresses, constant coefficients of rock material, etc. Are obtained from well charts and analysis of laboratory cores that are used to calculate the pressure and weight of the well Drilling is required. Rock failure is a very complicated process that is still not fully understood. To further simplify the analysis, it is assumed that the homogeneous and isotropic rocks and the pressure profile of the well are assumed to be the same.

To calculate the main stresses, these steps are done using coding in MATLAB software and predict the pressure, and weight of drilling mud in different directions of the well to prevent the instability of the wellbore, the results are presented in the of form three-dimensional and two-dimensional shapes and tables.

A field study was conducted on a carbonate formation in the Kupal carbonate oil reservoirs, in which a well with a pressure of 40 MPa and a weight of 42.29 (PCF) was drilled successfully and no reports of instability were provided.

Figure 1 shows the minimum required pressure and weight of mud for different wells for the Hoek-Brown, Mohr-Coulomb, and Mogi-Coulomb criteria. The results are about 3791 (m) deep. In the Hoek-Brown and Mogi-Coulomb criteria, the minimum drilling mud pressure increases with increasing azimuth and well deviation, because if we continue with drilling operations with the same pressure in the vertical section of the well, because the vertical stress is more than two horizontal stresses may cause the failure to a wellbore. But in the Mohr-Coulomb test, this pressure is reduced from a deviation angle of 20 degrees, which may be due to the tensile strength considered by this criterion. The Hoek-Brown criterion predicts that the single axial compressive strength of the rock, the minimum pressure, and the weight of the mud for drilling are more than Mohr-Coulomb, with an increase in the angle of deviation close to the Mogi-Coulomb criterion. The Mogi-Coulomb criterion estimates the minimum pressure fluctuation of more than two other criteria, which indicates that the intermediate stress affects the estimation of the minimum pressure and provides a better prediction of the pressure of the mud as a result, the minimum pressure and mud weight required is affected by the wellbore.

Figure 2 shows the maximum pressure and mud weight required for different aspects of the well based on Hoek-Brown, Mohr-Coulomb, and Mogi-Coulomb criteria. The results are about 3791 (m) deep. In all three criteria, the maximum pressure and the weight of the drilling mud decrease with increasing azimuth and the deviation angle of the wellbore, because if the pressure and the weight of the mud that is drilled in the vertical part of the wellbore, the deviated part of the wellbore are drilled with the same amount of pressure and weight mud. Due to the difference in the values of minimum and maximum horizontal stresses is that the wellbore suffers from tensile failure in the direction of the minimum horizontal stress, which causes the mud loss and blow out of the well.

In Figure 3, the minimum drilling mud pressure and the angle deviation of wells in the azimuths of 0° and 90° for the three criteria of the Mogi-Columbus Mohr-Columbus, and Hoek-Brown defects, are shown. The Mogi-Coulomb failure criterion predicts the maximum, minimum pressure, while the Mohr-Coulomb criterion advances the minimum, minimum pressure and decreases from a further 20 degrees to a further angle, which can be due to the tensile strength this is a failure criterion. Because the value of the lower limit of drilling mud pressure is close to and even less than the pore pressure, the closeness of the horizontal stress to the minimum horizontal stress is minimal. Therefore, in this condition, horizontal drilling (sub-equilibrium) is difficult and not recommended. In general, if the horizontal tension is at a maximum near vertical stress, the drilling mud safety window margin is wider and horizontal drilling is better and easier and recommended. Conversely, if the horizontal stress is at a maximum from the vertical stress and in other words near the horizontal stress is minimal, the drilling mud safety window margin is smaller and narrower, and the amount of the bottom of the drilling mud pressure is close to and even lower than the pressure. Drilling is difficult and not recommended.

In Figure 4, the maximum drilling mud pressure is shown in the wells in the azimuths of 0° and 90° for the three criteria of the Mogi-Coulomb, Mohr-Coulomb, and Hoek-Brown defects. The Hoek-Brown failure criterion predicts the highest maximum pressure in azimuth at 90°, and the Mogi-Coulomb criterion predicts the maximum peak pressure. The Mohr-Coulomb and Hoek-Brown benchmarks are close at 90° azimuth. The Mogi-Coulomb

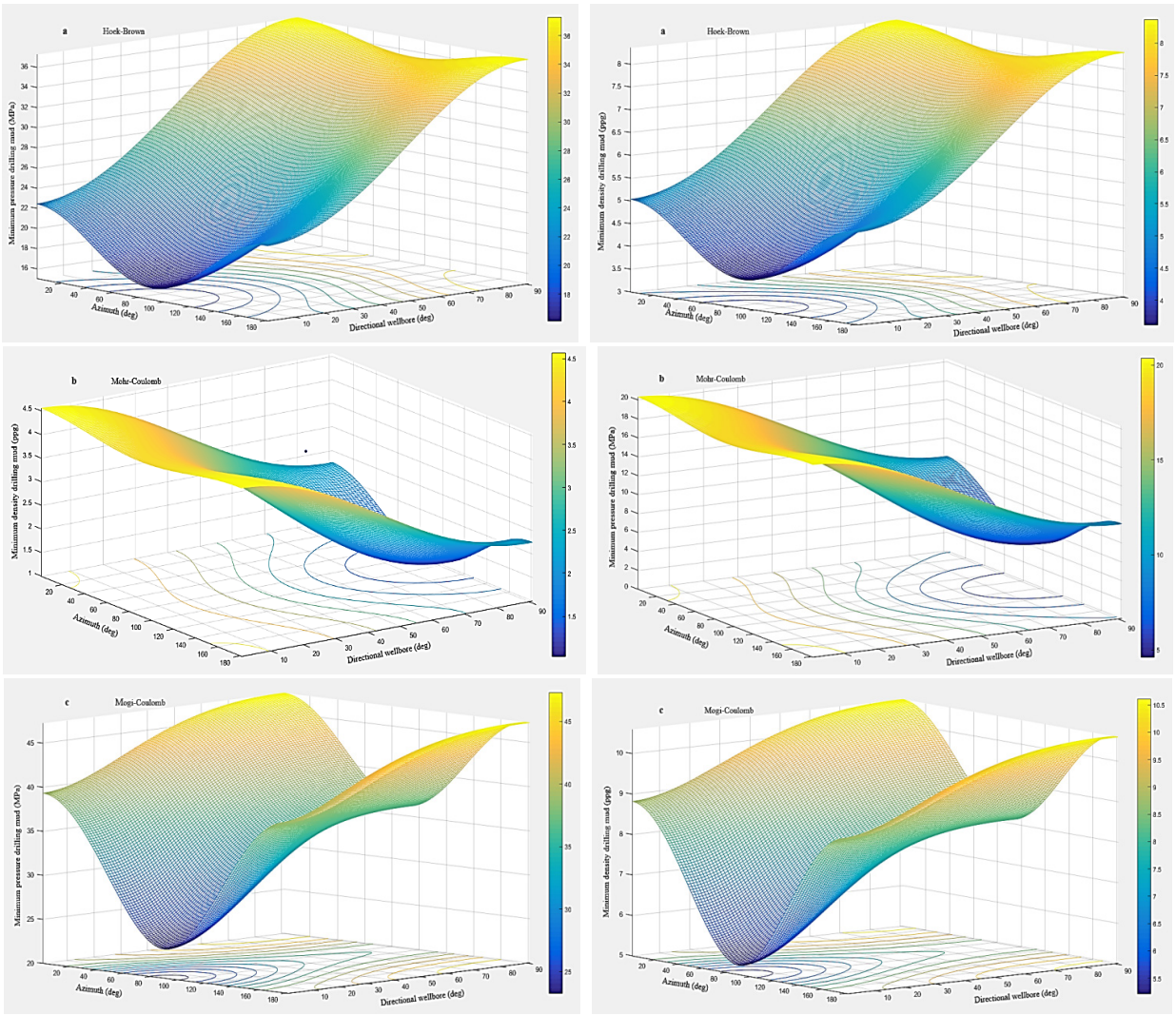

Figure 1. Minimum pressure and weight mud requirements based on azimuth and wellbore angle deviation using a) Hoek-Brown, b) Mohr-Coulomb and c) Mogi-Coulomb.

criterion in the azimuth 0° to the deviation angle of 30° is the maximum, maximum pressure of the mud and from this angle, then, predicts the minimum, maximum pressure of the mud. From a deviation angle of 30 degrees, the Hoek-Brown criterion predicts the maximum peak pressure. Therefore, the Mogi-Coulomb criterion is better than the other two criteria, because, in terms of tensile failure, the wellbore is safer.

Figure 5 shows drilling mud safety window the Hoek-Brown (a), Mohr-Coulomb (b), and Mogi-Coulomb (c and d) criteria are based on the angle of deviation and azimuths of 0, 30, 45, 60, and 90 degrees than for the Mogi-coulomb criterion separate shows the minimum and maximum differential pressure graphs. Based on this form, at zero angle of deviation, the pressure range of drilling mud is high due to the overcoming of shear failure due to the vertical deformation and with the deviation of the well from the vertical position, this area becomes smaller so that the well is deviated from the vertical state, the horizontal stresses of the vertical stress and therefore, if the minimum pressure is not increased, by increasing the angle of the deviation of the well, causing the wellbore shear failure, and if the maximum pressure of the mud does not decrease, by increasing the angle of the deviation of the well, the tensile deflection of the wellbore is in line with the minimum horizontal tension, and the loss of mud and eventually blow out in the wellbore.

To validate these models, the criteria are evaluated on a wellbore that has been successfully excavated.

Figure 5, as mentioned above, shows the minimum pressure and mud weight in terms of the deviation angle and azimuth at a depth of 3791 (m). The Mogi-Coulomb criterion predicts the highest minimum pressure and drilling mud weight, while the Mohr-Coulomb predicts the

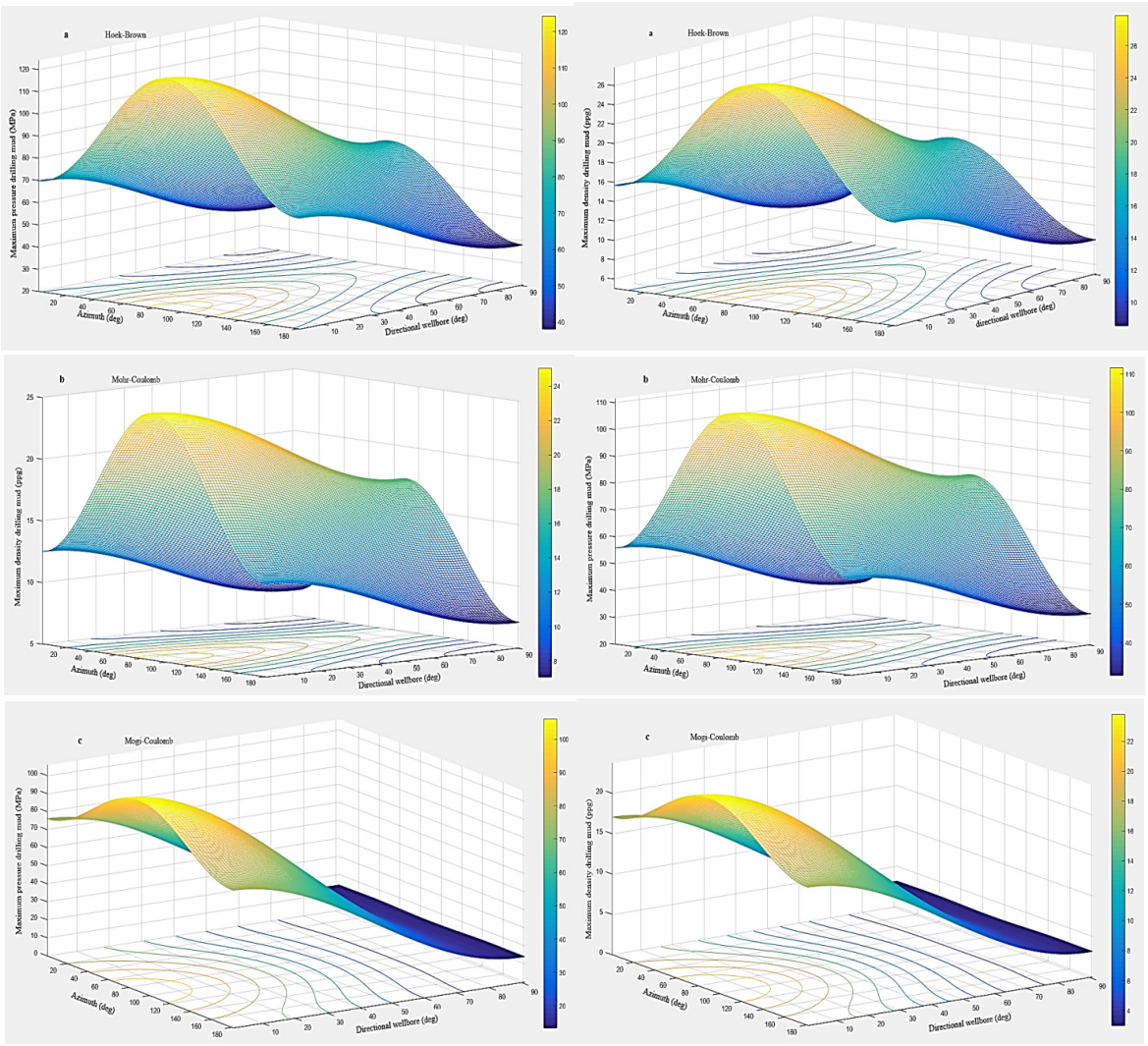

Figure 2. Maximum pressure and the mud weight requirements based on azimuth and wellbore angle deviation using a) Hoek-Brown, b) Mohr-Coulomb and c) Mogi-Coulomb.

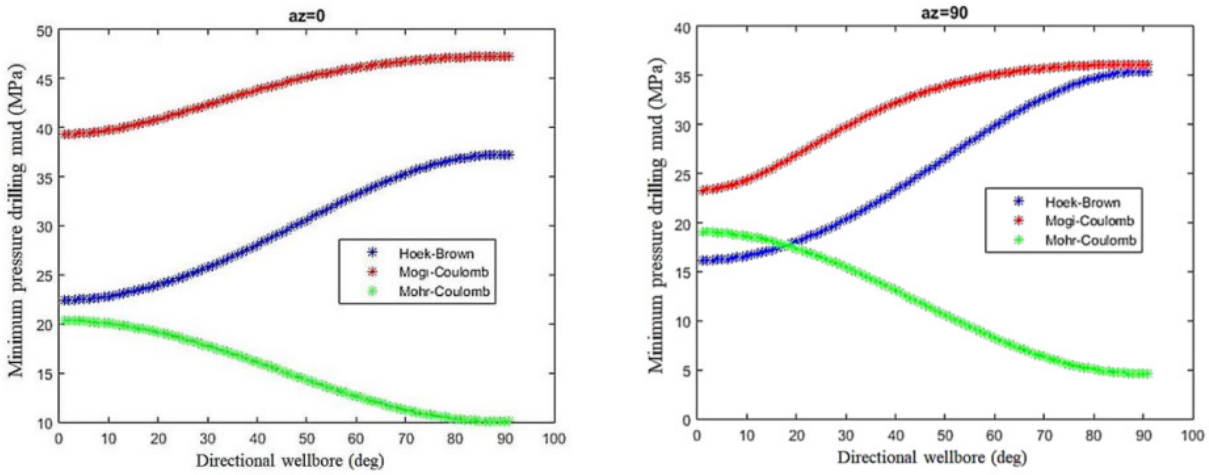

Figure 3. Minimum drilling mud pressure is predicted at 0 and 90 degrees azimuths.

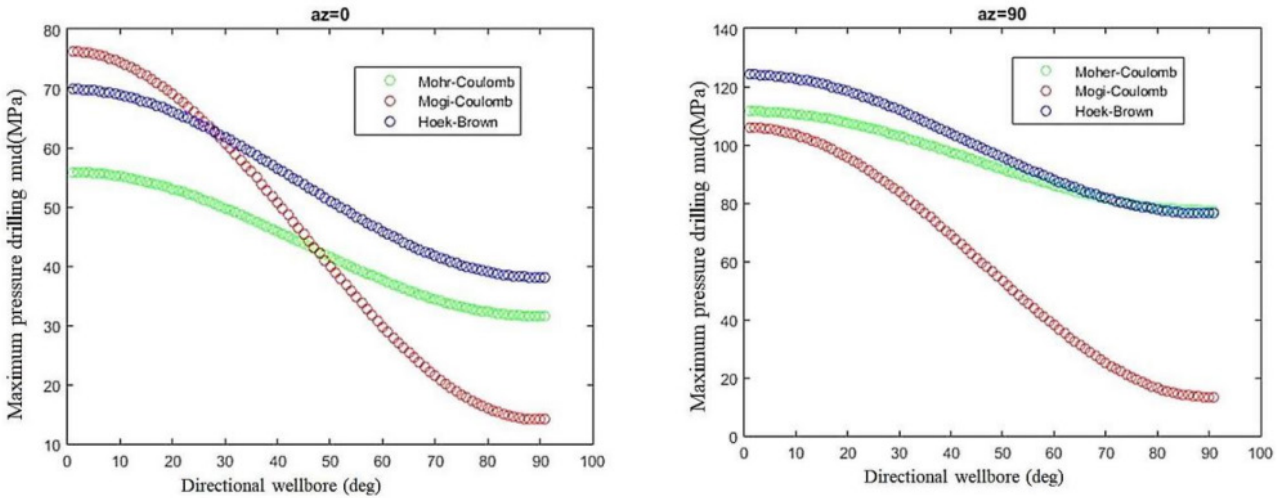

Figure 4. Maximum drilling mud pressure is predicted at 0 and 90 degrees azimuths.

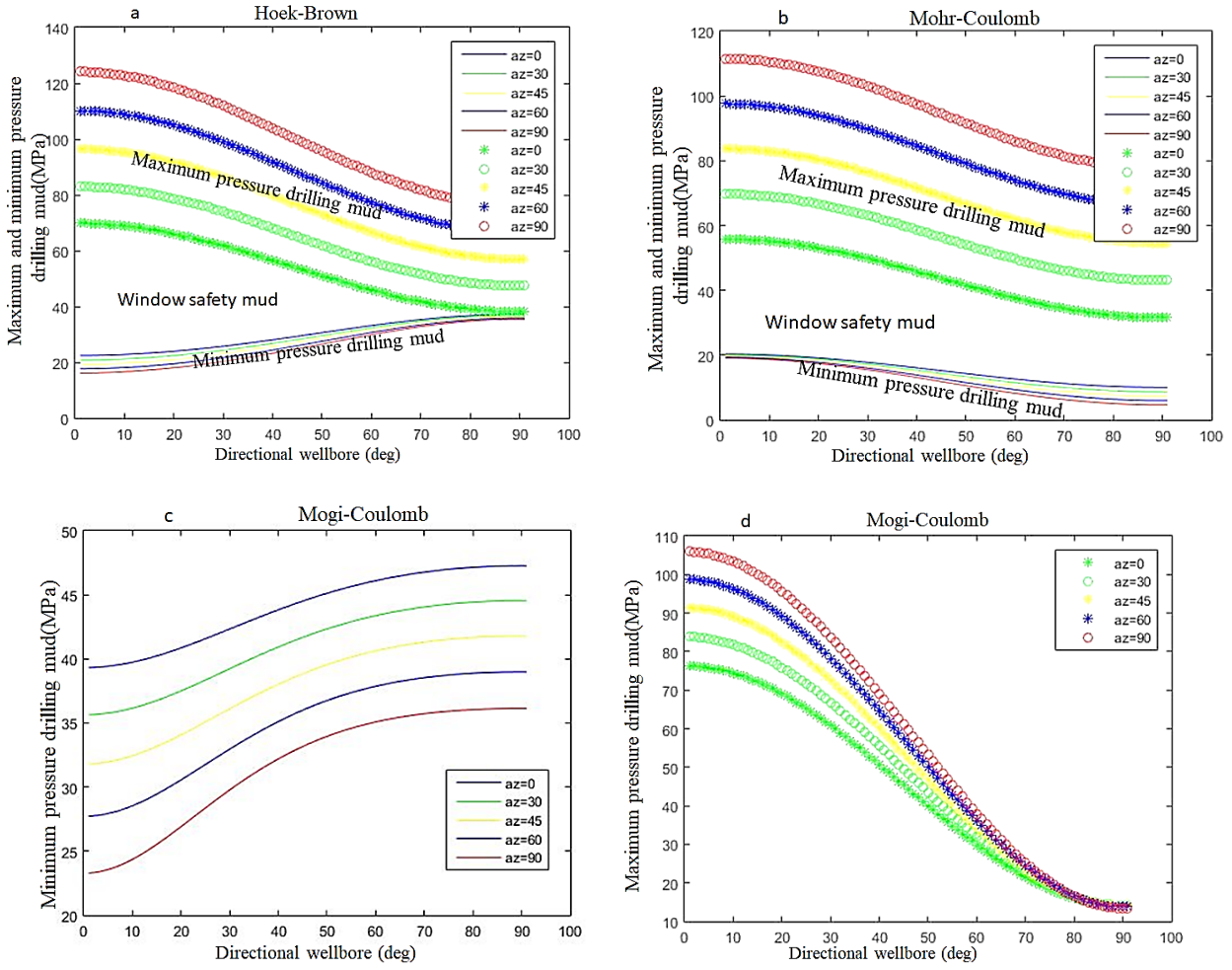

Figure 5. Safety mud window drilling pressure requirements based on azimuth and wellbore angle deviation using a) Hoek-Brown, b) Mohr-Coulomb, c and d) Mogi-Coulomb.

least. The Hoek-Brown criterion predicts the minimum pressure and the weight of the drilling mud more than Mohr-Coulomb and less than the Mogi-Coulomb and approaches the Mogi-Coulomb scale by increasing the angle of the deviation. By using the Mogi-Coulomb criterion, in the vertical state, the minimum pressure of the predicted mud weight was 39.33 (MPa) and 28.93 (PCF), respectively. This value is 0.492 (PCF) less than the actual value, and the reason why it is less than the drilling mud pressure that in the field can be applied is that the safety pressure is usually considered to be 150 (psi) to 200 (psi) higher than the pressure applied to the field, they are.

The reason for the difference between the Mogi-Coulomb criteria with both the Hoek-Brown and the Mohr-Coulomb criterion is that the Mogi-Coulomb criterion, considers medium and intermediate stresses for determining the trajectory, pressure, and mud weight. Therefore, the predicted rock resistance using Mogi-Coulomb is closer to the actual field value. As a result, the predicted mud pressure by Mogi-Coulomb to keep the wellbore stability is more than the values predicted by the Mohr-Coulomb and Hoek-Brown criteria. Thus, the Mogi-Coulomb criterion is more realistic and more conservative in the wellbore stability analysis. In contrast to the Mohr-Coulomb and Hoek-Brown criteria, only minimum and maximum stresses, as well as the Mohr-Coulomb tensile strength and the Hoek-Brown criterion, consider single-axial compressive strength of rock and assume that moderate stress has no effect on rock resistance As a result, the predicted rock resistance is less than the actual rock resistance. Therefore, the Mohr-Coulomb and Hoek-Brown criteria predict a minimum pressure drop for the wellbore wall. The Hoek-Brown criterion for predicting single-axial compressive strength predicts a minimum amount of drilling and weight mud compared to the Mohr-Coulomb criterion. In summary, the minimum and maximum predicted fluctuation pressure is given by three criteria at a depth of 3791 (m) in Tables 3 and 4.

The safety window and the optimum drilling mud are a range of drilling mud pressures that, if the pressure is low, shear failure wellbore, and if the pressure is higher than this range, the tensile fracture occurs in the wellbore.

Figure 6 shows the radial and tangential stresses around the wellbore. These stresses are not affected in a 6-radius wellbore ($\sigma_\Theta - \sigma_r = 0$). Increasing pressure and hydraulic weight of drilling fluid (drilling mud), causes increased radial stress and decreased tangential stress. Also, decreased deferent two stress and this deferent stresses caused more stable wellbore.

Table 3. Comparison of three rock failure criteria in the vertical wellbore.

Rock failure criteria	Predicted minimum mud pressure (MPa)	Predicted maximum mud pressure (MPa)
Hoek-Brown	29.43	69.86
Mohr-Coulomb	24.34	55.87
Mogi-Coulomb	39.33	76.24

Table 4. Comparison of three rock failure criteria in the horizontal wellbore.

Rock failure criteria	Predicted minimum mud pressure (MPa)	Predicted maximum mud pressure (MPa)
Hoek-Brown	37.26	38.09
Mohr-Coulomb	24.03	31.56
Mogi-Coulomb	47.27	56.4

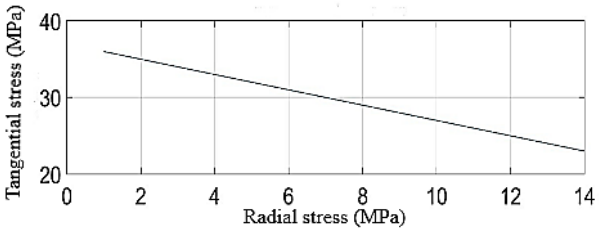

Figure 6. The radial and tangential stresses around the wellbore.

Figure 7 shows the maximum and minimum pressure of drilling mud that takes the shear stress to zero and applies the main stresses 1, 2, and 3 showing the angle of deviation of the well. By increasing the deflection angle, the maximum drilling mud pressure decreases. And the minimum mud pressure, should be increased by increasing the deflection angle of the well, but due to the proximity of stresses main 2 and 3 to each other minimum drilling mud pressure decrease with increasing deflection angle and sub-equilibrium drilling from angle deviation of 30 degrees to the horizontal position is difficult and not recommended; Because the minimum flower pressure is close to or smaller than The pressure is porous. Therefore, the closer the maximum horizontal stress is to the vertical stress, the range of the flower safety window drilling is larger and wider, and conversely, the farther the horizontal stress is from the maximum vertical stress. In other words, if the maximum the closer the horizontal stress is to the minimum horizontal stress, the smaller and more limited the safety range of the drilling mud.

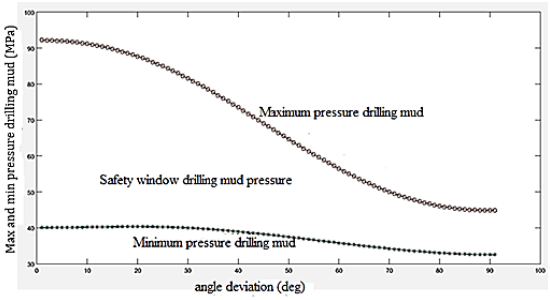

Figure 7. Changing the mud safety window according to the angle of deviation of the well by applying stresses.

According to the Mogi-Coulomb standard tables, the highest pressure and weight of drilling mud are predicted, but according to the drilling mud pressure drilling in this field, which was carried out at a pressure of 40 MPa and no instability was reported. The Mogi-Coulomb criterion is therefore the best failure and more conservative criterion and is recommended for drilling operations and this can be due to the average and medium stress used in this criterion.

5. Analysis of Wellbore Stability Using Boundary Elimination Method

Figure 8 shows the model geometry that the dimensions of the model are 1.5 × 1.5 m and the border elimination is 40 40 40 and the radius is 0.1 m.

The next step is to select the model and apply the properties of the materials. In this model, there are two criteria for Mohr-Coulomb failure Hoek-Brown is used to study the behavior of the rock and determine the stress around the well and the safety factor.

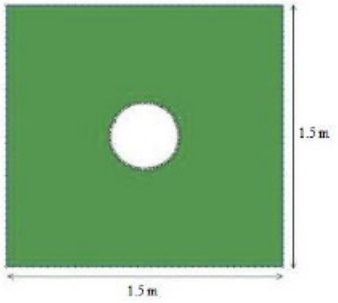

Figure 8. The model geometry that the dimensions of the model are 1.5 × 1.5 m and the border elimination is 40 40 40 and the radius is 0.1 m.

In this model, initially, the vertical stress at a depth of 3791 meters is equal to 96.7 MPa, which is perpendicular to the axis of the well (vertical well) have been. Also, the maximum horizontal stress was equal to 59.4 MPa along the x-axis, and the minimum horizontal stress equal to it was 44.5 MPa along the y-axis. The created well with a diameter of 0.2 m is subjected to internal pressure Pw and then the stability of the horizontal well in the direction of minimum and maximum horizontal stress is analyzed.

Using Examine 2D software, wall displacements, main stresses, mean, safety factor and other parameters required for well stability analysis can be examined. In this study, the wall stability well has been inspected based on safety factors.

Figure 9 shows the safety factor for different pressures applied to the inner wall of a vertical well. These images were created by applying the Hoek-Brown refractive index parameters with zero wellbore wall internal pressure.

Shear failure occurs and causes internal collapse due to increasing internal pressure. The pressure of 31 MPa is stabilized in the wellbore wall which enters the threshold of the drilling fluid safety window and until pressure is applied 56 MPa reaches the end of this window and at a pressure of 57 MPa, small cracks begin to form in the wall. Further increase in internal pressure (for example, 100 MPa) causes tensile failure in the wall and ultimately waste drilling fluid and well wall instability occurs. So the mud window safety window that failed this criterion comes in a pressure range of at least 31 MPa and a maximum of 56 MPa.

Figure 10 shows the safety factor for different pressures applied to the inner wall of a vertical well. These images were created by applying the Mohr-Columbus refractive index parameters with zero wellbore wall internal pressure. Shear failure occurs and causes internal collapse due to increasing internal pressure; so in Pressure of 25 MPa stabilized well wall that enters the threshold of the drilling fluid safety window and until pressure is applied 61 MPa reaches the end of this window and at a pressure of 62 MPa, small cracks begin to form in the wall.

Further increase in internal pressure (for example, 100 MPa) causes tensile failure in the wall and ultimately wastes drilling fluid, and wellbore wall instability occurs. So the mud window safety window failed this criterion. It comes in a pressure range of at least 25 MPa and a maximum of 61 MPa.

Figure 11 shows the safety factor for different pressures applied to the inner wall of a horizontal wellbore. These images were created by applying the Hoek-Brown refractive index parameters. At a pressure of 46 MPa, the wellbore wall is stable, indicating the entrance to the threshold of the drilling mud safety window, and at a pressure of 50 MPa, this window ends Finds. At pressures higher than this amount, small cracks are created in the wall and further increase the internal pressure it causing tensile failure in the wall, which ultimately causes drilling fluid waste and instability of the wellbore wall.

The drilling fluid safety window obtained from this failure criterion for the model has a compression range of

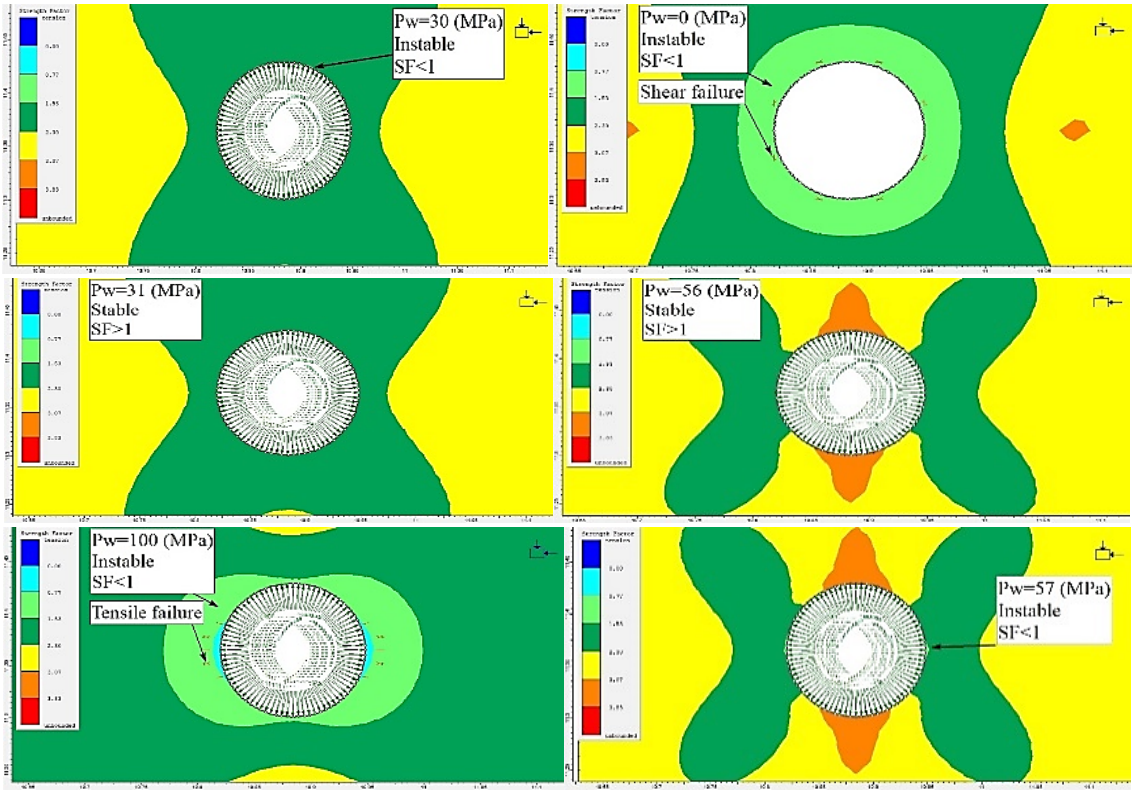

Figure 9. Changes in the safety factor of drilling fluid by applying different internal pressures to the wall of the vertical well (Hoek-Brown).

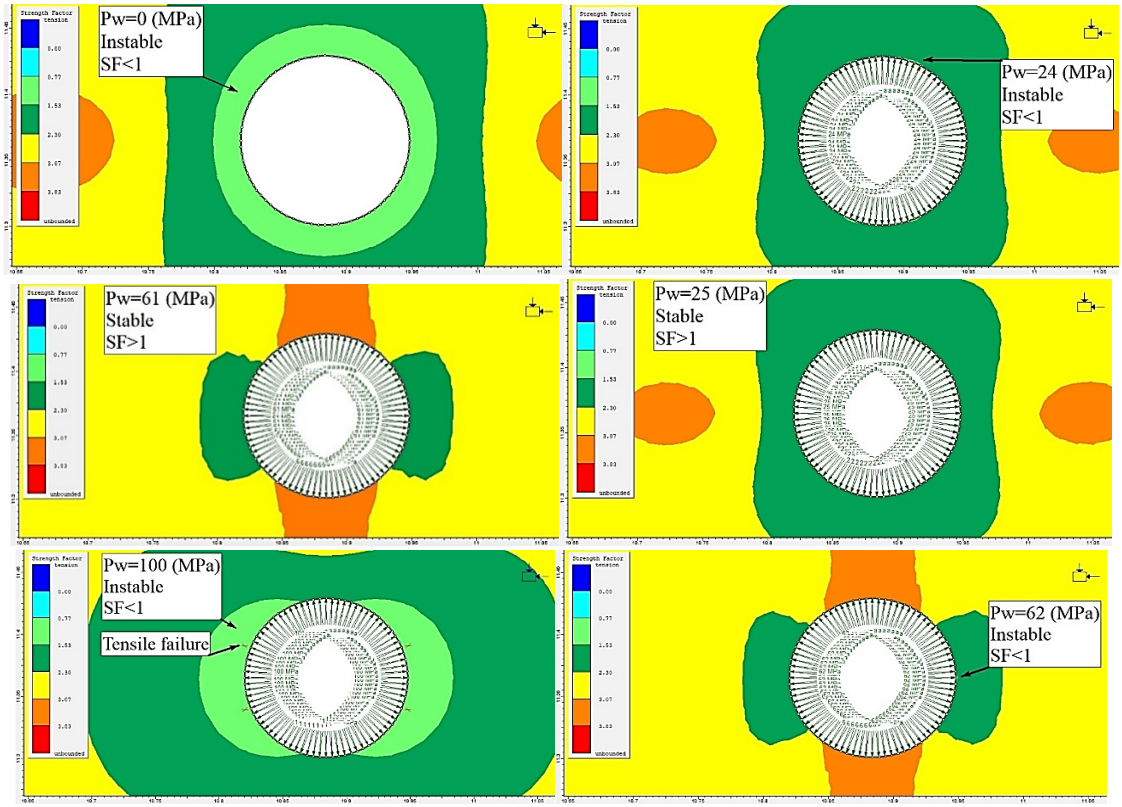

Figure 10. Changes in the safety factor of drilling fluid by applying different internal pressures to the wall of the vertical well (Mohr-Coulomb).

at least 46 to 50 MPa.

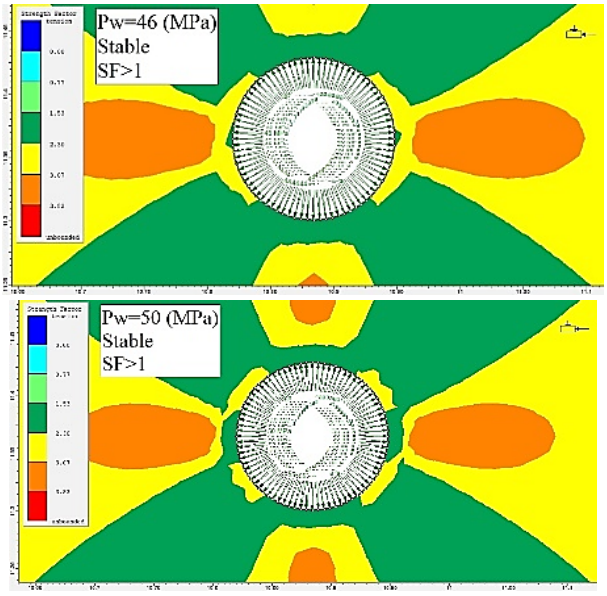

Figure 11. Changes in the drilling fluid safety factor by applying different internal pressures to the horizontal well wall (Hoek-Brown).

Figure 12 shows the safety factor for different pressures applied to the inner wall of a horizontal wellbore. These images were created by applying the Mohr-Columbus refractive index parameters. At a pressure of 43 MPa, the wellbore wall stabilized, which indicates the entrance to the drilling mud safety window threshold, and up to a pressure of 57.5 MPa.

The window continues and at higher pressures, small cracks appear in the wellbore wall. Further increase of internal pressure causes tensile failure in the wellbore wall and ultimately causes drilling fluid waste and instability of the wellbore wall; so the drilling fluid safety window obtained from this failure criterion for the model has a compression range of at least 43 MPa and a maximum of 57.5 MPa.

Figure 13 shows the internal wall pressure at a depth of 3791 m, 200 psi greater than the pore pressure for both criteria was applied and the result was that in the vertical well drilled in the direction of vertical stress, the stability of the wellbore wall with a safety factor above one were observed; But by drilling horizontal wells in the direction of minimum and maximum horizontal stresses, well wall instability and safety factor below one was observed. Horizontal wellbore instability in the direction of maximum horizontal stress. The instability of the horizontal well in the direction of horizontal stress is minimal, which is due to the vertical stress in the direction perpendicular to the wall.

Finally, the results of the two failure criteria in the vertical and horizontal positions are given in Tables 5 and 6. In Table 5, the safety factor for the internal wall pressure is 200 psi more than the pore space, in which the vertical wellbore wall pressure is stable for both criteria, but in the horizontal wellbore, the wellbore wall is unstable. The internal wellbore pressure is 200 psi more than the pore pressure, in which the vertical wellbore wall is stable for both criteria, but in the horizontal wellbore, the wellbore wall is unstable. Table 6 shows the drilling mud pressure safety factor for both rock failure criteria for vertical and horizontal wellbores. The Mohr-Coulomb failure criterion for vertical and horizontal conditions shows that this range is more than Hoek-Brown.

Table 6 shows the drilling mud pressure safety window range for both failure criteria for vertical and horizontal wells. The Mohr-Coulomb failure criterion for vertical and horizontal conditions shows that this range is more than Hoek-Brown.

By studying Tables 5 and 6, it is clear that the stability of the wellbore in the vertical position is better than in the horizontal position and vertical drilling will have a higher safety factor. In this study, due to the limitations of Examine 2D software, the stability analysis of sloping wells was not prepared and only analyses are made in both vertical and horizontal directions. The results from the analytical method showed the failure criterion indicated that the obtained results are reliable.

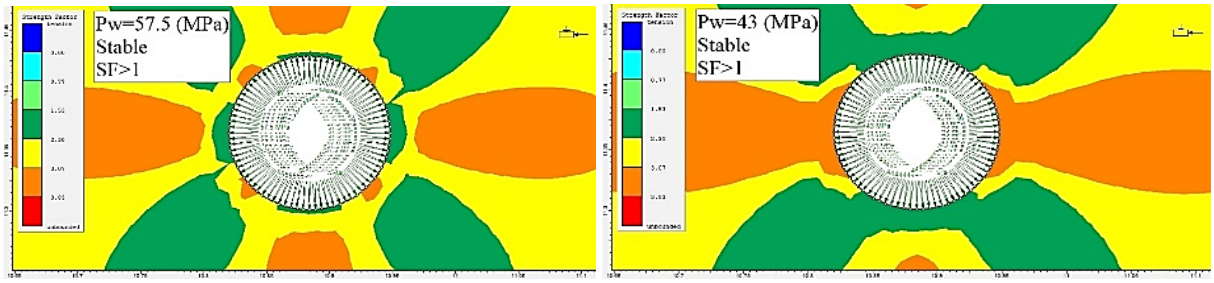

Figure 12. Changes in the safety factor of drilling fluid by applying different internal pressures to the horizontal wellbore wall (Mohr-Coulomb).

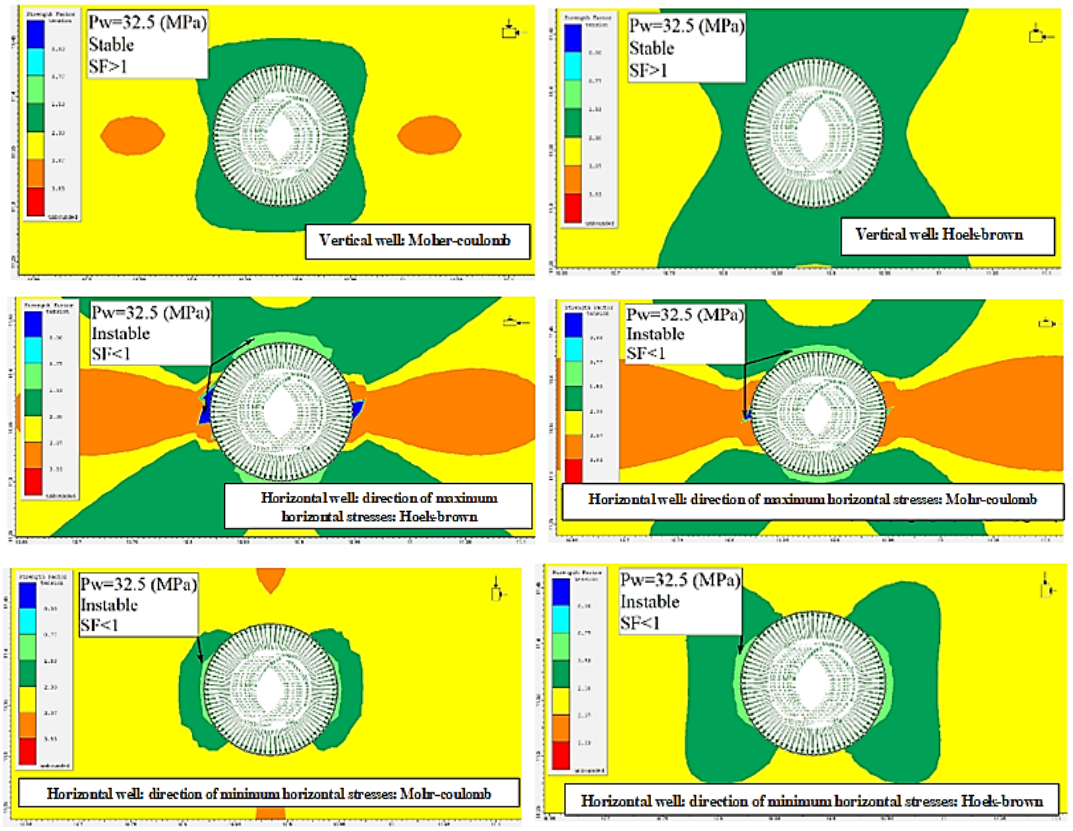

Figure 13. Safety factor changes in horizontal and vertical wells at an internal pressure of 32.5 MPa.

Table 5. Comparison of the safety factor of two failure criteria in vertical and horizontal wells at an internal pressure of 32.5 MPa.

Rock failure criteria	Mud pressure wellbore (MPa)	Safety factors for a vertical well	Safety factors for horizontal well
Hoek-Brown	32.5	SF > 1	SF < 1
Mohr-Coulomb	32.5	SF > 1	SF < 1

Table 6. Comparison of drilling mud pressure safety window with two failure criteria in vertical and horizontal wells.

Rock failure criteria	Drilling mud pressure safety window in vertical well (MPa)	Drilling mud pressure safety window in horizontal well (MPa)
Hoek-Brown	31-56	46-50
Mohr-Coulomb	25-61	43-57.5

6. Conclusions

We compared three criteria. Based on the presented graphs, the Mogi-Coulomb criterion provides a better result than other criteria, which can be due to the application of the main intermediate stress σ2. The Mohr-Coulomb criterion predicts, concerning the tensile strength, a smaller minimum pressure for the mud when increasing the angle deviation of the well. According to the presented diagrams, the effect of the azimuth of the well on the lower angles is significant, but with increasing the angle of the deviation, its effect is reduced. The angle of deviation plays the most significant role in the stability of the wellbore. The lower boundary of the safety of the mud is greater than the permeate pressure and the upper boundary exceeds the horizontal maximum tensile, however, these change with the angle and azimuth. The mud weight caused a higher pressure than the pore pressure and prevented the blowout of the well, but the weak formation causes tensile fractures in the wellbore wall and the loss of fluidity. To understand why the drilling direction is so important it should note that at the depth of interest there is a significant difference between the maximum and minimum horizontal principal stresses. Thus, the instability of the wellbore wall is due to the increase in the difference in wellbore stresses. To prevent this issue, increasing the hydrostatic pressure of the drilling fluid increases the radial stress and decreases the tangential stress, and this reduces

the difference between the tangential and radial stresses of the wellbore and makes the wellbore more stable. By drilling a wellbore, the stress regime is perturbed around the wellbore wall, and the highest concentration of stress and displacement will occur. To control such occurrences the bottom hole pressure should be optimized and so designed to prevent the instability resulting from stress concentration and wellbore displacement and sand production.

Author Contributions

Faramarz Abazari: Wrote the paper; Hossein Jalilifar: Contributed data and analysis tools; Mohammad Ali Riahi: Conceived and designed the analysis.

Funding

This research did not receive any specific grant from funding agencies in the public, commercial, or not-for-profit sectors.

Acknowledgement

This research did not receive any specific grant from funding agencies in the public, commercial, or not-for-profit sectors.

The third author would like to acknowledge the Research Council of the University of Tehran. Thanks are given to anonymous referees for their constructive and insightful comments that led to the improvement of this research.

Data Availability Statement

Restrictions apply to the availability of these data. Data were obtained from the National Iranian Oil Company and are available [from the authors at faramarz880761001@yahoo.com] with the permission of the National Iranian Oil Company.

Conflict of Interest

Author declares that there is no conflict of interest.

References

[1] Lacasse, S., Nadim, F., Liu, Z.Q., et al., 2019. Risk assessment and dams. Recent developments and applications. Proceedings of the XVII European Conference on Soil Mechanics and Geotechnical Engineering, Icelandic Geotechnical Society, Reykjavik.

[2] Carranza-Torres, C., Hormazábal, E., 2020. Computational tools for the estimation of Factor of Safety and location of the critical failure surface for slopes in rock masses that satisfy the Hoek-Brown failure criterion. Slope Stability 2020: Proceedings of the 2020 International Symposium on Slope Stability in Open Pit Mining and Civil Engineering, Australian Centre for Geomechanics, Perth. p. 1099-1122. DOI: https://doi.org/10.36487/ACG_repo/2025_73

[3] Zhang, L., Cao, P., Rodhe, K.C., 2009. Evaluation of rock strength criteria for wellbore stability analysis. International Journal of Rock Mechanics & Mining Sciences. 47(8), 1304-1316.

[4] Al-Ajmi, A.M., Zimmerman, R.W., 2006. Structural borehole stability analysis using the Mogi-Coulomb failure criterion. International Journal of Rock Mechanics and Mining Sciences.

[5] Carter, T., Carranza-Torres, C., 2019. Global characterization of high rock slopes using the Hoek-Brown mb parameter as controlling index. Proceedings of the 14th International Congress on Rock Mechanics and Rock Engineering, Foz do Iguassu.

[6] McLean, M., Addis, M., 1990. Wellbore stability: The effect of strength criteria on mud weight recommendations. SPE Annual Technical Conference and Exhibition. OnePetro. p. 23-26.

[7] Al-Ajmi, A.M., Zimmerman, R.W., 2009. A new well path optimization model for increased mechanical borehole stability. Journal of Petroleum Science and Engineering. 69, 53-62.

[8] Chatterjee, R., Mukhopadhyay, M., 2003. Numerical modelling of stress around a wellbore. Asia Pacific Oil and Gas Conference and Exhibition. OnePetro. DOI: https://doi.org/10.2118/80489-MS

[9] Hoang, S., Abousleiman, Y., Tare, U., 2004. The analytical solution for wellbore stability in multilateral junctions in the non-hydrostatic in-situ stress field. SPE Annual Technical Conference and Exhibition. OnePetro. p. 1-9.

[10] Salehi, S., Hareland, G., Nygaard, R., 2010. Numerical simulation of wellbore stability in under-balanced drilling wells. Journal of Petroleum Science and Engineering. 72, 229-235.

[11] Aslannejad, M., Manshad, A.K., Jalilifar, H., 2013. Analysis of vertical, Horizontal, and deviated wellbores stability. American Journal of Oil and Chemical Technologies. 1(8), 10-19.

[12] Kouchaki, E., Goshtasbi, K., Sharifzadeh, M., 2007. Stability analysis of oil wells in Asmari Formation, Kupal reservoir. Second Iranian Petroleum Engineering Congress. pp. 427-434. (in Persian) Available from: https://civilica.com/doc/146959/

[13] Horsrud, P., 2001, Estimating mechanical properties of shale from empirical correlations. SPE 56017 Drilling and Completion. 16, 68-73.

[14] Fjaer, E., Holt, R., Horsrud, P., et al., 2008. Petroleum related rock mechanics. 2nd Edition. Elsevier: Amsterdam.

[15] Hoek, E., Brown, E.T., 2019. The Hoek-Brown failure criterion and GSI, 2018 edition. Journal of Rock Mechanics and Geotechnical Engineering. 11, 445-463.

Earth and Planetary Science
https://ojs.nassg.org/index.php/eps/index

REVIEW ARTICLE

Contribution to the Paleontology, Stratigraphy and Paleogeography of Ninety-seven Southern Tethyan Agglutinated Foraminiferal Species

Haidar Salim Anan*

Professor of Stratigraphy and Micropaleontology, Al Azhar University-Gaza, Palestine

ARTICLE INFO

Article history
Received: 29 March 2022
Revised: 14 May 2022
Accepted: 24 May 2022
Published Online: 2 June 2022

Keywords:
Agglutinated foraminifera
Campanian
Paleogene
Southern and Northern Tethys

ABSTRACT

Ninety-seven Campanian-Paleogene smaller agglutinated benthic foraminiferal species belonging to thirty-five genera from ten countries in the Southern Tethys (Algeria, Egypt, Palestine, Jordan, Iraq, Qatar, UAE, Iran, Pakistan, India) have been studied. The modern taxonomical consideration of the species is used. Eighty-nine of the recorded species were previously noted in the literature, while eight of them are believed here as new: *Haplophragmoides iranica, Pseudogaudryinella iraqensis, Arenobulimina beitjebrinensis, A. jerusalemensis, Textulariella sinaensis, Dorothia iranica, Clavulinoides iranica,* and *Textularia salahii.* Forty species of them are recorded from Egypt (about 41%), twenty-seven from Pakistan (~ 28%), ten from UAE (~ 10.5%), six from Qatar (~ 6%), four from each of Algeria and Iran (~ 4%), three from Jordan (~ 3%), two from each of Palestine and Iran (~ 2%), and only one from each of Iraq and India (~ 1%). Most of the Southern Tethyan recorded species are endemic to their original description, while five of them are also recorded in some Northern Tethyan countries (Spain, France, Italy, Hungary and Slovenia): *Bathysiphon saidi, Haplophragmoides desertorum, Spiroplectinella esnaensis, Siphogaudryina africana* and *Textularia crookshanki.* The Southern Tethyan assemblage indicates an open marine environment, which represents middle-outer neritic environment (100-200 m depth), and shows an affinity with Midway-Type Fauna (MTF) of the United States Gulf Coastal area.

1. Introduction

An attempt has been made to bring together many scattered data in the literature under a unifying theme for the holotypes and paratypes of ninety-seven agglutinated foraminiferal species of the Order Astrorhizida Lankester in ten countries in the Southern Tethys (Algeria, Egypt, Palestine, Jordan, Iraq, Qatar, UAE, Iran, Pakistan, India, Figures 1-2). All the recorded species were erected from the Campanian-Early Paleogene time, and one from Recent. Some species of them are also recorded in other countries in both the Southern Tethys (i.e. Tunisia, Libya)

*Corresponding Author:
Haidar Salim Anan,
Professor of Stratigraphy and Micropaleontology, Al Azhar University-Gaza, Palestine;
Email: profanan@gmail.com

DOI: http://dx.doi.org/10.36956/eps.v1i1.511

Copyright © 2022 by the author(s). Published by Nan Yang Academy of Sciences Pte. Ltd. This is an open access article under the Creative Commons Attribution-NonCommercial 4.0 International (CC BY-NC 4.0) License. (https://creativecommons.org/licenses/by-nc/4.0/).

and Northern Tethys (i.e. Spain, France, Italy, Hungary, Slovenia). Eight species of them are believed here as new: *Haplophragmoides iranica, Pseudogaudryinella iraqensis, Arenobulimina beitjebrinensis, A. jerusalemensis, Textulariella sinaensis, Dorothia iranica, Clavulinoides iranica* and *Textularia salahii.*

2. Previous Studies

Many studies have been made to erect, illustrate and describe the ninety-seven agglutinated benthic foraminiferal species belonging to thirty-five genera are recorded in this study, which related to ten countries in the Southern Tethys, which done by many authors from these countries. Four species of them from Algeria by Ten Dam & Sigal [1], forty species from Egypt by many authors: Omara [2], Nakkady [3,4], LeRoy [5], Said & Kenawy [6], Anan [7-13], El-Dawy [14], Ali [15], two species from Palestine by Anan (this study), three species from Jordan by Futyan [16], one species from Iraq by Anan (this study), six species from Qatar by Hewaidy & Al-Hitmi [17,18], ten species from UAE by Anan [19-21,13], four species from Iran by Anan (this study), twenty-seven from Pakistan by Haque [22-24], and Anan [13], and one species from India by Habibnia & Mannikeri [25].

3. Systematic Paleontology

The taxonomy of Kaminski [26] (2014) is followed in this study for ninety-seven agglutinated foraminiferal benthic specie were erected from ten countries in the Southern Tethys. The new taxonomic considerations are used for many recorded species. These species are illustrated in Plates 1 and 2.

Order Astrorhizida Lankester, 1885;
Suborder Astrorhizina Lankester, 1885;
Superfamily Astrorhizoidea Brady, 1881;
Family Rhabdamminidae Brady, 1884;
Genus *Bathysiphon* Sars, 1872;

1) ***Bathysiphon paleocenica*** **El-Dawy** [14], p. 42, pl. 1, Figure 1 - (Pl. 1, Figure 1).

2) ***Bathysiphon saidi*** **(Anan)** [8] - Anan [27], p. 19, pl. 1, Figure 2. (= *Rhabdammina saidi* Anan [8], p. 218, Figure 8.1) - (Pl. 1, Figure 2).

Suborder Hemisphaeramminiae Loeblich & Tappan, 1961;
Family Saccamminidae Brady, 1884;
Genus *Orbulinoides* Saidova, 1975;

3) ***Orbulinoides arabica*** **Anan** [10], p. 531, Figure 4.1 - (Pl. 1, Figure 3).

Suborder Ammodiscina Mikhalevich, 1980;
Superfamily Ammodiscoidea Reuss, 1862;
Family Ammodiscidae Reuss, 1862;
Genus *Ammovertella* Cushman, 1928;
Type species *Ammodiscus (Psammophis) invertus* Schellwien, 1898;

4) ***Ammovertella qatarica*** **Hewaidy & Al-Hitmi** [18], p. 12, Figure 5.1, 5.2 - (Pl. 1, Figure 4).

Genus *Repmanina* Suleymanov, 1966;

5) ***Repmanina mazeni*** **Anan** [20], p. 85, pl. 1, Figure 4. (= *Repmanina* sp. Anan [28], p. 244, Figure 4.7) - (Pl. 1, Figure 5).

Order Schlumbergerinida Mikhalevich, 1980;
Suborder Schlumbergerinina Mikhalevich, 1980;
Superfamily Rzehakinoidea Cushman, 1933;
Family Rzehakinidae Cushman, 1933;
Genus *Rzehakina* Cushman, 1928;

6) ***Rzehakina khatiyahi*** **Hewaidy & Al-Hitmi** [18], p. 13, Figure, 5.3, 5.4 - (Pl. 1, Figure 6).

Family Miliamminidae Saidova, 1981;
Genus *Miliammina* Heron-Allen & Earland, 1930;

7) ***Miliammina kenawyi*** **Anan** [8], p. 218, Figure 8.2 - (Pl. 1, Figure 7).

Genus *Agglutinella* El-Nakhal, 1983;

8) ***Agglutinella reinemundi*** **(Haque** [23]**,** 1960) - Anan [20], p. 55, pl. 1, Figure 10 (= *Triloculina reinemundi* Haque [23], p. 19, pl. 2, Figure 5) - (Pl. 1, Figure 8).

9) ***Agglutinella sori*** **(Haque** [23]) - Anan, 2021a [20], p. 55, pl. 1, Figure 11 (*Triloculina sori* Haque [23], p. 20, pl. 5, Figure 9) - (Pl. 1, Figure 9).

Genus *Dentostomina* Cushman, 1933;

10) ***Dentostomina ammobicarinata*** **(Haque** [23]**)** - Anan [20], p. 44, pl. 1, Figure 5 (= *Triloculina ammobicarinata* Haque [23], pl. 6, Figure 6) - (Pl. 1, Figure 10).

11) ***Dentostomina ammoirregularis*** **(Haque** [23]**)** - Anan [20], p. 44, pl. 1, Figure 6 (= *Triloculina ammoirregularis* Haque [23], pl. 6, Figure 4) - (Pl. 1, Figure 11).

12) ***Dentostomina gapperi*** **(Haque** [22]**)** - Anan [20], p. 44, pl. 1, Figure 7 (= *Quinqueloculina gapperi* Haque [22], p. 54, pl. 32, Figure 11) - (Pl. 1, Figure 12).

Family Ammomassilinidae Mikhalevich & Kaminski, 2008;
Genus *Ammomassilina* Cushman, 1933;

13) ***Ammomassilina misrensis*** **Anan** [21] – Anan [21], p. 88, pl. 1, Figure 22 (= *Ammomassilina* sp. Anan [8], p. 219, Figure 8.5) - (Pl. 1, Figure 13).

Order Lituolida Lankester, 1885;
Suborder Lituolina Lankester, 1885;
Superfamily Lituoloidea de Blainville, 1827;
Family Haplophragmoididae Maync, 1952;
Genus *Asanospira* Takayanagi, 1960;

14) ***Asanospira diyabi*** **Hewaidy & Al-Hitmi** [18], p. 13, Figure 5.5, 5.6 - (Pl. 1, Figure 14).

15) ***Asanospira jalehaensis*** **Hewaidy & Al-Hitmi** [18], p. 13, Figure 5.7, 5.8 - (Pl. 1, Figure 15).

Suborder Hormosinina Mikhalevich, 1980;
Superfamily Hormosinoidea Haeckel, 1894;
Family Glaucoamminidae Saidova, 1981;
Genus *Psammolingulina* Silvestri, 1904;

16) ***Psammolingulina bahri*** **Anan** [21] **-** Anan [21], p. 85, pl. 1, Figure 4 (= *Psammolingulina* sp. Anan [28], p. 244, Figure 4.8) - (Pl. 1, Figure 16).

Suborder Lituolina Lankester, 1885;
Superfamily Lituoloidea de Blainville, 1827;
Family Haplophragmoididae Maync, 1952;
Genus *Haplophragmoides* Cushman, 1910;

17) ***Haplophragmoides desertorum*** **LeRoy** [5], p. 36, pl. 1, Figures 21, 22 - (Pl. 1, Figure 17).

18) ***Haplophragmoides iranica*** **Anan, n. sp.** (= *Haplophragmoides* sp., Salahi [29], p. 316, pl. 5, Figure 13).

Holotype: The illustrated specimen in Pl. 1, Figure 18; Pl. 2, Figure 1.

Dimension: Diameter 0.17 mm.

Depository: The geological Museum of Ferdowsi University of Mashhad, Iran.

Etymology: After the Islamic Republic of Iran.

Type locality: Khangiran Formation, Kopet-Dagh Basin, NE Iran.

Age: Middle Eocene.

Diagnosis: This species has closed coiled planispiral test, composed of three coils, the last coil composed of about 10 number of chambers in the last-formed coil, wall arenaceous and fine in texture, sutures distinct and depressed, periphery broadly rounded, aperture at the ventral border or on the lower portion of the apertural face of the chamber.

Remarks: This species differs from *H. desertorum* LeRoy in its three coiled whorls than one, tight than wide umbilicus, and higher diameter test.

Family Lituolidae de Blainville, 1827;
Genus *Ammobaculites* Cushman, 1910;

19) ***Ammobaculites bhallai*** **Habibnia & Mannikeri** [25], p. 3, pl. 1, Figures 2-4 - (Pl. 1, Figure 19).

20) ***Ammobaculites khargaensis*** **Nakkady** [4], p. 456, pl. 6, Figure 1 - (Pl. 1, Figure 20).

21) ***Ammobaculites schwageri*** **Said & Kenawy** [6], p. 121, pl. 1, Figure 8 - (Pl. 1, Figure 21).

Subfamily Flabellammininae Podobina, 1978;
Genus *Triplasia* Reuss, 1854;

22) ***Triplasia palmate*** **Hewaidy & Al-Hitmi** [18], p. 14, Figure 5.9, 5.10 - (Pl. 1, Figure 22).

Suborder Spiroplectamminina Mikhalevich, 1992;
Superfamily Spiroplectamminoidea Cushman, 1927;
Family Spiroplectamminidae Cushman, 1927;
Genus *Spiroplectinella* Kisel'man, 1927;

23) ***Spiroplectinella esnaensis*** **(LeRoy** [5]**)** - Aubert & Berggren [30], p. 409, pl. 1, Figure 6 (= *Spiroplectammina esnaensis* LeRoy [5], p. 50, pl. 1, Figures 11, 12) - (Pl. 1, Figure 23).

24) ***Spiroplectinella hamdani*** **(Anan** [19] **-** Anan [27], p. 79, pl. 1, Figure 2 (= *Spiroplectammina hamdani* Anan [7], p. 652, pl. 1, Figure 14) - (Pl. 1, Figure 24).

25) ***Spiroplectinella henryi*** **(LeRoy** [5]**)** - Hewaidy et al. [31], p. 20, pl. 3, Figure 20 (= *Spiroplectammina henryi* LeRoy [5], p. 50, pl. 2, Figure 15) - (Pl. 1, Figure 25).

26) ***Spiroplectinella knebeli*** **(LeRoy** [5]**) -** Anan [27], p. 80 (= *Spiroplectammina knebeli* LeRoy [5], p. 51, pl. 2, Figures 10, 11) - (Pl. 1, Figure 26).

27) ***Spiroplectinella paracarinata*** **Said & Kenawy** [6] - Anan [12], p. 20, pl. 1, Figure 1 (= *Spiroplectammina paracarinata* Said & Kenawy [6], p. 122, pl. 1, Figure 13). (Pl. 1, Figure 27).

28) ***Spiroplectinella ushbali*** (**Haque** [23]) - Anan [13], p. 10, pl. 1, Figure 1 (= *Textularia ushbali* Haque [23], p. 18, pl. 3, Figure 7) - (Pl. 1, Figure 28).

Suborder Trochamminina Saidova, 1981;
Superfamily Trochamminoidea Schwager, 1877;
Family Trochamminidae Schwager, 1877;
Genus *Trochammina* Parker & Jones, 1859;

29) ***Trochammina dohaensis*** **Hewaidy & Al-Hitmi** [18], p. 14, Figure 5.11, 5.12 - (Pl. 1, Figure 29).

Suborder Verneuilinina Mikhalevich & Kaminski, 2004;
Superfamily Vernuilinoidea Cushman, 1911;
Family Prolixopplectidae Loeblich &Tappan, 1985;
Genus *Plectina* Marsson, 1878;

30) ***Plectina emiratensis*** **Anan** [10], p. 534, Figure 4.2 - (Pl. 1, Figure 30).

Family Tritaxiidae Plotnikova, 1979;
Genus *Tritaxia* Reuss, 1860;

31) ***Tritaxia barakai*** **Said & Kenawy** [6], p. 123, pl. 1, Figure 18 - (Pl. 1, Figure 31).

32) ***Tritaxia elongata*** **(Haque** [22]**) –** Anan [32], p. 31, pl. 1, Figure 1 (= *Clavulinoides lakiensis elongata* Haque [22], p. 45, pl. 21, Figure 13) - (Pl. 1, Figure 32).

33) ***Tritaxia limbata*** **(Haque** [22]**) –** Anan [32], p. 31, pl. 1, Figure 2 (= *Clavulinoides lakiensis limbata* Haque [22], p. 45, pl. 21, Figure 8) - (Pl. 1, Figure 33).

Family Reophacellidae Mikhalevich & Kaminski, 2004;

Genus *Gaudryina* d'Orbigny, 1839;

34) ***Gaudryina aissana*** **Ten Dam & Sigal** [1], p. 31, pl. 2, Figure 2 - (Pl. 1, Figure 34).

35) ***Gaudryina ameeri*** **Anan** [12], p. 63, pl. 1, Figure 7 - (Pl. 1, Figure 35).

36) ***Gaudryina arabica*** **Anan** [13], p. 28, pl. 1, Figure 11 - (Pl. 1, Figure 36).

37) ***Gaudryina ennakhali*** **Anan** [13], p. 28, pl. 1, Figure 10 - (Pl. 1, Figure 37).

38) ***Gaudryina limbata*** **Said & Kenawy** [6], p. 123, pl. 1, Figure 23 - (Pl. 1, Figure 38).

39) ***Gaudryina nitida*** **Haque** [22] - Anan [13], p. 10, pl. 1, Figure 2 (= *Gaudryina pyramidata* Cushman *nitida* Haque [22], p. 41, pl. 9, Figure 2) - (Pl. 1, Figure 39).

40) ***Gaudryina osmani*** **Anan** [13], p. 28, pl. 1, Figure 14 - (Pl. 1, Figure 40).

41) ***Gaudryina rectiangulata*** **Ten Dam & Sigal** [1], p. 31, pl. 2, Figure 3 - (Pl. 1, Figure 41).

42) ***Gaudryina speijeri*** **Anan** [12], p. 66, pl. 1, Figure 10 - (Pl. 1, Figure 42).

43) ***Gaudryina salimi*** **Anan** [13], p. 28, pl. 1, Figure 12 - (Pl. 1, Figure 43).

44) ***Gaudryina textulariformis*** **Nakkady** [4], p. 457, pl. 6, Figure 3 - (Pl. 1, Figure 44).

Genus *Pseudogaudryinella* Cushman, 1936;

45) ***Pseudogaudryinella iraqensis*** **Anan, n. sp.** (= *Tritaxia whitei* of Jaff & Lawa [33], p. 14, pl. 2, Figures 14, 15).

Holotype: Illustrated specimen in Pl. 1, Figure 45; Pl. 2, Figure 2.

Dimension: Length 0.45 mm, width 0.17 mm.

Depositary: Department of Geology, University of Sulaimani, Iraq.

Etymology: After the Iraq Republic.

Type locality: Shiranish Formation, Kurdistan region, Northeast Iraq.

Age: Campanian.

Diagnosis: Test elongate, early stage triserial triangular in section, followed by biserial, and finally uniserial rounded in section, aperture terminal in the last chamber and rounded.

Remarks: This species belongs to the genus *Pseudogaudryinella* and differs from the genus *Tritaxia* in having a biserial stage intercalated between the triserial and uniserial ones, and differs from the genus *Gaudryina* in becoming uniserial in adult.

Genus *Siphogaudryina* Cushman, 1935;

46) ***Siphogaudryina africana*** **(LeRoy** [5]**) -** Anan [11], p. 272, pl. 1, Figure 7 (= *Gaudryina africana* LeRoy [5], p. 30, pl. 1, Figures 7, 8) - (Pl. 1, Figure 46).

47) ***Siphogaudryina daviesi*** **(Haque** [22]**) -** Anan [32], p. 31, pl. 1, Figure 3 (= *Gaudryina daviesi* Haque [22], p. 37, pl. 31, Figure 14) - (Pl. 1, Figure 47).

48) ***Siphogaudryina elongata*** **(Haque** [22]**) –** Anan [34], p. 272, pl. 1, Figure 9 (= *Gaudryina laevigata* Franke *elongata* Haque [22], p. 35, pl. 9, Figure 5) - (Pl. 1, Figure 48).

49) ***Siphogaudryina elegantissima*** **(Said & Kenawy** [6]**) -** Anan [24], p. 3, pl. 1, Figure 3 (= *Gaudryina elegantissima* Said & Kenawy [6], p. 123, pl. 1, Figure 21) - (Pl. 1, Figure 49).

50) ***Siphogaudryina nammalensis*** **(Haque** [22]**) -** Anan [34], p. 273, pl. 1, Figure 11 (= *Gaudryina* (*Siphogaudryina*) *carinata* Franke *nammalensis* Haque [22], p. 40, pl. 3, Figure 2) - (Pl. 1, Figure 50).

51) ***Siphogaudryina nekhlensis*** **(Said & Kenawy** [6]**) -** Anan [12], p. 20, pl. 1, Figure 4 (= *Gaudryina nekhlensis* Said & Kenawy [6], p. 124, pl. 1, Figure 24) - (Pl. 1, Figure 51).

52) ***Siphogaudryina strougoi*** **Anan** [9]**,** p. 141, Figure 2.1 - (Pl. 1, Figure 52).

53) ***Siphogaudryina tellburmaensis*** **(Futyan** [16]**) -** Anan [35], p. 3, pl. 1, Figure 3 (= *Gaudryina tellburmaensis* Futyan [16], p. 521, pl. 81, Figures 1, 2) - (Pl. 1, Figure 53).

Genus *Verneuilina* d'Orbigny, 1839;

54) ***Verneuilina aegyptiaca*** **Said & Kenawy** [6], p. 122, pl. 1, Figure 16 - (Pl. 1, Figure 54).

55) ***Verneuilina laevigata*** **Haque** [22], p. 34, pl. 21, Figures 9, 12 - (Pl. 1, Figure 55).

56) ***Verneuilina luxorensis*** **Nakkady** [3]**,** p. 683, pl. 89, Figure 6.7 - (Pl. 1, Figure 56).

Order Loftusiida Kaminski & Mikhalevich, 2004;

Suborder Ataxophragmiina Fursenko, 1958;

Superfamily Ataxophragmiacea Schwager, 1877;

Family Ataxophragmiidae Schwager, 1877;

Genus *Arenobulimina* Cushman, 1927;

57) ***Arenobulimina aegyptiaca*** **Said & Kenawy** [6], p. 126, pl. 1, Figure 42 - (Pl. 1, Figure 57).

58) ***Arenobulimina beitjebrinensis*** **Anan, n. sp.** (=

Arenobulimina sp. A. Almogi-Labin et al. [36], p. 578, pl. 2, Figure 5).

Holotype: Illustrated specimen in Pl. 1, Figure 58; Pl. 2, Figure 3.

Diameter: Length 0.25 mm, width 0.20 mm.

Etymology: After the type locality.

Type locality: Beit Jebrin, Palestine (Figure 3).

Stratigraphic level and age: *Gansserina gansseri* Zone, Late Maastrichtian.

Diagnosis: Test arenaceous, conical, trochospirally enrolled, tapering initial part with four-five chambers, later four chambers in the last whorl, chambers inflated, sutures distinct depressed, aperture an interiomarginal loop.

Remarks: This species differs from usually four making up at last whorl, tapering initial part, distinct loop-shaped aperture, older stratigraphic level. It is recorded, so far, from Palestine.

59) ***Arenobulimina jerusalemensis*** **Anan, n. sp. (**= *Arenobulimina* sp. B. Almogi-Labin et al. [36], p. 578, pl. 2, Figure 4).

Holotype: Illustrated specimen in Pl. 1, Figure 59; Pl. 2, Figure 4.

Diameter: Length 0.50 mm, width 0.50 mm.

Etymology: After the type locality, Palestine.

Type locality: southwest Jerusalem.

Stratigraphic level and age: *Gansserina gansseri - Abathomphalus mayaroensis* Zones, Late Maastrichtian .

Diagnosis: Low trochospiral test, four chambers in the last whorl, distinct inflated chambers, sutures depressed, aperture an interiomarginal loop.

Remarks: It differs from *A. beitjebrinensis* in its shorter length test, and younger stratigraphic level.

Family Textulariellidae Grönhagen & Luterbacher, 1966;

Genus *Textulariella* Cushman, 1927;

60) ***Textulariella sinaensis*** **Anan, n. sp.** (= *Textulariella* sp. Said & Kenawy [6], p. 127, pl. 1, Figure 43.

Holotype: Illustrated specimen in Pl. 1, Figure 60; Pl. 2, Figure 5.

Diameter: Length 0.4 mm, breadth 0.4 mm.

Depository: USNM P. 3988.

Etymology: After the Sinai Peninsula, Egypt.

Type locality: Giddi section, northern Saini, Egypt (Figure 3).

Stratigraphic level and age: Danian.

Diagnosis: Test very fine arenaceous and smoothly finished, more or less cylindrical in shape, initial part trochospiral coil, but biserial in the later part and increasing rapidly as added, sutures slightly limbate, aperture a low opening at the middle of the final chamber.

Remarks: This Danian species has cylindrical test, which differs from the conical and tapering sharply early stage of the Maastrichtian-Danian *T. cretosa*.

Order Textulariida Delage & Hérouard, 1896, emended by Kaminski, 2004;

Suborder Textulariina Delage & Hérouard, 1896;

Superfamily Eggerelloidea Cushman, 1937;

Family Eggerellidae Cushman, 1937;

Genus *Dorothia* Plummer, 1931;

61) ***Dorothia iranica*** **Anan, n. sp. (=** *Tritaxilina* sp., Salahi [29], p. 316, pl. 5, Figure 7**).**

Holotype: The figured specimen in Pl. 1, Figure 61; Pl. 2, Figure 6.

Dimension: Length 0.8 mm, width 0.3 mm.

Depositary: The geological Museum of Ferdowsi University of Mashhad, Iran.

Etymology: After the Islamic Republic of Iran.

Type locality: Khangiran Formation, Kopet-Dagh Basin, NE Iran.

Age: Early Eocene.

Diagnosis: The genus *Tritaxilina* has fusiform test, early portion triserial, roughly triangular in transverse section, the angles much rounded; later portion biserial or finally uniserial, circular in section, apical end somewhat pointed, apertural end truncate or broadly rounded; chambers numerous; the wall thick, of fine arenaceous material; sutures distinct, depressed; aperture in the young as in *Verneuilina*, in the adult becoming terminal and central with a border of inwardly projecting teeth. The genus *Dorothia* has triserial early portion followed by biserial chambers, without uniserial end portion.

Remarks: This species differs from *Dorothia bulletta* (Carsey) by its more elongated test, more depressed sutures and more large numbers of the inflated biserial chambers.

62) ***Dorothia nammalensis*** **Haque [22], 1956 –** Anan [13], p. 11, pl. 1, Figure 9 (= *Dorothia pupoides* (d'Orbigny) *nammalensis* Haque [22], p. 53, pl. 32, Figure 4) - (Pl. 1, Figure 62).

63) ***Dorothia sinaensis*** **Said & Kenawy** [6], p. 128, pl. 2, Figure 1 - (Pl. 2, Figure 63).

Genus *Marssonella* Cushman, 1933;

64) ***Marssonella hafitensis*** **Anan** [10]**,** p. 535, Figure 4.3 - (Pl. 1, Figure 64).

65) ***Marssonella nammalensis*** **Haque** [22] - Anan [13], p. 11, pl. 1, Figure 10 (= *Marssonella oxycona* (Reuss) *nammalensis* Haque [22], p. 50, pl. 3, Figure 4) - (Pl. 1, Figure 65).

Genus *Eggerella* Cushman, 1935;

66) ***Eggerella maqfiensis*** **LeRoy** [5]**,** p. 28, pl. 1, Figures 1, 2 - (Pl. 1, Figure 66).

Genus *Clavulinoides* Cushman, 1937;

67) ***Clavulinoides algerianus*** **Ten Dam & Sigal** [1], p. 33, pl. 2, Figure 11- (Pl. 1, Figure 67).

68) ***Clavulinoides iranica*** **Anan, n. sp. (=** *Heterostomella austinana* of Salah [29], p. 314, pl. 4, Figure 25).

Holotype: The illustrated specimen in Pl. 1 Figure 68; Pl. 2, Figure 7.

Dimension: Length 1.10 mm, width 0.45 mm.

Depository: The geological Museum of Ferdowsi University 0f Mashhad, Iran.

Etymology: After the Islamic Republic of Iran.

Type locality: Khangiran Formation, Kopet-Dagh Basin, NE Iran.

Age: Middle Eocene.

Diagnosis: The genus *Clavulinoides* has triserially early chambers arranged and later abruptly becoming uniserial, while the genus *Heterostomella* has triserial early stage followed by biserial chamber arranged. The species *C. iranica* has curved triangle test in cross section and discoidal last chamber.

Remarks: This species is characterized by its curved test than other most species of the genus which have nearly rectilinear tests.

69) ***Clavulinoides lakiensis*** **Haque** [22]**,** p. 43, pl. 21, Figure 7; p. 54, pl. 32, Figure 1 - (Pl. 1, Figure 69).

70) ***Clavulinoides spatha*** **Haque** [22] – Anan [13], p. 12, pl. 1, Figure 18 (= *Clavulinoides lakiensis spatha* Haque [22], p. 44, pl. 21, Figure 6) - (Pl. 2, Figure 70).

Genus *Pseudoclavulina* Cushman, 1937;

71) ***Pseudoclavulina barnardi*** **(Futyan** [16]**) -** Anan [13], p. 3, pl. 1, Figure 7 (= *Clavulina barnardi* Futyan [16], p. 522, pl. 81, Figure 3 (*non* Figure 4) - (Pl. 1, Figure 71).

72) ***Pseudoclavulina farafraensis*** **LeRoy** [5]**,** p. 44, pl. 2, Figure 9 - (Pl. 1, Figure 72).

73) ***Pseudoclavulina futyani*** **Anan** [11]**,** p. 87, pl. 1, Figure 16 (= *Clavulina barnardi* Futyan [16], p. 522, pl. 81, Figure 4 (*non* Figure 3) - (Pl. 1, Figure 73).

74) ***Pseudoclavulina globulifera*** **Ten Dam & Sigal** [1]**,** p. 32, pl. 2, Figures 5-7 - (Pl. 1, Figure 74).

75) ***Pseudoclavulina hewaidyi*** **Anan** [11]**,** p. 248, pl. 1, Figure 1 - (Pl. 1, Figure 75).

76) ***Pseudoclavulina maqfiensis*** **LeRoy** [5]**,** p. 44, pl. 2, Figures 16, 17 - (Pl. 1, Figure 76).

77) ***Pseudoclavulina pseudoarenata*** **Said & Kenawy** [6]**,** p. 125, pl. 1, Figure 33 - (Pl. 1, Figure 77).

78) ***Pseudoclavulina youssefi*** **Anan** [20]**,** p. 88, pl. 1, Figure 18 (= *Tritaxia* sp. Ali [15], pl. 3, Figure 14) - (Pl. 1, Figure 78).

Genus *Valvoreussella* Hofker, 1957;

79) ***Valvoreussella karreri*** **(Said & Kenawy** [6]**)** - Hewaidy & Al-Hitmi [17], p. 481, pl. 6, Figures 7, 8 (= *Verneuilina karreri* Said & Kenawy [6], p. 122, pl. 1, Figure 17) - (Pl. 1, Figure 79).

Family Valvulinidae Berthelin, 1880;

Genus *Clavulina* d'Orbigny, 1826;

80) ***Clavulina paxilliformis*** **Haque** [22]**,** p. 49, pl. 12, Figures 6, 8 - (Pl. 1 Figure 80).

81) ***Clavulina pseudoparisensis*** **Anan** [7]**,** p. 239, pl. 1, Figures 6, 7 - (Pl. 1, Figure 81).

82) ***Clavulina symmetrica*** **Haque** [22] **-** Anan [13], p. 12, pl. 1, Figure 19 (= *Clavulina paxilliformis symmetrica* Haque [22], p. 50, pl. 24, Figure 6) - (Pl. 1, Figure 82).

Genus *Valvulina* d'Orbigny, 1826;

83) ***Valvulina elongata*** **Haque** [22]**,** p. 47, pl. 21, Figure 11 (= *Valvulina nammalensis* Haque [22], (*non* 10) - (Pl. 1, Figure 83).

84) ***Valvulina nammalensis*** **Haque** [22]**,** p. 47, pl. 21, Figure 10 (*non* Figure 11) - (Pl. 1, Figure 84).

Superfamily Textulariodea Ehrenberg, 1838;

Family Thomasinellidae Loeblich & Tappan, 1984;

Genus *Thomasinella* Sclumberger, 1893;

85) ***Thomasinella aegyptia*** **Omara** [2]**,** p. 885, pl. 101, Figure 1 - (Pl. 1, Figure 85).

86) ***Thomasinella fragmentaria*** **Omara** [2]**,** p. 884, text-Figure 1.6 - (Pl. 1, Figure 86).

Family Textulariidae Ehrenberg, 1838;

Genus *Bigenerina* d'Orbigny, 1826;

87) ***Bigenerina khirthari*** **Haque** [23]**,** p. 18, pl. 3, Figure 4 - (Pl. 1, Figure 87).

88) ***Bigenerina metingensis*** **Haque** [24]**,** p. 18, pl. 2, Figures 13, 14 - (Pl. 2, Figure 88).

89) ***Bigenerina nodosa*** **Haque** [22]**,** p. 33, pl. 3, Figures 7, 8 - (Pl. 2, Figure 89).

Genus *Textularia* Defrance, 1824;

90) ***Textularia crookshanki*** **Haque** [22]**,** p. 32, pl. 9, Figure 9 - (Pl. 2, Figure 90).

91) ***Textularia fahmyi*** **Anan** [8]**,** p. 218, Figure 8.3 - (Pl. 2, Figure 91).

92) ***Textularia farafraensis*** **LeRoy** [5]**,** p. 51, pl. 2, Figures 3, 4 - (Pl. 2, Figure 92).

93) ***Textularia haquei*** **Anan** [35]**,** p. 3, pl. 1, Figure 6 (= *Textularia* sp. Haque [22], p. 32, pl. 9, Figures 10, 11) - (Pl. 2, Figure 93).

94) ***Textularia nilotica*** **(Schwager** [37]**)** - LeRoy [5], p. 52, pl. 2, Figures 1, 2 (= *Plecanium niloticum* Schwager [37], p. 115, pl. 26, Figure 14) - (Pl. 2, Figure 94).

95) ***Textularia punjabensis*** **Haque** [22]**,** p. 31, pl. 9, Figure 12 - (Pl. 2, Figure 95).

96) ***Textularia salahii* Anan, n. sp.** Pl. 2, Figure 34 (= *Textularia* sp. Salahi [29], p. 316, pl. 5, Figures 9, 10).

Holotype: The illustrated specimen in Pl. 1, Figure 96; Pl. 2, Figure 8.

Dimension: Length and width of the top specimen: 0.30 mm.

Type locality: Kopet-Dagh Basin, NE Iran.

Age: Middle Eocene.

Etymology: After prof. Amir Salahi, Ferdowsi University of Mashhad, Iran.

Diagnosis: Test medium, length equal the top part of the last biserial inflated chambers, expanding uniformly, periphery broadly round, sutures depressed and nearly straight, wall moderately smooth.

Remarks: This species differs from the other species of *Textularia* by its smaller size, not elongated test, three additional biserial chambers.

97) ***Textularia schwageri* LeRoy** [5], p. 51, pl. 2, Figures 5, 6 - (Pl. 1, Figure 97).

Figure 1. The geographic distribution of the recorded benthic foraminiferal species in the ten countries in the Southern Tethys (Algeria, Egypt, Palestine, Jordan, Iraq, Qatar, UAE, Iran, Pakistan and India).

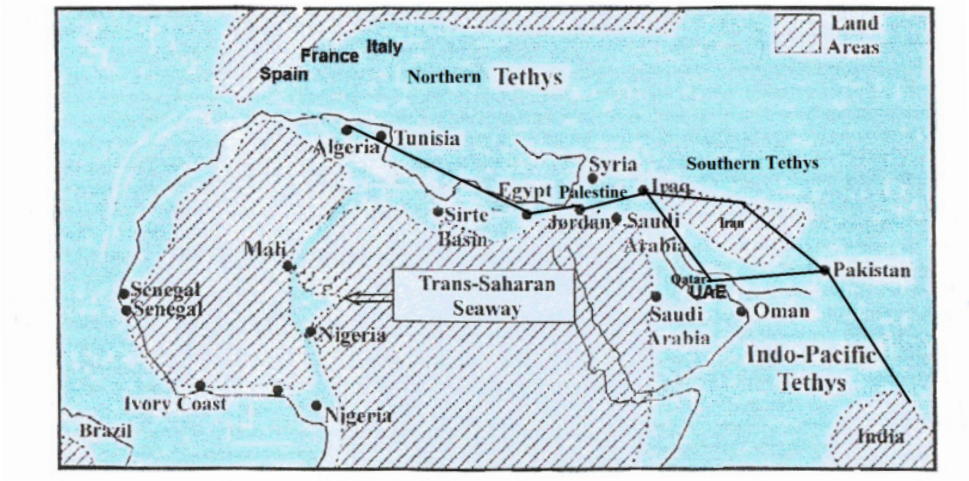

Figure 2. The open sea water between the ten countries in the Southern Tethys during the Paleocene (after Morsi et al. [48], with some modification).

Figure 3. Location map of Giddi and Nekhl sections (Sinai, Egypt), and Beit Jebrin and Jerusalem (Palestine) (after Said & Kenawy [6]).

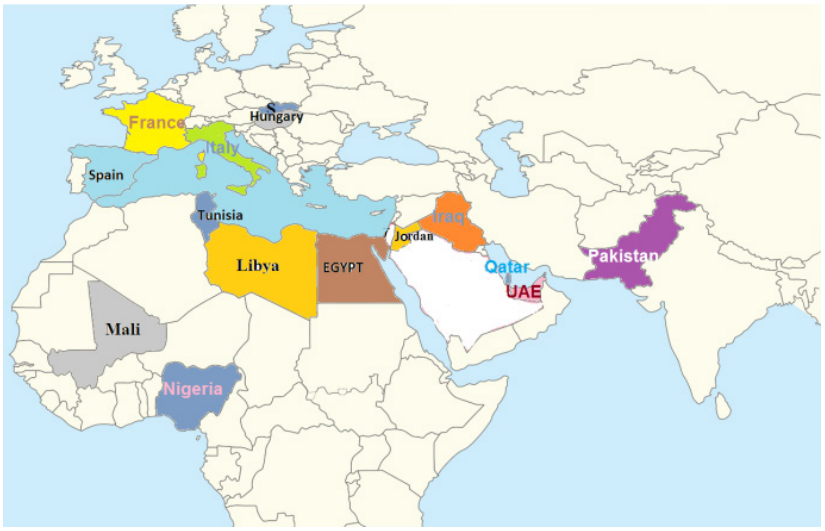

Figure 4. The paleogeographic distribution of the benthic foraminiferal species from the Southern Tethyan: Mali, Nigeria, Tunisia, Libya, Egypt, Jordan, Iraq, UAE, Pakistan, which also recorded in different localities of European Northern Tethys: Spain, Gulf of Biscay, France, Italy, Hungary, Slovenia (after Anan [42]).

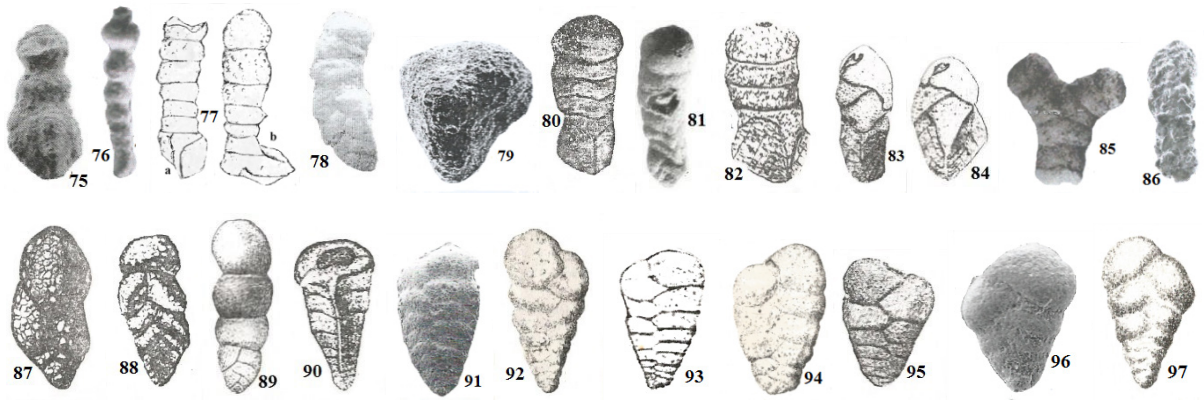

Plate 1

Figure **1.** *Bathysiphon paleocenica* El-Dawy [14] × 10, **2.** *B. saidi* [9] × 10, **3.** *Orbulinoides arabica* Anan [10] × 30, **4.** *Ammovertella qatarica* Hewaidy & Al-Hitmi [18] × 20, **5.** *Repmanina mazeni* (Anan) [20] × 15, **6.** *Rzehakina khatiyahi* Hewaidy & Al-Hitmi [18] × 10, **7.** *Miliammina kenawyi* Anan [9] × 15, **8.** *Agglutinella reinemundi* (Haque [23]) × 80, **9.** *A. sori* (Haque [23]) × 35, **10.** *Dentostomina ammobicarinata* (Haque [23]) × 15, **11.** *D. ammoirregularis* (Haque [23]) × 20, **12.** *D. gapperi* (Haque [22]) × 35, **13.** *Ammomassilina misrensis* Anan [21] × 20, **14.** *Asanospira diyabi* Hewaidy & Al-Hitmi [18] × 10, **15.** *A. jalehaensis* Hewaidy & Al-Hitmi [18] × 17, **16.** *Psammolingulina bahri* Anan [20] × 15, **17.** *Haplophrag-moides desertorum* LeRoy [5] × 30, **18.** *H. iranica* Anan (n. sp.) × 35, **19.** *Ammobaculites bhallai* Habibnia & Mannikeri [25] × 15, **20.** *A. khargaensis* Nakkady [4] × 60, **21.** *A. schwageri* Said & Kenawy [6] × 20, **22.** *Triplasia palmate* Hewaidy & Al-Hitmi, [18] × 10, **23.** *Spiroplectinella esnaensis* (LeRoy [5]) × 20, **24.** *S. hamdani* (Anan [19]) × 15, **25.** *S. henryi* (LeRoy [5]) × 18, **26.** *S. knebeli* (LeRoy [5]) × 16, **27.** *S. paracarinata* Said & Kenawy [6] × 40, **28.** *S. ushbali* (Haque [23]) × 30, **29.** *Trochammina dohaensis* Hewaidy & Al-Hitmi [18] × 15, **30.** *Plectina emiratensis* Anan [10] × 20, **31.** *Tritaxia barakai* Said & Kenawy [6] × 15, **32.** *T. elongata* (Haque [22]) × 20, **33.** *T. limbata* (Haque [22]) × 40, **34.** *Gaudryina aissana* Ten Dam & Sigal [1] × 20, **35.** *G. ameeri* Anan [12] × 20, **36.** *G. arabica* Anan [23] × 35, **37.** *G. ennakhali* Anan [23] × 75, **38.** *G. limbata* Said & Kenawy [6] × 50, **39.** *G. nitida* (Haque [22]) × 40, **40.** *G. osmani* Anan [23] × 35, **41.** *G. rectiangulata* Ten Dam & Sigal [1] × 25, **42.** *G. speijeri* Anan [12] × 20, **43.** *G. salimi* Anan [23] x, **44.** *G. textulariformis* Nakkadyi [4] × 50, **45.** *Pseudogaudryinella iraqensis* Anan (n. sp.) × 10, **46.** *Siphogaudryina africana* (LeRoy [5]) × 10, **47.** *S. daviesi* (Haque [22]) × 20, **48.** *S. elongata* (Haque [22]) × 25, **49.** *S. elegantissima* (Said & Kenawy [6]) × 40, **50.** *S. nammalensis* (Haque [22]) × 30, **51.** *S. nekhlensis* (Said & Kenawy [6]) × 15, **52.** *S. strougoi* Anan [9] × 10, **53.** *S. tellburmaensis* (Futyan [16]) × 25, **54.** *Verneuilina aegyptiaca* Said & Kenawy [6] × 30, **55.** *V. laevigata* Haque [22] × 35, **56.** *V, luxorensis* Nakkady [3] × 30, **57.** *Arenobulimina aegyptiaca* Said & Kenawy [6] × 15, **58.** *A. beitjebrinensis* Anan (n. sp.) × 30, **59.** *A. jerusalemensis* Anan (n. sp.) × 30, **60.** *Textulariella sinaensis* Anan (n. sp.) × 20, **61.** *Dorothia iranica* Anan (n. sp.) × 50, **62.** *D. nammalensis* Haque [22] × 35, **63.** *D. sinaensis* Said & Kenawy [6] × 30, **64.** *Marssonella hafitensis* Anan [10] × 30, **65.** *M. nammalensis* Haque [6] × 50, **66.** *Eggerella maqfiensis* LeRoy [5] × 30, **67.** *Clavulinoides algerianus* Ten Dam & Sigal [1] × 35, **68.** *C. iranica* Anan (n. sp.) × 35, **69.** *lakiensis* Haque [22] × 35, **70.** *C. spatha* Haque [22] × 40, **71.** *Pseudoclavulina barnardi* (Futyan [16] × 35, **72.** *P. farafraensis* LeRoy [5] × 20, **73.** *P. futyani* Anan [20] × 10, **74.** *P. globulifera* Ten Dam & Sigal [1] × 35, **75.** *P. hewaidyi* Anan [11] × 20, **76.** *P. maqfiensis* LeRoy [5] × 40, **77.** *P. pseudoarenata* Said & Kenawy [6] × 40, **78.** *P. youssefi* Anan [20] × 20, **79.** *Valvoreussella karreri* (Said & Kenawy [6]) × 30, **80.** *Clavulina paxilliformis* Haque [22] × 15, **81.** *C. pseudoparisensis* Anan [7] × 10, **82.** *C. symmetrica* Haque [6] × 45, **83.** *Valvulina elongata* Haque [22] × 20, **84.** *V. nammalensis* Haque [22] × 35, **85.** *Thomasinella aegyptia* Omara [2] × 8, **86.** *T. fragmentaria* Omara [2] × 10, **87.** *Bigenerina khirthari* Haque [24] × 30, **88.** *B. metingensis* Haque [22] × 50, **89.** *B. nodosa* Haque [22] × 45, **90.** *Textularia crookshanki* Haque [22] × 45, **91.** *T. fahmyi* Anan [8] × 20, **92.** *T. farafraensis* LeRoy [5] × 30, **93.** *T. haquei* Anan [35] × 22, **94.** *T. nilotica* (Schwager [37]) × 20, **95.** *T. punjabensis* Haque [22] × 35, **96.** *T. salahii* Anan (n. sp.) × 60, **97.** *T. schwageri* LeRoy [5] × 35.

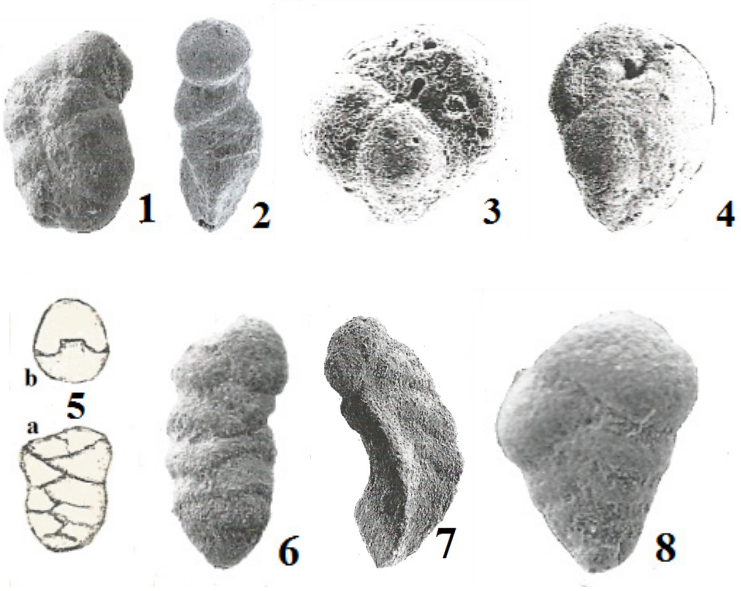

Plate 2 (n. sp.)

Figure **1.** *Haplophragmoides iranica* Anan (n. sp.) × 40, **2.** *Pseudogaudryinella iraqensis* Anan (n. sp.) × 20, **3.** *Arenobulimina beitjebrinensis* Anan (n. sp.) × 70, **4.** *A. jerusalemensis* Anan (n. sp.) × 65, **5.** *Textulariella sinaensis* Anan (n. sp.) × 30, **6.** *Dorothia iranica* Anan (n. sp.) × 120, **7.** *Clavulinoides iranica* Anan (n. sp.) × 80, **8.** *Textularia salahii* Anan (n. sp.) × 150.

4. Paleogeography

The ninety-seven agglutinated benthic foraminiferal species were originally identified from ten countries in the Southern Tethys, as well as some of them were recorded also in some localities in the Southern and Northern Tethys. Many authors (i.e. Said & Kenawy [6], Haque [22], Keller [38], Rögl [39], Rosenbaum et al. [40], Meulenkamp & Sissingh [41], Anan [32,42]). The Tethys had been connected from west with Atlantic Ocean to east with the Pacific with the Pacific Ocean via the Mediterranean Sea during the Campanian-Paleogene time. Anan [42] has recorded many Southern Tethyan benthic foraminiferal species (Tunisia, Libya, Mali, Nigeria, Egypt, Jordan, Iraq, UAE, Qatar, Pakistan), which also recorded in different countries in the Northern Tethys in Europe (Spain, Gulf of Biscay, France, Italy, Hungary, Slovenia (Figure 4).

5. Paleoenvironment

Miller et al. [43] noted that certain hydrographic properties (low oxygen, high CO_3, low pH, and corrosive waters) favor the development of agglutinated assemblages. Loeblich & Tappan [44] noted that the foraminiferal Suborder Astrorhizina reinstated for the typical monothalamous agglutinated taxa whose cementing material is solely organic, and the Family Haplophragmoididae reinstated for multilocular agglutinated taxa with organic cement. Anan [27] noted that most of the recorded species from the Middle-Upper Eocene of Jabal Hafit, UAE (e.g. *Bathysiphon saidi* and *Miliammina kenawyi*) are endemic to the tropical-subtropical regions. Jones [45] noted that the modern smaller agglutinating foraminifera occur in all marine environments, from marginal to deep, and some are tolerant of hyposalinity as well as normal marine salinity, and/or of hypoxia or dysoxia and appear better able than their calcareous benthic counterparts to tolerate conditions of high fresh-water flux, and of high sediment and organic carbon flux, and associated lowered oxygen availability. Moreover, the genera: *Gaudryina*, *Siphogaudryina*, *Verneuilina* in the Subfamily Verneuilininae is restricted to deep marine environments. Orabi [46] noted that the agglutinated tests are weakly held by organic material, which potentially oxidized within the surface layer of sediments. The recorded species represent middle-outer neritic environment (100-200 m) and show an affinity with Midway-Type Fauna (MTF), and the deeper water species have smooth tests, while the shallow water specimens have coarser grained.

6. Conclusions

The present study deals with the recording of ninety-seven identified species belonging to thirty-five agglutinated genera in ten localities of the Southern Tethys: Algeria, Egypt, Palestine, Jordan, Iraq, Qatar, UAE, Iran,

Pakistan and India. Most of these species are confined, so far, on their mentioned localities. Forty species of them are recorded from Egypt (about 41.5%), twenty-seven from Pakistan (~ 28%), ten from UAE (~ 10.5%), six from Qatar (~ 6%), four from Algeria (4.5%), three from Jordan (~ 3%), two from Palestine and Iran (~ 2%), and only one from each of Iraq and India (~ 1%). Seven species of them are believed here as new: Four species from Iran *Haplophragmoides iranica*, *Dorothia iranica, Clavulinoides iranica* and *Textularia salahii*; two species from Palestine *Arenobulimina beitjebrinensis* and *A. jerusalemensis;* one species from Iraq *Pseudogaudryinella iraqensis* and one species from Egypt *Textulariella sinaensis*. The recorded species represent middle-outer neritic environment (100-200 m) in an open marine basin and show an affinity with Midway-Type Fauna (MTF) of the United States Gulf Coastal area.

Acknowledgement

Gratitude expressed to the editor of the Earth and Planetary Science, the unknown reviewers for their valuable comments, and also to my daughter Dr. Huda H. Anan for her help in the development of the figures and plates.

Conflict of Interest

There is no conflict of interest.

References

[1] Ten Dam, A., Sigal, J., 1950. Some new species of Foraminifera from the Dano-Montian of Algeria. Contributions from the Cushman Laboratory for Foraminiferal Research. 1(1, 2), 130-131.

[2] Omara, S., 1956. New foraminifera from the Cenomanian of Sinai. Journal of Paleontology. 30(4), 883-890.

[3] Nakkady, S.E., 1950. A new foraminiferal fauna from the Esna Shale and Upper Cretaceous chalk of Egypt. Journal of Paleontology. 24(6), 675-692.

[4] Nakkady, S.E., 1959. Biostratigraphy of the Um Elghanayem section, Egypt. Micropaleontology. 5(4), 453-472.

[5] LeRoy, L.W., 1953. Biostratigraphy of Maqfi section, Egypt. Geological Society of American Memoir. 54, 1-73.

[6] Said, R., Kenawy, A., 1956. Upper Cretaceous and Lower Tertiary foraminifera from northern Sinai, Egypt. Micropaleontology. 2(2), 105-173.

[7] Anan, H.S., 1984. Littoral recent foraminifera from the Qossier-Marsa Alam stretch of the Red Sea coast, Egypt. Revue de Paléobiologie. 3(2), 235-245.

[8] Anan, H.S., 1994. Benthic foraminifera around Middle/Upper Eocene boundary in Egypt. Middle East Research Center, Ain Shams Univ. Earth Science Series, Cairo. 8, 210-233.

[9] Anan, H.S., 2002. Two new benthic foraminiferal species from the Maastrichtian and Paleocene rocks of northern Egypt. Middle East Research Center, Ain Shams University. Earth Science Series. 16, 141-144.

[10] Anan, H.S., 2003. Three new species of benthic foraminifera from the Middle-Upper Eocene of Jabal Hafit, Al Ain area, United Arab Emirates. Neues Jahrbuch für Geologie und Paläontologie, Mh. 9, 529-536.

[11] Anan, H.S., 2008. Latest Maastrichtian *Plummerita haggagae* and Paleocene *Pseudoclavulina hewaidyi*, two new foraminiferal species from Egypt. Egyptian Journal of Paleontology. 8, 245-254.

[12] Anan, H.S., 2012. A lineage phylogeny from some Cretaceous-Tertiary agglutinated benthic foraminiferal species in Egypt and Tethys. Egyptian Journal of Paleontology. 12, 59-72.

[13] Anan, H.S., 2022. Two new evolutionary lineages of the Maastrichtian-Paleogene *Gaudryina pyramidata* and *Gaudryina arabica* groups in the Tethys. Journal of Microbiology & Experimentation. 10(1), 24-31.

[14] El-Dawy, M.H., 2001. Paleocene benthic foraminiferal biostratigraphy and paleobathymetry, El Sheikh Fadl and Ras Gharib, Eastern Desert, Egypt. Micropaleontology. 4(1), 23-46.

[15] Ali, M.Y., 2003. Micropaleontological and stratigraphical analyses of the Late Cretaceous/Early Tertiary succession of the Southern Nile Valley (Egypt). Der Fakultät für Geowissenschaften an der Ruhr-Universität Bochum vorgelegte Dissertation zur Erlangung des Grades eines. 1-197.

[16] Futyan, A.I., 1976. Late Mesozoic and Early Cainozoic benthonic foraminifera from Jordan. Palaeontology. 19(3), 53-66.

[17] Hewaidy, A.A., Al-Hitmi, H., 1993. Cretaceous-Early Eocene foraminifera from Dukhan oil field, west Qatar, Arabian Gulf (A-Suborders Textulariina, Involutinina and Miliolina). Al-Azhar Bulletin of Science. 4(2), 469-494.

[18] Hewaidy, A.A., Al-Hitmi, H., 1994. Cretaceous-Early Eocene biostratigraphy of the Dukhan oil field, west Qatar, Arabian Gulf. Middle East Research Center, Ain Shams University. Earth Science Series. 8, 1-24.

[19] Anan, H.S., 1993. Maastrichtian-Paleocene micropaleontology and biostratigraphy of Qarn El Barr section, Al Dhayd area, United Arab Emirates. Al-Azhar Bulletin of Science, Al-Azhar University. 4(2), 639-

670.

[20] Anan, H.S., 2021. Paleontology, stratigraphy, paleoenvironment and paleogeography of the seventy Tethyan Maastrichtian-Paleogene foraminiferal species of Anan, a review. Journal of Microbiology & Experimentation. 9(3), 81-100.

[21] Anan, H.S., 2021. Representatives of some diagnostic agglutinated foraminiferal genera of the Subclass Monothalamana (*Bathysiphon, Orbulinelloides, Repmanina, Miliammina, Agglutinella, Dentostomenia, Ammomassilina, Psammolingulina*) in the Tethys. Geological Behavior (GBR). 5(2), 53-58.

[22] Haque, A.F.M.M., 1956. The foraminifera of the Ranikot and the Laki of the Nammal Gorge, Salt Range, Pakistan. Pakistan Geological Survey Memoir. Palaeontologica Pakistanica. 1, 1-229.

[23] Haque, A.F.M.M., 1960. Some middle to late Eocene smaller foraminifera from the Sor Rang, Quetta District, West Pakistan. Pakistan Geological Survey Memoir, Palaeontologica Pakistanica. 2(2), 9-57.

[24] Haque, A.F.M.M., 1962. The smaller foraminifera of the Meting Limestone (Lower Eocene) Meting, Hyderabad Division, West Pakistan. Pakistan Geological Survey Memoir, Palaeontologica Pakistanica. 2(1), 1-43.

[25] Habibnia, B.A., Mannikeri, M.S., 1990. Smaller foraminifera from Eocene beds of Jaisalmer District, Western Rajasthan. Journal of the Palaeontological Society of India. 3, 1-15.

[26] Kaminski, M.A., 2014. The year 2010 classification of the agglutinated foraminifera. Micropaleontology. 60(1), 89-108.

[27] Anan, H.S., 2005. Agglutinated Middle-Upper Eocene foraminifera in Jabal Hafit, Al Ain area, United Arab Emirates. Revue de Paléobiologie. 24(1), 17-27.

[28] Anan, H.S., 2016. Early Paleogene agglutinated foraminifera from the Middle East (Egypt and Arabia) and its distribution in the Tethys. Spanish Journal of Paleontology. 31(2), 353-368.

[29] Salahi, A., 2021. Late Paleocene-Middle Eocene Planktonic and Small Benthic Foraminiferal Fauna from the type section of Khangiran Formation, Kopet-Dagh Basin (NE Iran), Southernmost Peri-Tethys. Stratigraphy and Geological Correlation. 29(3), 303-321.

[30] Aubert, J., Berggren, W.A., 1976. Paleocene benthonic foraminiferal biostratigraphy and paleoecology of Tunisia. Bulletin du Centre de Recherches Pau-SNPA. 10(2), 379-469.

[31] Hewaidy, A.A., Farouk, S., Aly, H.A., et al., 2014. Maastrichtian to Paleocene agglutinated foraminifera from the Dakhla Oasis, Western Desert, Egypt. Egyptian Journal Paleontology. 14, 1-38.

[32] Anan, H.S., 2019. Contribution to the paleontology, stratigraphy and paleobiogeography of some diagnostic Pakistanian Paleogene foraminifer in the Middle East. Earth Sciences Pakistan. 3(1), 29-34.

[33] Jaff, R.B.N., Lawa, F.A., 2018. Palaeoenvironmental signature of the Late Campanian-Early Maastrichtian benthonic foraminiferal assemblages of Kurdistan, Northeast Iraq. Journal of African Earth Sciences. 151, 255-273.

[34] Anan, H.S., 2021. Representatives of some diagnostic agglutinated foraminiferal genera of the Suborder Verneuilinina (*Plectina, Gaudryina, Siphogaudryina, Verneuilina*) in the Southern Tethys. International Journal of Innovative Science, Engineering & Technology. 8(6), 269-281.

[35] Anan, H.S., 2020. Taxonomic consideration and stratigraphic implication of the accelerated evolution of the Maastrichtian-Eocene transition of twenty benthic foraminiferal species in the Tethys. Earth Sciences Pakistan (ESP). 4(1), 01-06.

[36] Almogi-Labin, A., Bein, A., Sass, E., 1990. Agglutinated foraminifera in organic-rich neritic carbonates (Upper Cretaceous, Israel) and their use in identifying oxygen levels in oxygen—poor environments. Paleoecology, Biostratigraphy, Paleoceanography and taxonomy of agglutinated Foraminifera. Kluwer Academic Publication, Netherland. 565-585.

[37] Schwager, C., 1883. Die Foraminiferen aus dem Eocaenablegerungen der Libyschen wuste und Agyptens. Paleontographica. 30, 81-153.

[38] Keller, G., 1992. Paleoecological response of Tethyan benthic foraminifera to the Cretaceous-Tertiary boundary transition. Studies in benthic Foraminifera. Tokai University Press: Tokyo. pp. 77-91.

[39] Rögl, F., 1999. Mediterranean and Paratethys. Facts and hypotheses of an Oligocene to Miocene paleogeography (short overview). Geologica Carpathica. 50(4), 339-349.

[40] Rosenbaum, G., Lister, G.S., Duboz, C., 2002. Relative motions of Africa, Iberia and Europe during Alpine orogeny. Tectonophysics. 359, 117-129.

[41] Meulenkamp, J.E., Sissingh, W., 2003. Tertiary palaeogeography and tectonostratigraphic evolution of the Northern and Southern Peri-Tethys platforms and the intermediate domains of the African-Eurasian convergent plate boundary zone. Palaeogeography, Palaeoclimatology, Palaeoecology. 196, 209-228.

[42] Anan, H.S., 2020. Southern Tethys benthic foraminifera in Northern Tethys. Earth Sciences Pakistan

(ESP). 4(2), 70-75.

[43] Miller, K.G., Gradstein, F.M., Berggren, W.A., 1982. Late cretaceous to early tertiary agglutinated benthic foraminifera in the Labrador Sea. Micropaleontology. 28(1), 1-30.

[44] Loeblich, A.R., Tappan, H., 1989. Implications of wall composition and structure in agglutinated foraminifers. Journal of Paleontology. 63(6), 769-777.

[45] Jones, R.W., 2014. Foraminifera and their applications. Cambridge University Press: Cambridge. pp. 1-391.

[46] Orabi, O.H., 2020. Morphological abnormality observed in the species *Ammobaculites texanus* Cushman and paleoenvironmental implications. Revue de Micropaléontologie. 68(100444), 1-9.

[47] Morsi, A.M., Faris, M., Zalat, A., et al., 2008. Maastrichtian-Early Eocene ostracodes from west-central Sinai, Egypt—taxonomy, biostratigraphy, paleoecology and paleobiogeography. Revue de Paléobiologie. 27(1), 159-189.

Earth and Planetary Science
https://ojs.nassg.org/index.php/eps/index

RESEARCH ARTICLE

Assessment of Pollution and Identification of Sources of Heavy Metals, and Radionuclides Contamination in Sand along the Southern Part of the Cameroonian Coast (South-West, Africa)

Francis Temgo Sopie[1] Victorine Ambassa Bela[2] Armel Zacharie Ekoa Bessa[2*] Archange Duviol Tsanga[2] Patrice Roland Liyouck[1] Théophile Njanko[1] Gabriel Ngueutchoua[2]

1. Department of Earth Sciences, University of Dschang, Dschang, Cameroon
2. Department of Earth Sciences, University of Yaoundé I, Yaoundé, Cameroon

ARTICLE INFO

Article history
Received: 15 April 2022
Revised: 19 May 2022
Accepted: 24 May 2022
Published Online: 2 June 2022

Keywords:
Pollution indices
Statistical analysis
Ecological risk
Heavy metals and radionuclides
Source identification

ABSTRACT

Sandy sediments collected along the southern part of the Cameroonian coast have been analyzed geochemically by ICP MS methods to investigate the distribution characteristics, contamination levels and related ecological risks. In these sediments, the concentration (mg/kg) of selected elements are in order Fe > Mn > Cr > V > Th > Ni > U > Co. Indices of pollution such as index of geoaccumulation, where values of all elements in the sediments were < 0, except Th in the sediments station of Yoyo II, and Cr in sediment of all stations were Igeo > 0. The contamination factor shows that the station of Yoyo II has values of CF < 1, such as Fe, V, Ni and Co. While Uranium, Th and Mn values vary from 1 to 3 and 3 to 6, and for Cr values of CF > 6. However, Kribi and Campo stations show that all the elements have values of CF < 1, except Cr which has values of CF > 6. The degree of contamination values ranges between (9.48-37.13) for the station of Yoyo II, (8.84-17.62) for the Kribi station, and (6.52-13.56) for the Campo station. The pollution loading index values at all sampling stations are lower than 1. The potential ecological risk (Er and RI), indicates that this coastal area is a low risk region. Pearson correlation, cluster analysis and principal component analysis supported that heavy metals (Fe, Mn, Cr, V, Ni and Co) have common human influences while radionuclides (Th and U) have a natural source. The presence of human activities such as domestic waste, intensive farming and the processing of industrial products could be potential sources of anthropogenic environmental pollution, thereby threatening the environmental concerns of the entire study area.

*Corresponding Author:
Armel Zacharie Ekoa Bessa,
Department of Earth Sciences, University of Yaoundé I, Yaoundé, Cameroon;
Email: armelekoa@yahoo.fr

DOI: http://dx.doi.org/10.36956/eps.v1i1.525

Copyright © 2022 by the author(s). Published by Nan Yang Academy of Sciences Pte. Ltd. This is an open access article under the Creative Commons Attribution-NonCommercial 4.0 International (CC BY-NC 4.0) License. (https://creativecommons.org/licenses/by-nc/4.0/).

1. Introduction

Over the past two decades, pollution of aquatic sediments has become a worldwide environmental concern [1]. Heavy metals in deposition persist in the environments, which poses a risk, not only to benthic but also to aquatic biota, as metals in sediments can be discharged into the aquatic overlying waters through both chemical and biological processes [2,3]. The characteristics and behavior of coastal habitats are diverse and changing. There are sandy beaches, which can be considered as the geographical area where the marine and terrestrial ecological systems interact. Such settings are critical for the survival of a wide range of plants and animals, as well as a wide range of economic activities. In recent years, there has been an increase in global concern about the effects on coastal habitats [4-6]. Pollution from industrial activities such as discharges of urban sewage, fishing activities, and the combustion of fossil fuels via the dumping of solid waste has extensively affected the environments throughout the land-linked coastline [6-8]. As a result of their highly toxicity, prolonged occurrence, slow rate of degradation, and simple accumulation by marine biota, heavy metals in sediments have received scientific attention and public concern recently [3,9]. Metals including Pb, Cd, Zn, Cr, Cu, and Ni are predominantly mobilized by human activity, while other metals like Al, Fe, Co, and Mn are of lithogenic origin [10]. Natural radiation has been a part of human life throughout history. Its principal mechanisms are cosmogenic and cosmic gamma radiation, terrestrial gamma radiation from naturally occurring radionuclides in soils, sediments, and rocks, and naturally occurring radioactive constituents in our food and inhaled air [5,11,12]. Uranium and thorium are found in fairly low abundances in rocks, soils, and sediments [5]. Thorium is a strikingly abundant element in the Earth's crust, almost three times more abundant than uranium [13]. Felsic rocks (e.g. granite) have been found to have higher U and Th content than mafic rocks like basalt and andesites [5,14].

Heavy metals in coastal sediments are the result of natural processes and/or anthropogenic activities. The background values for heavy metals are determined by natural processes such as atmospheric input, Aeolian processes, and crustal movements [3]. Industrialization and agricultural practices are linked to anthropogenic heavy metals inputs. The major anthropogenic inputs are from sources including atmospheric deposits, waste disposal, waste combustion, urban effluents, traffic emissions, fertilizer application, and long-term application of wastewater to farmland [4]. To investigate the source of heavy metals in terrestrial and littoral environments, several factors need to be examined, such as grain size, mineral composition, and the sedimentary environment. Metals that have leached into sediments from anthropogenic sources, on the other hand, are more commonly present in relatively more bioavailable forms [15,16]. Soil erosion, natural weathering of the Earth's crust, mining, industrial effluents, urban runoff, sewage discharge, and pest or disease-control agents are all sources of heavy metals in today's crops [17,18]. Therefore, the purposes of the present study were: (i) to determine the spatial distribution of selected heavy metals contents along the Southern part of the Cameroonian coast; (ii) to assess heavy metal contamination levels and potential ecological risk in the study area based on the geo-accumulation index and potential ecological risk; (iii) to definite the possible source of pollutants using multivariate statistical analyses.

2. Materials and Methods

2.1 Study Area

The area under study is located in the southern part of the Cameroonian coast, near the mouth of the Sanaga River located on the Atlantic Ocean coast, ranging from 2°20' to 3°40' N and 9°40' to 10°20' E in southwestern (SW) Cameroon (Figure 1). The wet season lasts from March to November, and the dry season lasts from December to February. The soils in this area are ferralitic and hydromorphic [19]. The main activities in this area are artisanal fishing and agriculture. The geology of the Cameroonian coast is dominated by sedimentary strata associated with the Douala Basin. From the Upper Cretaceous to the Tertiary, marine transgression has sculpted these strata [20,21]. The Douala sub-basin is located in the Gulf of Guinea between the Cameroon Volcanic Line and the Rio Muni basin in Cameroon. According to Nguene et al. [22] and Lawrence et al. [23], three major events in geodynamics and sedimentary history can be distinguished: (i) the early Cretaceous extensional rift to drift phase; (ii) the transition from rift to drift highlighted by the accentuation of transformed directions caused by a series of cross faults; and (iii) the late Cretaceous and Tertiary passive margin wedge. The Cameroonian coast is unconformably underlain by the Precambrian basement and begins with a marl and fossiliferous limestone marine series of lower Turonian-Campanian age and is continued by a Campanian-Paleocene continental series to date [24]. Also known as the Dizangue series, it is composed of small conglomerates at the base, and fine and coarse sandstones at the top. The series also contains interbedded clay, kaolinite, and ferruginous sandstone [20,25]. In the Sanaga upstream basin, there is a succession of fine, black and beige sandstones and Middle Cretaceous arkosic conglomeratic sandstones [6].

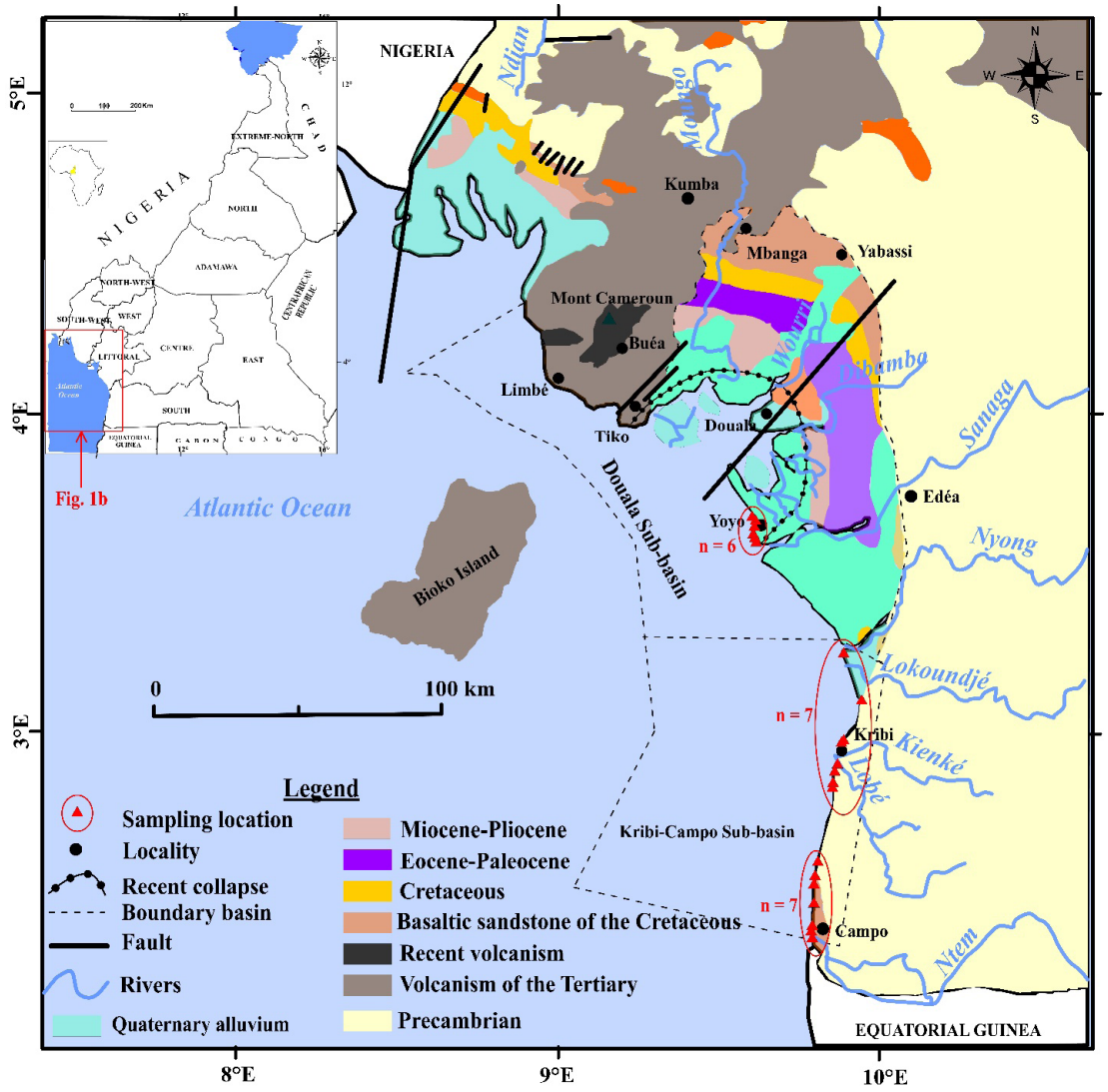

Figure 1. Investigated area and sampling location: a) location of the study area and in Cameroon; b) Location of sampling area and station along the southern part of the Cameroonian coast.

2.2 Sample Collection and Analysis

The sediments were sampled at three sites, for a total of 20 samples collected, selected according to the type of slope, surroundings and sampling of the sediments and water along the coastal shoreline. The three sites are Yoyo II, Kribi and Campo. Sampling was collected in February 2022, at the designated locations, with the use of a trowel. This one is used to scrape off the top layer 10-15 cm) of sediment to prevent contamination. Polyethylene bags have been used to pack and carry the samples to the laboratory. About 2 kg of each sample was collected. The samples were then air-dried, ground, and then sieved. The ground samples, 0.2 g (ground, sieved with a 0.080 mm) have been prepared and mixed with 1.5 g of $LiBO_2$. The mixture was then dissolved in 100 mL of 5% HNO_3. The metal concentration intensity of Fe, Mn, Cr, V, Ni, Th, U and Co was determined in air/acetylene fire by inductively coupled plasma mass spectrometry (ICP-MS) from ALS (Australian Laboratory Services), Vancouver, Canada. Analytical doubts ranged from 0.1 to 0.5% for trace metals. The detection limits vary from 0.05×10^{-6} mg/g to 4.0×10^{-6} mg/g according to the element.

The statistical descriptions of heavy metals were obtained from the PAST program (version 1.72). Box and whisker plots of sediment quantification were drawn for the three sites to show the variation in the heavy metal concentrations investigated. Furthermore, the heavy metal data from the three sites were subject to agglomerative hierarchical analysis (AHC) and principal component analysis (PCA) to build a correlation matrix, and to identify if a significant variation between the different treatments exists. The PCA was carried out with the statistical software

package XLSTAT, version 14.

2.3 Assessment Methods of Sediment Pollution

2.3.1 Geoaccumulation Index (Igeo)

Popular measure to determine the extent of metal deposition in sediments is the geoaccumulation index (Igeo) Chen et al. [26] and Singovszka and Blintova [27]. The Igeo takes into account both the impact of human activities and the background concentration of the area. The index is expressed mathematically as follows:

$$Igeo = \log_2 (C_i/k \times B_i) \quad (1)$$

where C_i denotes the content of element (i) in the selected materials, B_i denotes the geochemical content of element (i), and k is a factor that accounts for probable lithogenic effect variation in background data. Factor k normally has a value of 1.5. There are six classes on the Igeo scale, varying from unpolluted to very strongly polluted (Table 1).

2.3.2 Contamination Factor (CF), Degree of Contamination (DC) and Pollution Load Index (PLI)

The CF is the calculated ratio resulting from the following equation [28]:

$$CF = (C_{metal} / C_{background}) \quad (2)$$

C_{metal} is the concentration of pollutants in the deposits and $C_{background}$ refers to the background metal concentrations. We classified the CF into four groups to measure the contamination level (Table 1).

The degree of contamination (DC) is the sum of all contamination factors for a given site [29]. The DC can be calculated using the equation:

$$DC = \sum_{i=1}^{n} CFi \quad (3)$$

in which CF is the single contamination factor and n is the element amount present. DC < n, would denote a low degree of contamination; n ≤ DC < 2n, moderate degree of contamination; 2n ≤ DC < 4n, considerable degree of contamination and DC > 4n, very high degree of contamination. For this studied heavy metals n = 8.

The pollution load index (PLI) is a combined approach of factors in the studied area [30]. The PLI could indicate temporal and spatial variance, as well as each element's contribution to overall pollution [28]. The pollution load index (PLI) is calculated using an equation from Tomlinson et al. [28].

$$PLI = \sqrt[n]{(CF1 \times CF2 \times CF3 \times ..... \times CFn} \quad (4)$$

n is the number of metals, while CF refers to the contamination factor. The pollution loading index was interpreted by Tomlinson et al. [28] and Suresh et al. [31]. The PLI is categorized into three ranks as described in Table 1.

2.3.3 Ecological Risk Assessment

For the current study, a prospective ecological risk factor (E^i_r) and a possible ecological risk index (RI) were used to estimate the ecological risk. The ecological risk potential is determined using Håkanson [29] technique. The RI was created in order to quantify the extent of trace metals contamination in sediments, as well as their toxicity and environmental impact.

$$E_r^i = Tr \times CF \quad (5)$$

$$RI = \sum_{1}^{n} Er^i \quad (6)$$

RI denotes the sum of all risk factors for heavy metals in the selected sediment, (Eri) is the potential monomial environmental risk factor proposed by Håkanson [29] and Suresh et al. [31]; Tr is the toxic response factor proposed by Håkanson [29] for three metals Mn (1), Cr (2), and Ni (5),

Table 1. Classes of pollution indices and contamination levels used in the study.

I-geo value ; classes	Pollution level	Er classes	Er level
I-geo ≤ 0 ; 0	Unpolluted	Er < 40	Low potential ecological risk
I-geo = 0-1 ; 1	Unpolluted to moderately polluted	Er = 40-80	Moderate potential ecological risk
I-geo = 1-2 ; 2	Moderately polluted	Er = 80-160	Significant potential ecological risk
I-geo = 2-3 ; 3	Moderately to strongly polluted	Er = 160-320	High potential ecological risk
I-geo = 3-4 ; 4	Strongly polluted	Er > 320	Very high potential ecological risk
I-geo = 4-5 ; 5	Strongly to very strongly polluted		
RI classes	Risk level	CF classes	Contamination level
RI <150	Low ecological risk	CF < 1	Low contamination
RI = 150-300	Moderate ecological risk	CF = 1-3	Moderate contamination
RI = 300-600	Significant ecological risk	CF = 3-6	Considerable contamination
RI > 600	High ecological risk	CF > 6	High contamination

and CF is the contamination factor determined by Equation (2). The expressions and values used for the ecological risk assessment interpretation are presented in Table 1.

2.4 Multivariate Statistical Analyses

The statistical analysis was carried out with Microsoft Excel version 16, whereas Surfer 16 was used to plot the maps. Heavy metals in sediment for each individual habitat were performed in a one-way ANOVA with equal probability replication at the 0.05 level (Duncan's test) by using the program COSTAT 6.3. In this study, multivariate statistical analysis was carried out using Pearson correlation, cluster analysis, and principal component analysis (PCA).

3. Results and Discussion

3.1 Distribution of Heavy Metals and Radionuclides

The distribution of heavy metals (Fe, Mn, Cr, V, Ni, Co) and radionuclides (Th and U) observed in the beach sand along the Southern part of the Cameroonian coast is presented in (Table 2). The mean concentration (mg/kg) of these elements were found in the following decreasing order as Fe (4755.92-116,450.1) > Mn (77.45-3407.8) > Cr (547.36-957.88) > V (5-318) > Th (0.46-161) > Ni (4-22) > U (0.21-21.9) > Co (1-18) (Table 2). However, all metals are higher than the average Shales values [32] except Ni and Co which have lower values (Table 2). Metal concentrations in sediments vary due to changes in bedrock composition, sediment texture, sediment transport, mineral sorting, and anthropogenic activities [5,33]. Activities such as runoff from agricultural land, exposure of the Atlantic Ocean to substantial releases of pollutants from industrial processes, and untreated domestic sewage from residential areas may have raised the concentration of these metals in this coastal area [25]. The highest concentration of Fe is most likely to be caused by natural processes such as leaching of source rocks, transported from the continent and transported directly from the ocean by rivers and wave movements [6,25]. Similarly, increasing Fe concentrations could have been caused by urban and industrial waste, as well as corrosion of underwater structures [34,35]. Manganese has been found in a variety of amounts as a natural trace element in crude oils, which has been used to improve fuel oil combustion [36]. The average amounts found in this study are attributed to the presence of mangrove vegetation [6,37]. The amounts of Cr could be linked to the pollution load resulting from diverse agricultural wastes [5]. The occurrence of Cr in this study could be attributed to the combustion of plastic trash, anthropogenic waste dumping, and tourism-related sludge dredging. Vanadium is found in carbon-rich materials like crude oil, coal, oil shale and oil sands. Because V is generally relatively soluble, weathering is an essential way for it to be distributed in the environment. It's found in algae, plants, invertebrates, fish, and a variety of other species. Furthermore, human activities such as marketplaces and garages would be responsible for the high values of V in sands [6,38]. Natural weathering and rock leaching can cause Ni to reach the environment [39]. Fishing, tourist activities, and rock leaching could all contribute to the moderate Ni concentration. Cobalt is rarely found naturally in the environment. It is usually manufactured as by-product of nickel and copper mining. When Co particles are not attached to soil or sediment particles, however, plant and animal uptake is stronger, and buildup in plants and animals is possible. Furthermore, the significant concentration of Co could be related to the presence of iron and manganese oxyhydroxide in sediments because Co is considered a low mobility element in sediments and has a strong affinity with iron and manganese oxyhydroxide. Thorium is a radioactive element and can be found in low concentrations in most rocks and soils. This element circulates very little in nature due to its high insolubility when it is in the oxide form [5,40]. In addition to Th, U is radioactive, but it is not especially rare. It can occur in minor quantities in rocks and sediments, in both water and air, in varying concentrations that are generally very low. However, due to its solubility in water, which determines its mobility in the environment as well as its toxicity, U is unlikely to be found in fish or vegetable products [5,12,41]. In this study, high concentrations of U in the sediments would be due to anthropogenic activities such as the use of coal, and phosphate fertilizers in agricultural production.

3.2 Geoaccumulation Indices of Heavy Metals and Radionuclides

The geoaccumulation index (Igeo) of the different metals (Fe, Mn, V, Ni, Co) and radionuclides (Th and U) of the sediment samples from Yoyo II, Kribi and Campo are given in Appendix 1. The station of Yoyo II shows that most of the metals contained in the samples have values of Igeo < 0, while Cr and Th have values of Igeo > 0 (Appendix 1; Table 1). The results obtained show that, the sediments of Yoyo II are mostly unpolluted in Fe, Mn, V, Ni, Co and U, and moderately to strongly polluted in Cr and Th (Table 1; Figure 2). The results are similar to those of Chougong et al. [5] on the alluvial sediments of the Lobé river in Cameroon. The results obtained in the Kribi and Campo sediment samples are similar for both heavy metals and radionuclides (Th and U). Sediments from these two sites have values of Igeo < 0 in most samples, except for Cr which has values of Igeo > 0 in all samples from

both sites (Appendix 1; Table 1). The sediments of the Kribi and Campo site are all unpolluted in Fe, Mn, V, Ni, Co, Th and U. Moreover, these same samples show that the sediments of Kribi and Campo location are moderately to strongly polluted in Cr (Table 1; Figure 2).

These results corroborate those obtained on beach sediments along the Littoral zone of Cameroon [6]. Moreover, these results are far from those obtained on the sediments of the various beaches of Limbé which shows that, the sediments are polluted in Co, Ni, Cu and Cd on the one hand, and on the other hand unpolluted in Zn, Cr, Fe and Mn [25]. The unpolluted nature of sediments in these different sites would be due to the fact that the various anthropogenic activities carried out in these areas do not contribute significantly to the contamination of the sediments. High Cr Igeo values suggest that sediment retains more Cr than other metals [5,42].

Table 2. Descriptive statistical of heavy metals and radionuclides concentration (mg/kg).

ID	Fe	Mn	Cr	V	Ni	Co	Th	U	Station
Yo1	21471.58	309.8	615.78	37	9	5	8.9	1.46	
Yo2	40355.38	1084.3	684.2	102	14	7	51.7	7.66	
Yo3	99314.8	2943.1	752.62	272	19	15	150	19.2	
Yo5	28115.88	542.15	821.04	53	11	5	30	4.2	
Yo6	116450.1	3407.8	684.2	318	22	18	161	21.9	Yoyo II
PYo0	16645.72	154.9	752.62	23	9	4	2.9	0.8	
Min	16645.72	154.9	615.78	23	9	4	2.9	0.8	
Max	116450.1	3407.8	821.04	318	22	18	161	21.9	
Mean	53725.58	1407.01	718.41	134.17	14	9	67.42	9.20	
SD	43040.91	1413.26	71.756	128.23	5.44	5.97	70.44	9.16	
Lje	12169.56	154.9	684.2	15	7	3	3.1	0.61	
Lji	46230.34	1471.55	684.2	156	19	10	40.6	7.11	
Lo2	45181.24	697.05	615.78	72	14	10	8	1.82	
Lo1	17065.36	232.35	752.62	22	7	2	2.4	0.62	
Lb	19862.96	309.8	752.62	24	9	4	4.3	0.9	
EB2	31822.7	542.15	615.78	60	12	6	6.9	1.42	Kribi
Eb1	31053.36	232.35	889.46	59	14	6	4.4	1.25	
Min	12169.56	154.9	615.78	15	7	2	2.4	0.61	
Max	46230.34	1471.55	889.46	156	19	10	40.6	7.11	
Mean	29055.07	520.02	713.52	58.29	11.71	5.86	9.96	1.96	
SD	13416.81	461.93	95.60	48.49	4.39	3.18	13.66	2.31	
CD	23709.66	309.8	957.88	30	11	5	3.9	0.87	
CE	41894.06	1084.3	752.62	84	14	8	12.5	2.67	
CRL	48258.6	929.4	684.2	91	17	8	9.9	2.51	
CB1	4755.92	77.45	547.36	5	4	1	0.46	0.21	
CB2	24199.24	309.8	684.2	30	10	5	2.1	0.74	
CV1	27486.42	542.15	821.04	52	10	6	12.6	2.07	Campo
CV2	20282.6	309.8	547.36	28	9	4	10.2	1.15	
Min	4755.92	77.45	547.36	5	4	1	0.46	0.21	
Max	48258.6	1084.3	957.88	91	17	8	12.6	2.67	
Mean	27226.64	508.96	713.52	45.71	10.71	5.29	7.38	1.46	
SD	14330.80	368.35	147.05	31.68	4.07	2.43	5.09	0.95	
Average Shale	47,200	850	90	130	68	19	12	3.7	-

Average shale, after Turekian and Wedepohl [5].

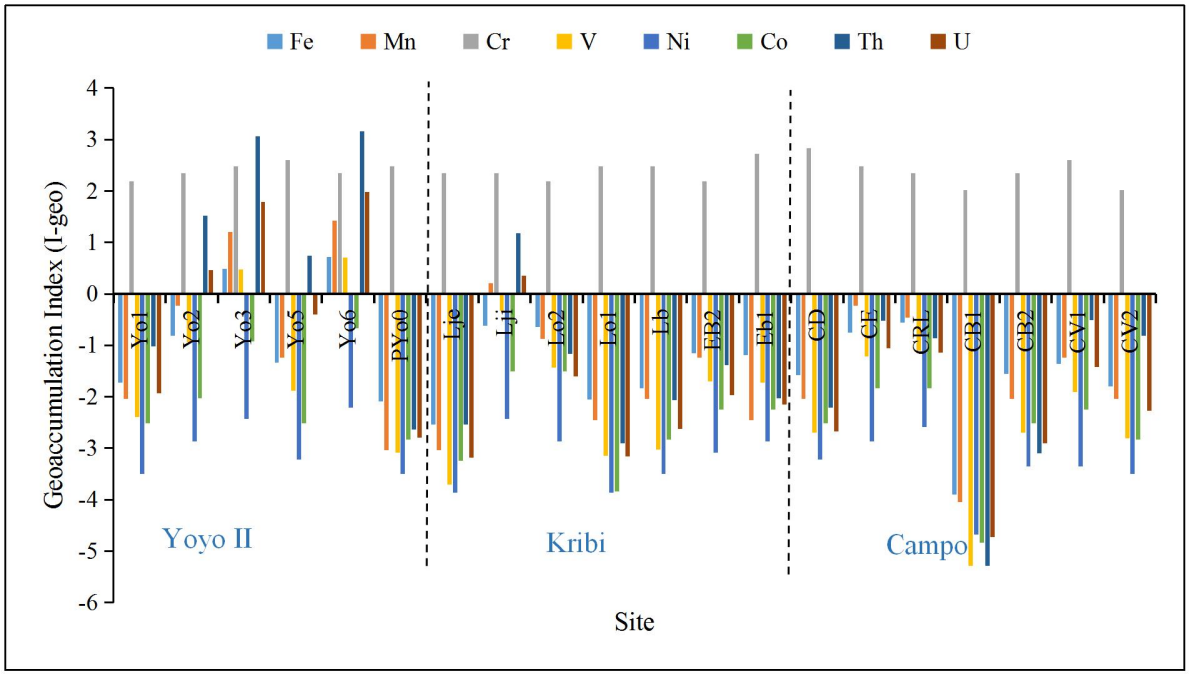

Figure 2. Calculation of geoaccumulation indices of different metals and radionuclides in the sediment of southern part of the Cameroonian coast.

3.3 Contamination Factor (CF), Degree of Contamination (DC) and Pollution Load Index (PLI)

The contamination factor (CF) was determined using Equation (3). In this study, CF is classified into four classes for the sediment samples from Yoyo II (Table 1; Appendix 2; Figure 3). In the Yoyo II, Fe, V, Ni, and Co have values of CF < 1, as well as some samples containing Mn, Th, and U. These values suggest that the sediments would be low contamination (Table 1; Figure 3). Uranium, Th, and Mn have samples that mostly fall into the class where CF values vary from 1 to 3 and 3 to 6, meaning that, the sediments are moderate to considerably contaminated. Chromium has values of CF > 6 in all the samples. This is also observed in two samples containing Th. These values indicate a high rate of contamination (Table 1; Figure 3). The locality of Kribi and Campo shows that, in most of the samples studied, all the metals have values of CF < 1, meaning that these sediments are weakly contaminated, except Cr which has values of CF > 6, meaning that, the sediments of Kribi and Campo are strongly contaminated with Cr (Appendix 2; Table 1; Figure 3). The low, moderate and considerable contamination of the sediments of the studied samples by these metals would be caused by the impact of external discontinuous sources such as agricultural runoff, and other anthropogenic contributions such as household waste dumping, tourism and fishing activities. This outcome is consistent with that obtained by Ekoa Bessa et al. [39,25,6] in sediments from the Moloundou swamp, sediments from the coastal areas of Limbé in the northern part of the coastline, and investigated sediments along the coastal zone of Cameroon, respectively. The same result was obtained by Mandeng et al. [12] in sediments of the Abiete-Toko gold district, Southern Cameroon. Moreover, the high Cr contamination is thought to be due to emissions from industry such as sludge combustion and tanneries, and anthropogenic activities such as the frequent use of phosphate fertilizers on soils. The degree of contamination (DC) values range between (9.48-37.13) for the Yoyo II station; (8.84-17.62) for the Kribi station and (6.52-13.56) for the Campo station. DC values obtained in the studied sediments show that these sediments have a moderate, considerable and high degree of contamination ($8 \leq DC < 32$ and $DC > 32$). The results from each station are presented and observed in (Appendix 2; Figure 4). These results confirm those obtained on the CF, this could be due to the anthropogenic inputs, industrial activities, soil leaching and agricultural runoff.

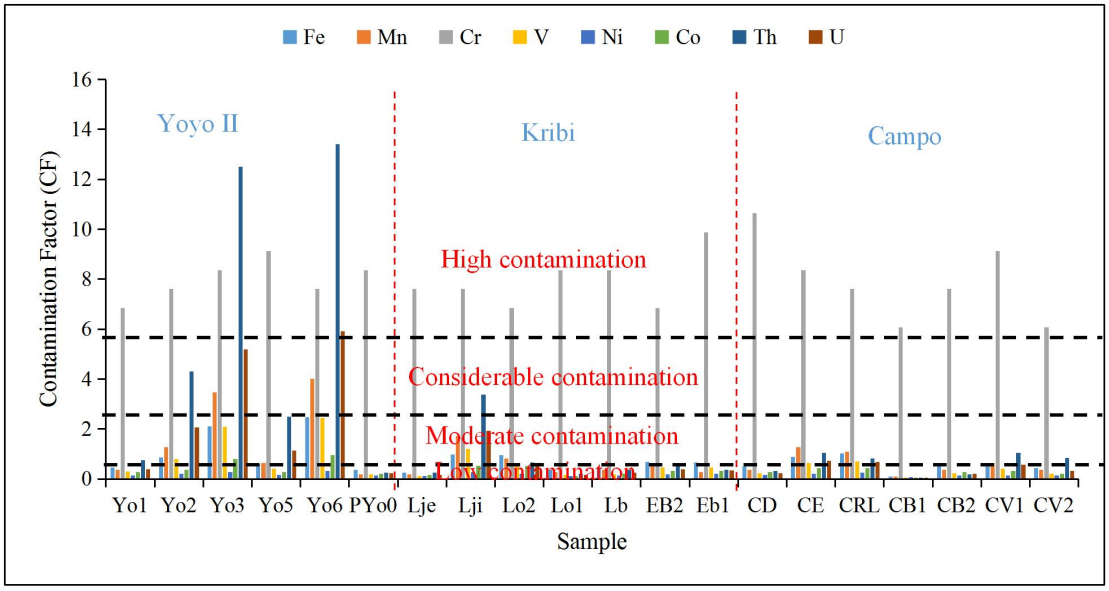

Figure 3. Contamination factors of different metals and radionuclides in the sediment of southern part of the Cameroonian coast.

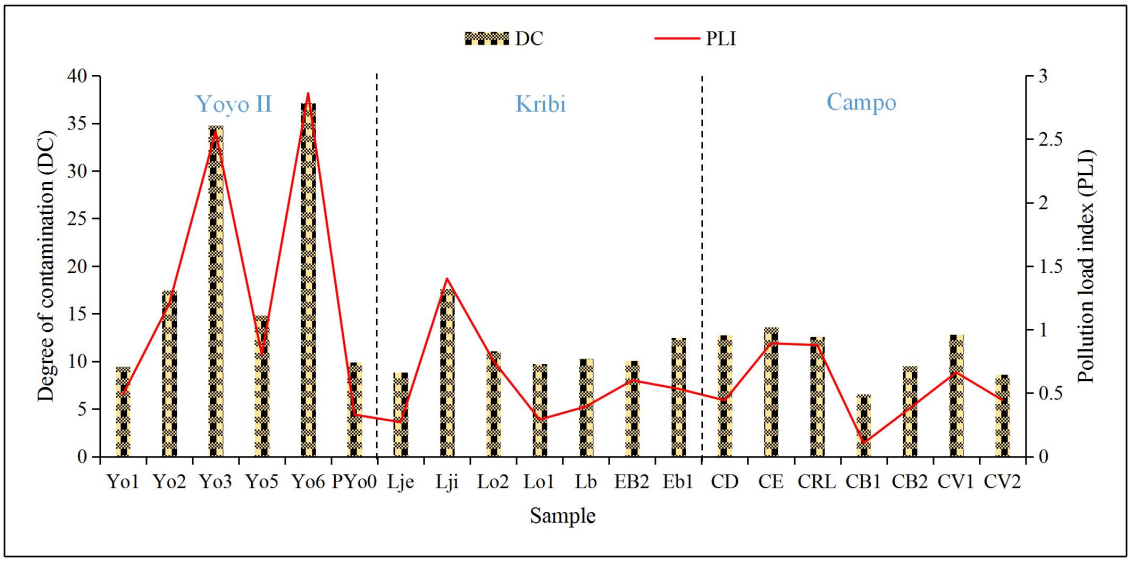

Figure 4. Degree of contamination (DC) and pollution load index (PLI) of metals and radionuclides of southern part of the Cameroonian coast.

The pollution load index (PLI) was calculated from Equation (4) for the sediment samples in this study, and their spatial distribution is shown in Figure 4. Appendix 2 gives a summary of the calculated values of the selected analyzed metals. The PLI values in all sampling stations are less than 1 and the sediments are classified as unpolluted, except at the Yoyo II station which shows that 50% of the samples from this station are contaminated with metals to some degree. The PLI in this study is very low when compared to other coastal environments reported by Ekoa Bessa et al. [25], and Sankarappan et al. [35]. While the high values recorded in these sediments are similar to those collected in the sediments of Moloundou Swamp, eastern Cameroon [39], as well as those of the Lobé River in Cameroon [5].

3.4 Assessment of Potential Ecological Risk

Beyond the assessment of heavy metal concentrations, an ecological assessment of heavy metals is required to understand potential harmful effects. The results of the potential ecological risk factor (Er) and the potential ecological risk index (RI) of heavy metals of the three stations

studied along the Southern part of the Cameroonian coast are given in Appendix 3 and Figure 5. The Er of the three stations (Yoyo II, Kribi and Campo) showed a low potential ecological risk factor (Er < 40) for the trio Mn, Cr and Ni (Table 1, Appendix 3 and Figure 5). The RI of heavy metals studied in the sediments of three stations showed a low index of ecological risk. In general, in the sediments of this southern part of Cameroonian coast, the possible ecological evaluation (Er and RI) of heavy metals trends to Cr > Mn > Ni. The study region is a low risk zone, according to the ecological risk assessment, which could be due to anthropogenic activities and which could affect the concentration of heavy metals. These results are in agreement with those of several authors, in particular the results obtained by El-Amier et al. [18], in the sediments of Mediterranean Sea Drain Estuaries in Egypt; those obtained by Ekoa Bessa et al. [25], in the beach sediments along the Atlantic Ocean (Limbe costal fringes, Cameroon) and those obtained by Mandeng et al. [12], in the sediments of Abiete-Toko gold district, southern Cameroon.

3.5 Statistical Analysis

A Pearson correlation analysis was realized using COSTAT 6.3 software. The correlation coefficient values of this study are listed in Table 3. Pearson correlation indicates that the Fe concentration was significantly positive, correlated ($p < 0.01$) with Mn, V, Co (0.98), U (0.94), Th (0.93), Ni (0.89). However, several elements such as Co, Th and U had significant positive correlations ($p < 0.01$) with V (0.96), Mn (0.95), Ni (0.93); Mn (0.96), Co (0.87), Ni (0.73) and Mn (0.98), V (0.97), Co (0.89), Ni (0.77), respectively. A positive relationship between Co, Mn and Ni demonstrated a characteristic natural origin of these components in the sediments while good correlation between each other could suggest the important activity from anthropogenic sources, and that they can be affected by possible additions [5].

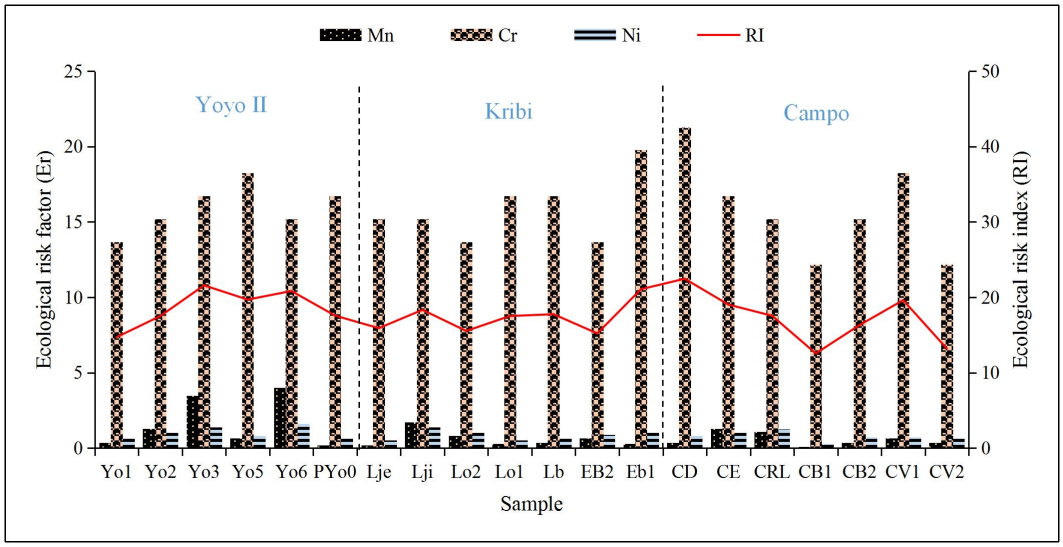

Figure 5. Calculation of potential factor index (Eri) and potential ecological risk index (RI) in sediments from sampling stations along the southern part of the Cameroonian coast.

Table 3. Pearson correlation.

Elements	*Fe*	*Mn*	*Cr*	*V*	*Ni*	*Co*	*Th*	*U*
Fe	1							
Mn	0.98	1						
Cr	0.03	–0.02	1					
V	0.983	0.99	0.00	1				
Ni	0.893	0.85	0.12	0.88	1			
Co	0.98	0.95	0.02	0.96	0.93	1		
Th	0.93	0.96	0.00	0.96	0.73	0.87	1	
U	0.94	0.98	0.01	0.97	0.77	0.89	1.00	1

Correlation is significant at $p < 0.05$.

To better comprehend the link between these variables and determine their origin, principal components analysis was performed on sediment characteristics and heavy metals. The first two main components with eigenvalues greater than 1 account for 94.57% of the total variance, as illustrated in supplemental Appendix 4 and Figure 6. As a result, these two components play an important role in explaining heavy metal contaminations and their source in the studied area.

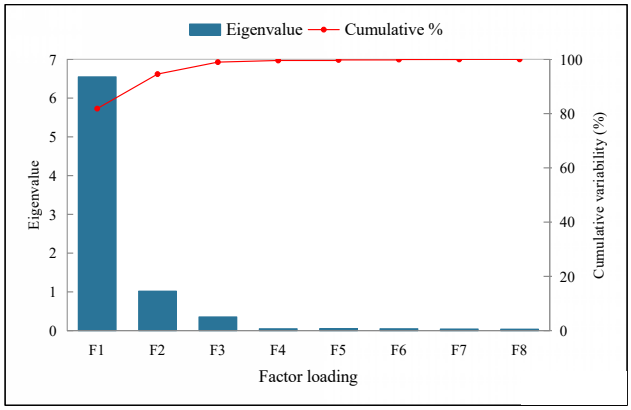

Figure 6. Scree plot, eigenvalue and variance of principal components.

The results revealed that the first main component (F1) accounted for 81.83% of total variation, with substantial loadings encompassing all of the factors tested (Figure 7a). The existence of Fe in the same components indicates that all elements are positively associated to this group, which could imply that these elements have a natural origin. The second principal component (F2) accounted for 12.27% of total variance (Figure 7a). This group shows an absence of anthropogenic and natural activity. Chromium, Ni and Co are derived from the terrigenous detrital matter carried by runoff and the lithological features of the drainage area Wang et al. [43], Chougong et al. [5]. This finding suggests that this group is likely to be an anthropogenic factor.

Cluster analysis is a technique for gaining valuable insight into the grouping of data based on similarity. The cluster analysis of the sediments stations by metals and radionuclides showed very similar tendencies in this study, with three separate clusters (C1-C3) (Figure 7b), each consisting of similar studies spread throughout these three stations. The cluster model indicates that the similarity index of cluster sampling sites is as follows: C1 to C3. Class C1 is composed of samples from the three stations, but it is more represented by the samples from Yoyo II and Kribi stations. Class C2 mainly represents samples from Campo and Kribi stations, while class C3 mostly represents the samples from Campo (Figure 7b). Within both class C1, the stations have more than 50% similarity, class C2 has 35% similarity, and class C3 has 15% similarity. These results show that the different metals obtained are probably influenced by anthropogenic factors and natural sources such as the weathering and erosion of nearby rocks.

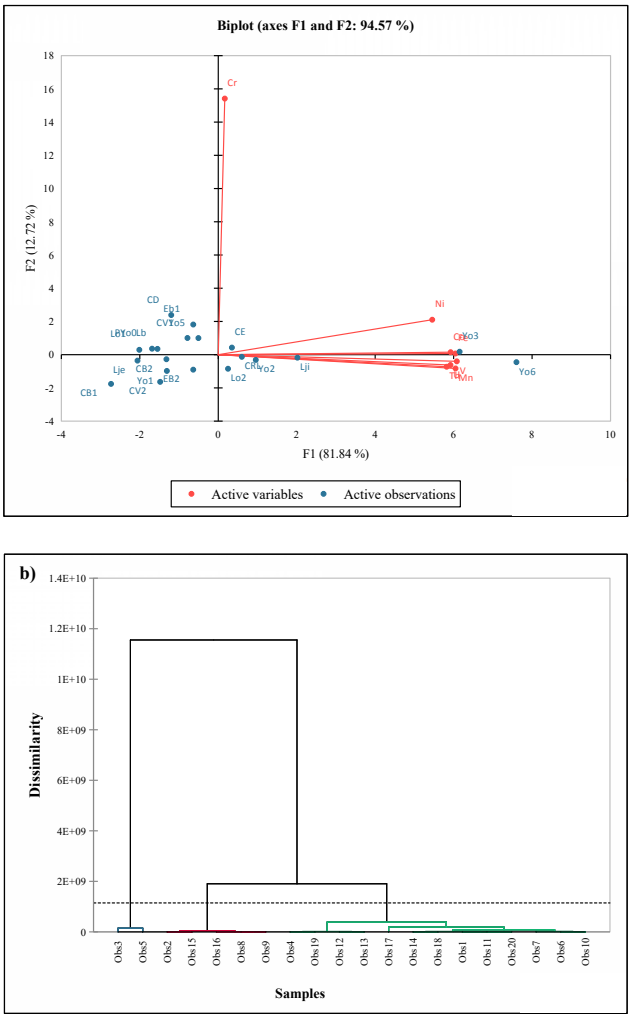

Figure 7. Statistical analysis of sampling stations according to heavy metals and radionuclides of sediment samples along the Cameroonian coast a) Principal component analysis (PCA) b) Similarity dendrogram.

4. Conclusions

Sediment samples along the southern part of the Cameroonian coast have been investigated to infer the distribution, assessment of pollution and ecological risk of heavy metals (Fe, Mn, Cr, V, Ni and Co), and radionuclides (Th and U). The results of this study showed that all metals, including radionuclides are higher than the average shales values, except Ni and Co, which have lower values. Moreover, the spatial distribution of these elements showed that Fe, Mn, Cr and V have very high concentrations compared

to the others.

The Igeo values of all metals and radionuclides of the study area characterize the sediments unpolluted and moderately polluted, except Cr which presents strongly polluted. The occurrence of Cr in this study could be attributed to the anthropogenic source such as combustion of plastic trash, various agricultural wastes, tourism-related sludge dredging. In general, the assessment of pollution (CF, DC and PLI), in the sediments of the southern part of the Cameroonian coast reveals that these sediments are low to high contaminated, according to each station. These results reveal that these sediments are unpolluted.

The evaluation of the potential ecological risk (Er and RI), indicates that this part of the coast of Cameroon is a low risk area. Matrix correlation, principal components and cluster analysis were employed to confirm the similarity between heavy metals and radionuclides, and to assess the influence of anthropogenic activities on sediment quality. Based on these analyses, heavy metals (Fe, Mn, Cr, V, Ni, and Co) have common anthropogenic sources, while radionuclides (Th and U) have a natural source.

This study provides information on environmental pollution in the study area by assessing the contamination of sediments along the southern of the Cameroonian coast which could be useful to the government in limiting the spread of harmful contaminants.

Author Contributions

All the authors quoted in this paper have participated ardently in the writing of this manuscript, by exposing very beneficial arguments in the context of this study and have also worked for the form and the linguistic quality provide in this document. work of the first author and will also be used under abstract form for publication of article, and we consent to its use in this manner. We agree with the statements above and declare that this submission follows the policies of the journal as outlined in the guide.

Data Availability Statement

All data used in this study have been reported in Table 2 and analyzed in the commercial laboratory ALS from Vancouver, Canada. We add that no additional data was carried out for the realization of this work.

Funding

AZEB testifies on behalf of all the authors of this paper that, this research has not received any specific grant from any funding body in the public, commercial or non-profit sectors.

Acknowledgement

The authors are grateful to the Department of Earth Sciences, Faculty of Sciences, University of Dchang.

Conflict of Interest

In the name of all the authors, the corresponding author states that there is no conflict of interest.

References

[1] Akcil, A., Erust, C., Ozdemiroglu, S., et al., 2015. A review of approaches and techniques used in aquatic contaminated sediments: metal removal and stabilization by chemical and biotechnological processes. Journal of Cleaner Produvtion. 86, 24-36.

[2] Ip, C.C., Li, X.D., Zhang, G., et al., 2007. Trace metal distribution in sediments of the Pearl River Estuary and the surrounding coastal area, South China. Environmental Pollution. 147, 311-323.

[3] Huang, F., Xu, Y., Tan, Z., et al., 2018. Assessment of pollution and identification of sources of heavy metals in sediments from west coast of Shenzhen, China. Environmental Sciences and Pollution Research. 25, 3647-3656.

[4] Bramha, S.N., Mohanty, A.K., Satpathy, K.K., et al., 2014. Heavy metal content in the beach sediment with respect to contamination levels and sediment quality guidelines: A study at Kalpakkam coast, southeast coast of India. Environment Earth Sciences. 72, 4463-4472.

[5] Chougong, D.T., Ngueutchoua, G., Dicka, E.H., et al., 2021. Distributions of trace metals and radionuclides contamination in alluvial sediments from the Lobé River in Cameroon. Earth System and Environment. 6(1), 121-139.

[6] Ekoa Bessa, A.Z., Ambassa Bela, V., Ngueutchoua, G., et al., 2022. Characteristics and source identification of environmental trace metals in beach sediments along the Littoral zone of Cameroon. Earth Systems and Environment. 6, 175-187.

[7] Bastami, K.D., Neyestani, M.R., Shemirani, F., et al., 2015. Heavy metal pollution assessment in relation to sediment properties in the coastal sediments of the southern Caspain Sea. Marine Pollution Bulletin. 92, 237-243.

[8] Zhang, H., Walker, T.R., Davis, E., et al., 2019. Spatiotemporal characterization of metals in small craft harbor sediments in Nova Scotia, Canada. Marine Pollution Bulletin. 140, 493-502.

[9] Li, F., Huang, J., Zeng, G., et al., 2013. Spatial risk assessment and sources identification of heavy met-

als in surface sediments from the Dongting Lake, Middle China. Journal of Geochemical Exploration. 132, 75-83.

[10] Hossain, M.B., Shanta, T.B., Ahmed, A.S., et al., 2019. Baseline study of heavy metal contamination in the Sangu River estuary, Chattogram, Bangladesh. Marine Pollution Bulletin. 140, 255-261.

[11] Bartlett, J.H., Castro, A., 2019. Isotopic spectroscopy of uranium atomic beams produced by thermal reduction of uranium compounds. Spectrochimica Acta part B: Atomic Spectroscopy. 155, 61-66.

[12] Mandeng, E.P.B., Bidjeck, L.M.B., Bessa, A.Z.E., et al., 2019. Contamination and risk assessment of heavy metals, and uranium of sediments in two watersheds in Abiete-Toko gold district, Southern Cameroon. Heliyon. 5, 02591.

[13] Baranov, V.I., Morozova, N.G., 1971. The behavior of natural radionuclides in soils. Radioekologiya. 2, 13-41.

[14] Armstrong-Altrin, J.S., 2020. Detrital zircon U-Pb geochronology and geochemistry of the Riachuelos and Palma Sola beach sediments,Veracruz State, Gulf of Mexico: A new insight on palaeoenvironment. Journal of Palaeogeography. 9, 1-27.

[15] Tehna, N., Sababa, E., Ekoa Bessa, A.Z., et al., 2019. Mine waste and heavy metal pollution in Betare-Oya Mining Area (Eastern Cameroon). Environmental and Earth Sciences Research Journal. 6, 167-176.

[16] Noa Tang, D., Ekoa Bessa, A.Z., Brice, T.K., et al., 2021. Heavy metal contamination and ecological risk assessment of overlying water and sediments of Nkozoa Lake (Southern Cameroon). Annual Research and Review Biology. 92-109.
DOI: https://doi.org/10.9734/arrb/2021/v36i430366

[17] Bianchini, A., Cento, F., Guzzini, A., et al., 2019. Sediment management in coastal infrastructures: Techno-economic and environmental impact assessment of alternative technologies to dredging. Journal of Environmental Management. 248, 109332.

[18] El-Amier, Y.A., Bessa, A.Z.E., Elsayed, A., et al., 2021. Assessment of the heavy metals pollution and ecological risk in sediments of Mediterranean Sea Drain Estuaries in Egypt and Phytoremediation potential of two emergent plants. Sustainability. 13, 12244.

[19] Bilong, P., Belinga, S.E., Volkoff, B., 1992. Sequence of evolution of armoured landscapes and ferrallitic soils in tropical forest areas of Central Africa: Place of soils with spotted clay horizons. Comptes Rendus de l'Academie des Sciences. 314, 109-115.

[20] Ngueutchoua, G., Bessa, A.Z., Eyong, J.T., et al., 2019. Geochemistry of cretaceous fine-grained siliciclastic rocks from Upper Mundeck and Logbadjeck Formations, Douala sub-basin, SW Cameroon: Implications for weathering intensity, provenance, paleoclimate, redox condition, and tectonic setting. Journal of African Earth Sciences. 152, 215-236.

[21] Mbesse, C.O., Bessong, M., Ntamak-Nida, M.J., et al., 2020. Palynology and palynofacies analyses in the Douala sub-basin: Implications on palaeoenvironment evolution of the Souellaba Formation/west Cameroon. Journal of African Earth Sciences. 172, 104004.

[22] Nguene, F.R., Tamfu, S., Loule, J.P., et al., 1992. Palaeoenvironments of the Douala and Kribi/Campo subbasins in Cameroon, West Africa. Bulletin des Centres de recherches exploration-production Elf-Aquitaine. Mémoire. (13), 129-139.

[23] Lawrence, R.S., Munday, S., Bray, R., 2002. Regional geology and geophysics of the Eastern Gulf of Guinea (Niger Delta to Rio Muni). Lead Edge. 21, 1112-1117.

[24] Ntamak-Nida, M.J., Bourquin, S., Makong, J.C., et al., 2010. Sedimentology and sequence stratigraphy from outcrops of the Kribi-Campo subbasin: Lower Mundeck Formation (Lower Cretaceous, southern Cameroon). Journal of African Earth Sciences. 58, 1-8.

[25] Ekoa Bessa, A.Z., Ngueutchoua, G., Janpou, A.K., et al., 2021. Heavy metal contamination and its ecological risks in the beach sediments along the Atlantic Ocean (Limbe coastal fringes, Cameroon). Earth System and Environment. 5, 433-444.

[26] Chen, H.Y., Teng, Y.G., Wang, J.S., et al., 2012. A framework for pollution characteristic assessment and source apportionment of heavy metal contaminants in riverbed sediments: A case study. Fresenius Environmental Bulletin. 21, 1112-1119.

[27] Singovszka, E., Balintova, M., 2019. Enrichment factor and geo-accumulation index of trace metals in sediments in the River Hornad, Slovakia. IOP Conference Series: Earth and Environmental Science. 222, 012023.

[28] Tomlinson, D., Wilson, J., Harris, C., et al., 1980. Problems in the assessment of heavy-metal levels in estuaries and the formation of a pollution index. Helgoländer Meeresuntersuchungen. 33, 566-575.

[29] Håkanson, L., 1980. An ecological risk index for aquatic pollution control. A sedimentological approach. Water Research. 14, 975-1001.

[30] Wang, J., Jiang, Y., Sun, J., et al., 2020. Geochemical transfer of cadmium in river sediments near a lead-zinc smelter. Ecotoxicology and Environmental Safety. 196, 110529.

[31] Suresh, G., Ramasamy, V., Meenakshisundaram, V., et al., 2011. Influence of mineralogical and heavy

metal composition on natural radionuclide concentrations in the river sediments. Applied Radiation and Isotopes. 69, 466-1474.

[32] Turekian, K.K., Wedepohl, K.H., 1961. Distribution of the elements in some major units of the earth's crust. Geological Society America Bulletin. 72, 175-192.

[33] Ramos-Vázquez, M.A., Armstrong-Altrin, J.S., 2019. Sediment chemistry and detrital zircon record in the Bosque and Paseo del Mar coastal areas from the southwestern Gulf of Mexico. Marine and Petroleum Geology. 110, 650-675.

[34] Saifullah, S.M., Ismail, S., Khan, S.H., et al., 2004. Land use-iron pollution in mangrove habitat of Karachi, Indus Delta. Earth Interactions. 8, 1-9.

[35] Sankarappan, R., Gopalakrishnan, G., Shanmugam, R., et al., 2021. Diffusion, textural characteristics, and source identification of the heavy metals in the Karankadu mangrove sediments, South India. Arabian Journal of Geosciences. 14, 1.

[36] Long, E.R., Field, L.J., Macdonald, D.D., 1998. Predicting toxicity in marine sediments with numerical sediment quality guidelines. Environmental Toxicology and Chemistry. 17, 714-727.

[37] Kasilingam, K., Gandhi, M.S., Krishnakumar, S., et al., 2016. Trace element concentration in surface sediments of Palk Strait, southeast coast of Tamil Nadu, India. Marine Pollution Bulletin. 111, 500-508.

[38] Li, C., Chengwen, S., Yanyan, Y., et al., 2015. Spatial distribution and risk assessment of heavy metals in sediments of Shuangtaizi estuary, China. Marine Pollution Bulletin. 98, 358-364.

[39] Ekoa Bessa, A.Z., El-Amier, Y.A., Doumo, E.P.E., et al., 2018. Assessment of sediments pollution by trace metals in the Moloundou swamp, southeast Cameroon. Annual Research and Review Biology. 1-13.

[40] Sahoo, S.K., Hosoda, M., Kamagata, S., et al., 2011. Thorium, uranium and rare earth elements concentration in weathered Japanese soil. Samples Progress in Nuclear Science and Technology. 1, 416-419.

[41] Domingo, J.L., 2001. Reproductive and developmental toxicity of natural and depleted uranium: A review. Reproductive Toxicology. 15, 603-609.

[42] Pinto, M.M.S.C., Silva, M.M.V.G., Neiva, A.M.R., 2004. Pollution of water and stream sediments associated with the Vale De Abrutiga Uranium Mine, Central Portugal Mine. Water and the Environment. 23, 66-75.

[43] Wang, X., Chen, F., Hasi, E., et al., 2008. Desertification in China: An assessment. Earth Sciences Reviews. 88, 188-206.

Appendix

Appendix 1. Geoaccumulation indices for heavy metals (Fe, Mn, Cr, V, Ni, Co) and radionuclides (Th, U).

ID	Fe	Mn	Cr	V	Ni	Co	Th	U	Station
Yo1	–1.72	–2.04	2.19	–2.40	–3.50	–2.51	–1.02	–1.93	
Yo2	–0.81	–0.23	2.34	–0.93	–2.87	–2.03	1.52	0.46	
Yo3	0.49	1.21	2.48	0.48	–2.42	–0.93	3.06	1.79	Yoyo II
Yo5	–1.33	–1.23	2.60	–1.88	–3.21	–2.51	0.74	–0.40	
Yo6	0.72	1.42	2.34	0.71	–2.21	–0.66	3.16	1.98	
PYo0	–2.09	–3.04	2.48	–3.08	–3.50	–2.83	–2.63	–2.79	
Lje	–2.54	–3.04	2.34	–3.70	–3.87	–3.25	–2.54	–3.19	
Lji	–0.61	0.21	2.34	–0.32	–2.42	–1.51	1.17	0.36	
Lo2	–0.65	–0.87	2.19	–1.44	–2.87	–1.51	–1.17	–1.61	
Lo1	–2.05	–2.46	2.48	–3.15	–3.87	–3.83	–2.91	–3.16	Kribi
Lb	–1.83	–2.04	2.48	–3.02	–3.50	–2.83	–2.07	–2.62	
EB2	–1.15	–1.23	2.19	–1.70	–3.09	–2.25	–1.38	–1.97	
Eb1	–1.19	–2.46	2.72	–1.72	–2.87	–2.25	–2.03	–2.15	
CD	–1.58	–2.04	2.83	–2.70	–3.21	–2.51	–2.21	–2.67	
CE	–0.76	–0.23	2.48	–1.22	–2.87	–1.83	–0.53	–1.06	
CRL	–0.55	–0.46	2.34	–1.10	–2.58	–1.83	–0.86	–1.14	
CB1	–3.90	–4.04	2.02	–5.29	–4.67	–4.83	–5.29	–4.72	Campo
CB2	–1.55	–2.04	2.34	–2.70	–3.35	–2.51	–3.10	–2.91	
CV1	–1.37	–1.23	2.60	–1.91	–3.35	–2.25	–0.51	–1.42	
CV2	–1.80	–2.04	2.02	–2.80	–3.50	–2.83	–0.82	–2.27	

Appendix 2. Statistical descriptive of contamination factor (CF), degree of contamination (DC) and pollution load index (PLI) in the sediment samples.

ID	CF								DC	PLI	Station
	Fe	Mn	Cr	V	Ni	Co	Th	U			
Yo1	0.45	0.36	6.84	0.28	0.13	0.26	0.74	0.39	9.48	0.49	Yoyo II
Yo2	0.85	1.28	7.60	0.78	0.21	0.37	4.31	2.07	17.47	1.20	
Yo3	2.10	3.46	8.36	2.09	0.28	0.79	12.50	5.19	34.78	2.56	
Yo5	0.60	0.64	9.12	0.41	0.16	0.26	2.50	1.14	14.82	0.80	
Yo6	2.47	4.01	7.60	2.45	0.32	0.95	13.42	5.92	37.13	2.86	
PYo0	0.35	0.18	8.36	0.18	0.13	0.21	0.24	0.22	9.88	0.33	
Lje	0.26	0.18	7.60	0.12	0.10	0.16	0.26	0.16	8.84	0.27	Kribi
Lji	0.98	1.73	7.60	1.20	0.28	0.53	3.38	1.92	17.62	1.40	
Lo2	0.96	0.82	6.84	0.55	0.21	0.53	0.67	0.49	11.06	0.76	
Lo1	0.36	0.27	8.36	0.17	0.10	0.11	0.20	0.17	9.74	0.29	
Lb	0.42	0.36	8.36	0.18	0.13	0.21	0.36	0.24	10.28	0.39	
EB2	0.67	0.64	6.84	0.46	0.18	0.32	0.58	0.38	10.07	0.60	
Eb1	0.66	0.27	9.88	0.45	0.21	0.32	0.37	0.34	12.49	0.53	
CD	0.50	0.36	10.64	0.23	0.16	0.26	0.33	0.24	12.73	0.44	Campo
CE	0.89	1.28	8.36	0.65	0.21	0.42	1.04	0.72	13.56	0.89	
CRL	1.02	1.09	7.60	0.70	0.25	0.42	0.83	0.68	12.59	0.88	
CB1	0.10	0.09	6.08	0.04	0.06	0.05	0.04	0.06	6.52	0.10	
CB2	0.51	0.36	7.60	0.23	0.15	0.26	0.18	0.20	9.50	0.38	
CV1	0.58	0.64	9.12	0.40	0.15	0.32	1.05	0.56	12.82	0.66	
CV2	0.43	0.36	6.08	0.22	0.13	0.21	0.85	0.31	8.60	0.44	

Appendix 3. Pollution indices (Er and RI) in the sediment study.

ID	Mn	Cr	Ni	RI	Station
Yo1	0.36	13.68	0.66	14.71	YOYO II
Yo2	1.28	15.20	1.03	17.51	
Yo3	3.47	16.72	1.40	21.58	
Yo5	0.64	18.25	0.81	19.69	
Yo6	4.01	15.20	1.61	20.83	
PYo0	0.18	16.72	0.66	17.57	
Lje	0.18	15.20	0.51	15.90	Kribi
Lji	1.73	15.20	1.40	18.33	
Lo2	0.82	13.68	1.03	15.53	
Lo1	0.27	16.72	0.51	17.51	
Lb	0.36	16.72	0.66	17.75	
EB2	0.64	13.68	0.88	15.20	
Eb1	0.27	19.77	1.03	21.07	
CD	0.36	21.29	0.81	22.46	Campo
CE	1.28	16.72	1.03	19.03	
CRL	1.09	15.20	1.25	17.55	
CB1	0.09	12.16	0.29	12.55	
CB2	0.36	15.20	0.74	16.30	
CV1	0.64	18.25	0.73	19.62	
CV2	0.36	12.16	0.66	13.19	

Appendix 4. Rotated component matrix of heavy metals and radionuclides.

Factor loading	F1	F2	F3	F4	F5
Fe	0.387	0.005	0.069	0.458	0.098
Mn	0.387	–0.053	–0.110	–0.010	0.750
Cr	0.011	0.987	–0.143	0.046	0.041
V	0.389	–0.026	–0.035	–0.184	0.255
Ni	0.349	0.135	0.689	–0.553	–0.158
Co	0.379	0.010	0.315	0.610	–0.320
Th	0.373	–0.046	–0.488	–0.124	–0.404
U	0.379	–0.040	–0.388	–0.247	–0.266
Eigenvalue	6.548	1.018	0.353	0.048	0.016
Variability (%)	81.844	12.723	4.413	0.601	0.206
Cumulative (%)	81.844	94.568	98.981	99.582	99.788

NASS
NAN YANG ACADEMY OF SCIENCES

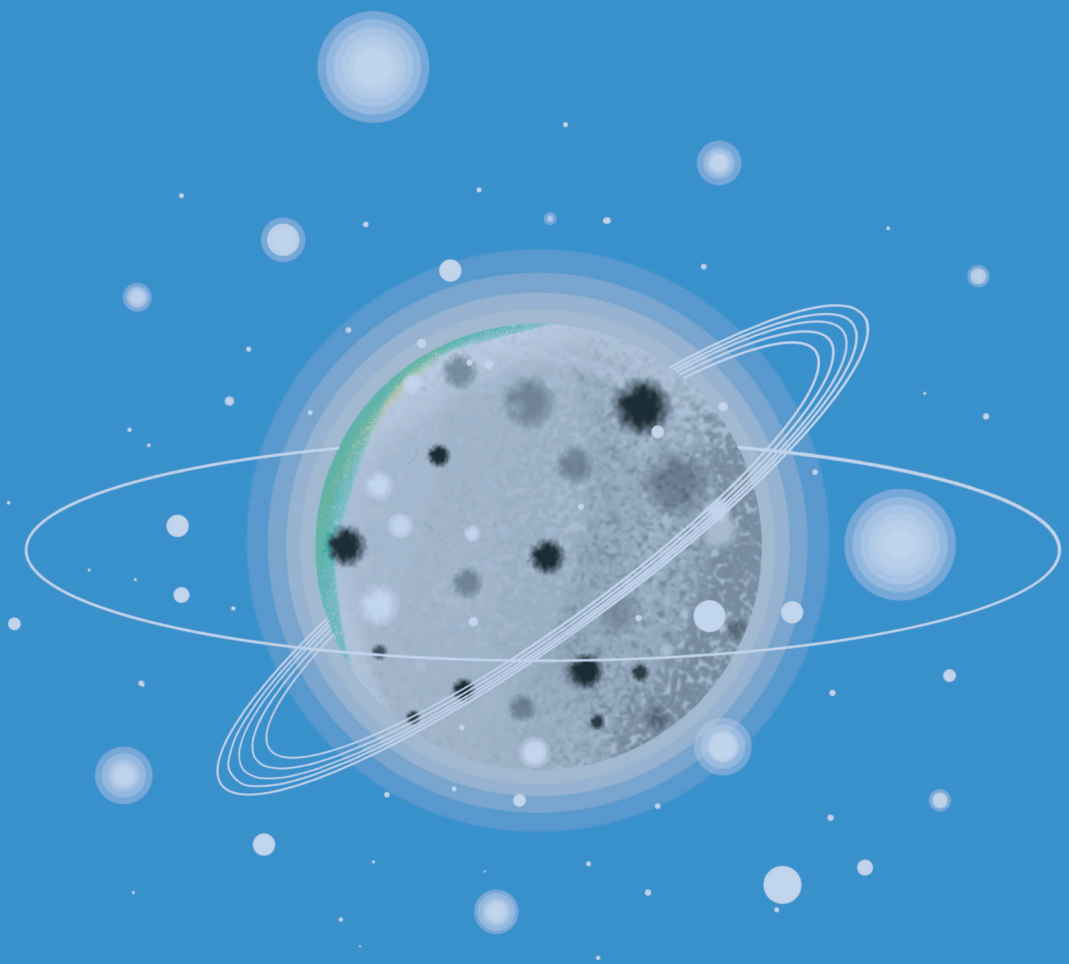

2810-9732
01
9 772810 973225

Tel.: +65 65881289
E-mail: eps@nassg.org
Website: ojs.nassg.org
Add.: 12 Eu Tong Sen Street #07-169 Singapore 059819